MULTIMODALITY IMAGING OF TUMOR VASCULATURE AND METABOLISM

APPROVED BY SUPERVISORY COMMITTEE

Dawen Zhao, M.D., Ph.D. (Mentor)

Ralph P. Mason, Ph.D. (Committee Chair)

Hanzhang Lu, Ph.D.

Jinming Gao, Ph.D.

Debabrata Saha, Ph.D.

DEDICATION

I would like to thank my supervisor, Dr. Dawen Zhao, for giving me the opportunity to work in his lab and for his support and guidance through my PhD journey. I am also grateful to my committee members, Dr. Ralph P. Mason, Dr. Debabrata Saha, Dr. Hanzhang Lu, and Dr. Jinming Gao for their invaluable help and advice.

Also, thanks to all the members of the Laboratory of Prognostic Radiology (LPR) group for supporting me with resources and technical help, especially Dr. Li Liu for her help in cell culture techniques and Dr. Rami R. Hallac for helping me with my experiments and data analysis.

Lastly but most importantly, I would like to avail myself to this opportunity to thank my parents, Li Zhou and Shengyun Wu, grandmother, Yanrong Han, cousin Zhenghao Zhou and my best friend Acong Xu. Thank you for being patient and encouraging when I needed it the most, and most notably, being there to help guide my way.

MULTIMODALITY IMAGING OF TUMOR VASCULATURE AND METABOLISM

by

HELING ZHOU

DISSERTATION

Presented to the Faculty of the Graduate School of Biomedical Sciences

The University of Texas Southwestern Medical Center at Dallas

In Partial Fulfillment of the Requirements

For the Degree of

DOCTOR OF PHILOSOPHY

The University of Texas Southwestern Medical Center at Dallas

Dallas, Texas

May, 2013

MULTIMODALITY IMAGING OF TUMOR VASCULATURE AND METABOLISM

HELING ZHOU, Ph.D.

The University of Texas Southwestern Medical Center at Dallas, 2013

Mentor: DAWEN ZHAO, M.D., Ph.D.

Cancer is the second leading cause of death in America. A number of abnormal features in tumor vasculature and metabolism have been identified as imaging biomarkers to detect tumor boundary, provide physiological information, predict treatment response and guide surgeries.

In chapter 2, longitudinal MRI was applied to monitor the initiation and development of intracranial tumors and assess the changes in tumor vascular volume and permeability in a mouse model of breast cancer brain metastases. Using a 9.4T system, high resolution anatomic MRI and dynamic susceptibility

contrast (DSC) perfusion MRI were acquired at different time points after an intracardiac injection of brain-tropic breast cancer MDA-MB231-BR-EGFP (231-BR) cells.

DSC MRI revealed that relative cerebral blood volume (rCBV) of metastatic tumors was significantly lower than that of contralateral normal brain. Intriguingly, longitudinal measurements showed that rCBV of individual metastases at early stage was similar to, but became significantly lower than that of their healthy counterparts with tumor growth. The rCBV data were in agreement with histological analysis of microvascular density (MVD).

In chapter 3, 20 nm super-paramagnetic iron oxide (SPIO) particles were conjugated with a novel monoclonal antibody PGN635 to image the exposed phosphatidylserine (PS) on the tumor vascular endothelial cells and evaluate the enhanced exposure of PS as a result of radiation therapy in mice subcutaneous tumors. Both *in vitro* and *in vivo* studies verified the binding of SPIO-PGN635 and showed elevated PS exposure upon irradiation. In the subcutaneous tumor models, the distribution of the contrast appeared to be inhomogeneous across the tumors. Sparse signal loss was observed on the T_2 weighted images after the administration of SPIO-PGN635. The signal loss fraction indicated significantly more increase in the irradiated tumor compared to the non-irradiated side. Prussian blue staining confirmed the accumulation of SPIO-PGN635 in the

tumors along the blood vessels. Control and blocking studies were conducted to validate antigen specificity.

It is recognized that cancer cells exhibit highly elevated glucose metabolism compared to non-tumor cells. In chapter 4, I have applied *in vivo* optical imaging to study dynamic uptake of a near-infrared dye-labeled glucose analogue, 2-deoxyglucose (2-DG) by orthotopic glioma in a mouse model. Dynamic fluorescent imaging revealed significantly higher signal intensity in the tumor side of the brain than the contralateral normal brain 24 h after injection. Even stronger contrast was achieved by removing the scalp and skull of the mice. In contrast, a control dye, IRDye800CW carboxylate, showed little difference. Ex vivo fluorescence imaging performed on ultrathin cryosections of tumor bearing whole brain revealed distinct tumor margins. Microscopic imaging identified cytoplasmic locations of the 2-DG dye in tumor cells.

TABLE OF CONTENTS

PRIOR PUBLICATIONS

Papers

Heling Zhou, Min Chen, Dawen Zhao. Longitudinal MRI evaluation of intracranial development and vascular characteristics of breast cancer brain metastases in a mouse model. PLoS ONE, 2013 (in press)

Heling Zhou, Kate Luby-Phelps, Bruce E. Mickey, Amyn A. Habib, Ralph P. Mason and Dawen Zhao. Dynamic Near-Infrared Optical Imaging of 2-Deoxyglucose Uptake by Intracranial Glioma of Athymic Mice. PLoS ONE, 2009. 4(11): e8051

Dawen Zhao, Jason H. Stafford, **Heling Zhou**, Philip E. Thorpe. Near-infrared Optical Imaging of Exposed Phosphatidylserine in a Mouse Glioma Model. Translational Oncology, 2011. **4**(6): p. 355-364.

Debabrata Saha, Henry Dunn, **Heling Zhou**, Hiroshi Harada, Masahiro Hiraoka, Ralph P. Mason, Dawen Zhao. *In vivo* Bioluminescence Imaging of Tumor Hypoxia Dynamics of Breast Cancer Brain Metastasis in a Mouse Model. J Vis Exp, 2011. (doi:10.3791/3175):e3175.

Abstracts and conferences

Heling Zhou, Dawen Zhao. Longitudinal MRI studies of changes in tumor vascular perfusion and permeability of breast cancer brain metastasis in a mouse model. Gordon Research Conference, *in vivo* MR. July 2012.

Heling Zhou, Amyn Habib, Ralph P. Mason, Dawen Zhao. Assessing vascular perfusion of primary and metastatic brain tumors using MRI. UT Metroplex Day. February 2012.

Heling Zhou, Jason Reneau, Ralph P. Mason, Dawen Zhao. *In vivo* imaging of tumor hypoxia and vasculature of gliomas and breast cancer brain metastasis using mouse models. Southern Biomedical Engineering Conference. May 2011.

Heling Zhou, Amyn Habib, Ralph P. Mason, Dawen Zhao. Integrated MRI Approaches to Interrogate Tumor Oxygenation and Vascular Perfusion of Orthotopic Brain Tumors in a Mouse Model. ISMRM. May 2010.

Heling Zhou, Amyn Habib, Peter Antich, Ralph P. Mason, Dawen Zhao. *In vivo* Imaging of Tumor Hypoxia and Vasculature of Orthotopic Mouse Brain

Tumor Models. Journal of Nuclear Medicine, Molecular Neuroimaging Symposium, May 2010.

Heling Zhou, Ana Gondim, Debabrata Saha, Vikram Kodibagkar, Ralph Mason, Dawen Zhao. *In vivo* Multimodal Imaging of Orthotopic Gliobastoma xenografts in Nude Mice. Frontiers of Biomedical Imaging Science. June 2009

LIST OF FIGURES

LIST OF DEFINITIONS

2-DG	2-Deoxyglucose
231-BR	MDA-MB231-BR-EGFP
A5	Annexin V
ABAE	Adult Bovine Aortic Endothelial
ADC	Apparent Diffusion Coefficient
ASL	Arterial Spin Labeling
ATP	Adenosine Triphosphate
BBB	Brain Blood Barrier
BF	Blood Flow
BLI	Bioluminescent Imaging
BOLD	Blood Oxygen Level Dependent
BTB	Blood Tumor Barrier
BV	Blood Volume
CB	Carbogen
CBF	Cerebral Blood Flow
ClfA	Clumping Factor A
CNS	Central Nervous System
CSF	Cerebral Spinal Fluid
CT	Computed Tomography
DCE	Dynamic Contrast Enhanced
$dHbO_2$	Deoxyhemoglobin
DMEM	Dulbecco's Modified Eagle's Medium
DSC	Dynamic Susceptibility Contrast

EPR	Enhanced Permeability and Retention
FLI	Fluorescent Imaging
FOV	Field of View
FPPM	First-Pass Pharmacokinetic Modeling
FSEMS	Fast Spin Echo Multi Slice
GBM	Glioblastoma Multiforme
GEMS	Gradient Echo Multi Slice
GLUT	Glucose Transporter
HbO_2	Oxyhemoglobin
ktrans	Blood Perfusion-Vessel Permeability
MRI	Magnetic Resonance Imaging
MVD	Micro-Vessel Density
NIR	Near Infrared
PEG	Polyethylene Glycol
PET	Positron Emission Tomography
PS	Phosphatidylserine
rCBV	relative Cerebral Blood Volume
ROI	Regions of Interest
s.c.	Subcutaneous
SEMS	Spin Echo Multi Slice
SI	Signal Intensity
SNR	Signal to Noise Ratio
SPECT	Single Photon Emission Computed tomography
SPIO	Superparamagnetic Iron Oxide
T/M	Tumor/Muscle Ratio

T_1	Spin-Lattice Relaxation
T_2	Spin-Spin Relaxation
T_2*	Apparent Spin-Spin Relaxation
TCA	Tricarboxylic Acid
TE	Echo Time
TME	Tumor Microenvironment
TNR	Tumor/Normal ratio
TR	Repetition Time
US	Ultrasonography
ve	Extravascular-Extracellular Volume Fraction
VEGF	Vascular Endothelial Growth Factor

CHAPTER ONE
Introduction

1.1 TUMOR BIOLOGY

1.1.1 Brain tumors

Cancer is one of the leading causes of death in America [1]. It is characterized by uncontrolled growth of anaplastic cells that can invade into surrounding normal tissue and metastasize to distant organs. Cancer is indeed a group of more than 200 different diseases. Brain cancer is among the most aggressive and deadly ones.

Malignant brain tumors can originate from brain itself or metastasize from other organs. According to the 2010 Central Brain Tumor Registry of the United States (CBTRUS) Statistical Report, glioma and meningioma (mainly benign) are the most common types of primary brain tumor, which constitute of about 34% and 35%, respectively [2]. Gliomas can originate from astrocytes, ependymomal cells or oligodendrocytes. Stage IV astrocytoma (glioma that originates from astrocytes) is referred to as glioblastoma multiforme (GBM), which is the most common and most malignant type of glioma [3]. It consists of about half of all gliomas, with a one-year survival of 33.7% and five-year survival of only 4.5% [2]. GBM is characterized by high infiltration and vascularization. The tumor

cells intruding into normal brain make it difficult to identify the tumor boundary, and the incomplete surgery resection leads to recurrence. In addition, GBM is heterogeneous and consists of different subclones and phenotypes, and thus the responses to treatments are variant, which makes it difficult to treat [4].

GBM is the most common primary brain malignancy [3], but brain tumors metastasized from other primary sites have a ten-fold higher incidence [5-8]. Lung, breast and skin (melanoma) are the most common origins of brain metastases [9]. About half of lung cancer patients [10], 30% of stage IV breast cancer patients [11, 12], and two to three quarters for melanoma patients [13] develop brain metastases in the course of disease. Nevertheless, all kinds of brain tumors are associated with high morbidity and mortality. The median survival is less than one year even with the most aggressive treatments [5, 10-14].

Treating brain tumor is challenging. The poor prognosis partially results from impermeability of effective anti-cancer therapeutics through brain blood barrier (BBB) to reach parenchymal tumor cells [15]. Capillaries in body and brain have distinct structures. Endothelial cells (ECs) form capillaries in brain with tight junctions, which are absent in the capillaries found in most parts of the body. In addition, the brain capillaries are surrounded by large numbers of pericytes and astrocytes. All three of them form the BBB, which is less permeable compared to the other capillaries in the body and allows high selectivity of

particles passage in and out of the brain [16-18]. At early stage of both primary and metastatic tumor development, the BBB remains intact. As tumor progresses the BBB gradually becomes permeable. However, it has been reported that the permeability of BBB may be heterogeneously distributed across the tumor and even the most disrupted BBB still remains as an obstacle that limits the drug delivery significantly[19]. As a result, most chemotherapeutic agents that are successful against visceral malignancy fail in treating brain tumors. Several strategies have been developed to circumvent BBB: 1) temporary destruction of BBB by high osmolar drug, 2) enhancing drug permeability through BBB, 3) utilizing catheters, polymers or microchips to deliver drug directly to tumor and 4) delivering drug directly to central nervous system (CNS) [18]. Despite all the effort, the improvement in prognosis is still under satisfactory.

BBB not only hinders the chemotherapeutic drugs from reaching the tumor cells, but also makes it difficult for imaging, given that most imaging agents, especially novel molecular targeting agents, have limited penetration to the tumor parenchyma. However, since the tumor blood network is accessible to the systemic vasculature, imaging tumor vasculature does not require penetration of BBB. Various information can be generated from vascular imaging: from functional to molecular level.

1.1.2 Tumor metabolism and its impact on microenvironment

Glucose is the main source of energy in most organisms. Glucose molecules cannot freely diffuse in the cells but rather they are recognized and transported through the plasma membrane by wide varieties of glucose transporters (GLUTs). The glucose molecule is first phosphorylated in the cell, so that it cannot be transported out of the cells. This reaction also helps to keep low glucose concentration in the cell. Through the process called glycolysis, one glucose molecule is converted into two pyruvate molecules with a net production of two adenosine triphosphates (ATP). In normal cells when oxygen is present, the pyruvate molecules are transported into mitochondria and further broken down into carbon dioxide and water through tricarboxylic acid (TCA) cycle yielding more ATPs. This process of energy production is called aerobic oxidative phosphorylation. Only when the cells are hypoxic or under pathological conditions, pyruvate is converted to lactate and transported out of the cells without more energy yields. Apparently, it is a much less efficient metabolism pathway to breakdown glucose compared to aerobic oxidative phosphorylation. Warburg observed that the tumor cells convert glucose to lactate even when sufficient oxygen is present. As a matter of fact, glycolysis provides more than half of the total energy produced in tumor cells compared to around 10% in

normal cells in aerobic environment [20]. This phenomenon is referred to as aerobic glycolysis or ‘Warburg effect’.

As a result of such inefficient metabolism shift, tumor cells need to consume more glucose to produce enough ATPs for survival and proliferation. Fludeoxyglucose (^{18}F-FDG), a Positron Emission Tomography (PET) imaging agent, uses the Warburg effect to locate primary and metastatic tumors. In fact, it is one of the most used techniques in clinic to diagnose various cancer types.

Another important consequence of the Warburg effect is the over production of lactate, which causes acidic tumor microenvironment. The low pH induces stress to tumor cells as well as stromal cells and vascular ECs within or surrounding the tumor [21].

1.1.3 Tumor vasculature

With high demands for metabolism, tumors need to recruit and incorporate blood vessels in order to sustain oxygen and nutrition supply. In fact, tumor cannot grow beyond 1mm in diameter without its own blood supply, and thus angiogenesis is necessary for further growth [22].

Angiogenesis is the process to form new blood vasculature from existing ones. Under normal conditions, the endothelial cells are mostly quiescent and

angiogenesis is only active transiently for ovarian cycle and wound healing, and the process is tightly controlled by both angiogenesis inducers and inhibitors [23, 24]. For primary solid tumors, angiogenesis is the predominant method to form new blood vessels. In fact, the 'angiogenesis switch' is always on in tumors, along with overabundant growth factors and absence of inhibitors, causing the tumor vessels to sprout constantly (Figure 1-1 A-C).

As a result, the tumor vasculature is characterized by chaos and inefficiency. A number of abnormal features of tumor vessels have been recognized and studied, such as the heterogeneous microvascular distribution, increased vessel diameter, presence of sinusoids, dead ends, arterio-venous shunts, incomplete basal lining and absence of pericytes and smooth muscle [25]. In turn, these structural abnormalities cause further functional deficiencies, including decreased perfusion pressure, increased vascular resistance, and increased permeability. In addition to the morphology and functional changes, some abnormalities have been observed at the cellular and molecular level, i.e., the overexpression of vascular endothelial growth factor (VEGF) and integrin $\alpha_v\beta_3$ [26, 27]. Those biomarkers are elevated during angiogenesis to facilitate the proliferation and survival of ECs.

However, some tumors do not depend on angiogenesis to survive. When the tumor cells are proximate to existing blood vessels, there is no immediate need for

angiogenesis. Instead, the tumor cells grow along the blood vessels in order to obtain oxygen and nutrition supplies (Figure 1-1 E and F). This phenomenon occurs mostly in organs with rich blood vascular network, such as brain, lung and liver, and has been reported in both primary and metastatic tumors [28-34]. The co-opted vessels are usually relatively 'normal' in the beginning of the process. In the case of brain, the BBB is often intact.

Angiogenesis and co-option can co-exist in one single tumor. As the angiogenesis-dependent tumor expands, some tumor cells reach an existing blood network in normal tissue and co-opt with those vessels to survive (Figure 1-1 D). This has been observed in the infiltrative GBM [35-37]. The vessels co-opted by tumor often become dilated and gradually malfunction (Figure 1-1 G) [14], which in turn affects the efficacy of oxygen and nutrition delivery, and further triggers the angiogenesis process (Figure 1-1 H).

Other types of biomarkers are elevated by tumor microenvironment and are not limited to angiogenesis-dependent tumors. As discussed earlier, the tumor microenvironment is hypoxic and acidic, lacks nutrition and is concentrated with metabolism waste (such as ROS). Those stressful conditions have been shown to induce genetic and epigenetic alterations [38]. Examples of such markers include Delta 4, a signaling molecule that is upregulated by hypoxia [39], and phosphatidylserine (PS), a type of phospholipid in inner leaflet of plasma

membrane, become exposed due to the stress signals. The characteristics and diagnostic value of PS is discussed in more details below.

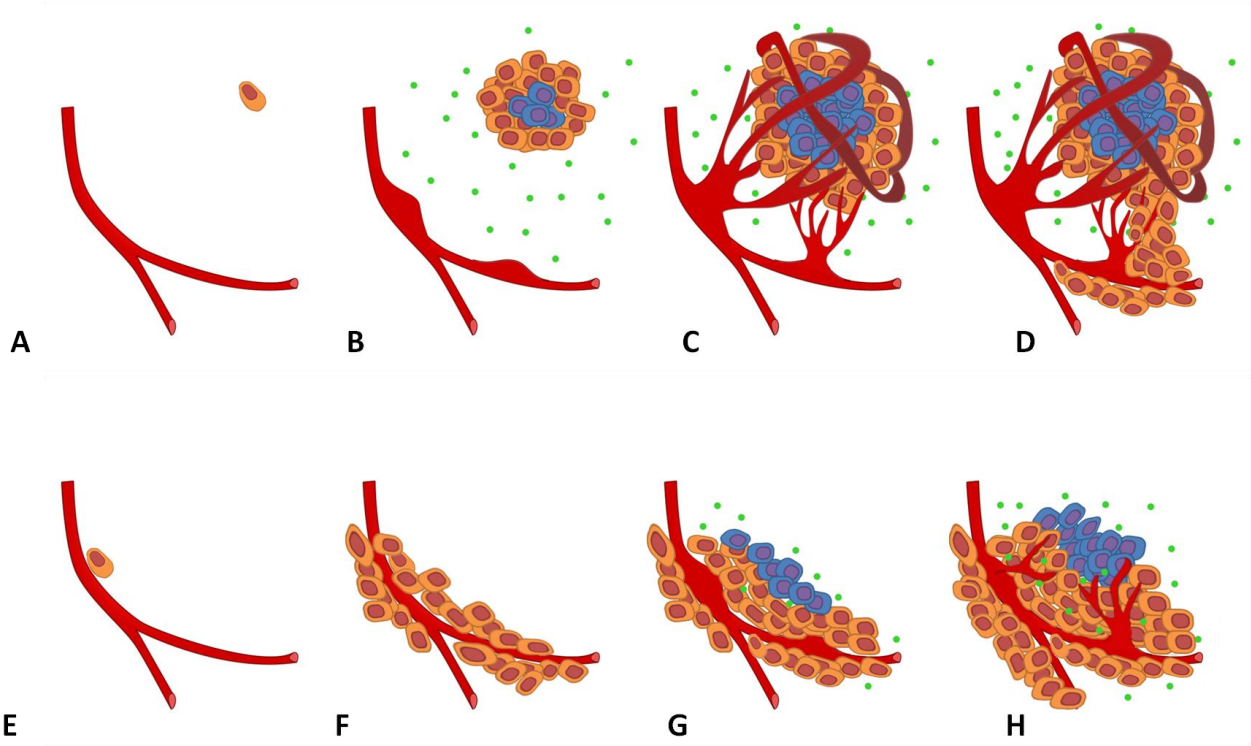

Figure 1-1 Illustrations of the angiogenesis and vascular co-option processes.
Tumor cells (orange) require adequate blood supply to sustain oxygen and nutrition. Once tumor cells become hypoxic (blue), angiogenesis inducers (green dots) are secreted to recruit new vasculature through the angiogenesis process (A-C). Tumor cells can also grow along the existing blood vessels in a process called vascular co-option (E-G). In some cases, both processes coexist to sustain blood supply to tumor cells (D and H).

1.1.4 Phosphatidylserine (PS)

Phospholipid is the main component of cell membranes. It consists of a hydrophilic head and a hydrophobic tail. When the hydrophobic tails align against one another, and the hydrophilic heads expose to water, a lipid bilayer is formed. Many of those lipid bilayers are naturally asymmetric. PS, the most abundant anionic phospholipid of the cell membrane, is a well-known example of such asymmetry. Under normal conditions, PS is restrained to the inner surface of the cell membranes (Figure 1-2 A) [40, 41]. Its exposure is accompanied by apoptosis so that macrophages can recognize the dying cells and remove them from the system [42, 43]. Other than apoptosis, several factors such as cell injury [44] and malignant transformation [45] also cause the exposure of the PS on the cell surface.

Recent studies have shown that PS becomes exposed on the outer surface of viable (non-apoptotic) endothelial cells in tumor vasculature, rendering it a potential biomarker for tumor imaging (Figure 1-2 B) [43, 46, 47]. PS exhibits a number of attractive features. Firstly, PS appears to be a universal marker for various solid tumors. Although the level of exposure varies from type to type, PS-positive tumor vascular endothelial cells have been seen for all the tumors examined to date in animal models, including human breast cancer [46],

Hodgkin's tumor, non-small cell lung carcinoma, colorectal carcinoma [43, 46, 47], mouse lung carcinoma, colon carcinoma [47], prostate carcinoma, breast carcinoma and melanoma [48], and rat glioma [49]. Although the exact mechanism is not fully understood, previous studies have shown that hypoxia, acidity, inflammatory cytokines and the elevated ROS level can cause PS exposure on ECs [43, 50, 51]. Secondly, PS is also highly specific since it is absent on normal ECs including those in the lung, kidney, ovary, liver and brain. In addition, abundance of PS on cell membrane ensures good sensitivity. Lastly, besides spontaneous exposure of PS on tumor vascular endothelial cells, the elevated level of exposure can be induced by cancer treatments including chemotherapy, radiation therapy and hormone deprivation therapy (Figure 1-2 C) [49, 52]. This feature makes PS an attractive biomarker to evaluate treatment efficacy.

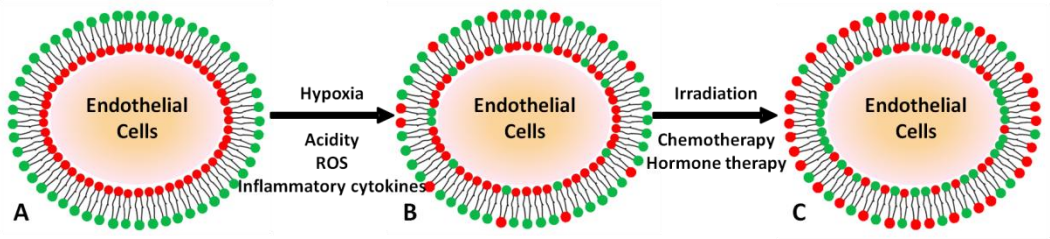

Figure 1-2 Diagram demonstrating the PS distribution (red) on the EC membrane and the factors inducing its exposure.

Annexin V (A5) is a probe used to detect apoptotic cells. It binds to a number of anionic phospholipids including PS. Dr. Philip Thorpe's group developed a series of monoclonal antibodies that target PS with higher specificity and affinity than Annexin V. These antibodies recognize PS complexed with the PS-binding protein, β2-glycoprotien 1 (β2GP1) [43]. In collaboration with Dr. Thorpe's group, we conjugated PGN635, a novel fully human monoclonal antibody, with near infrared dye, IRDye800CW to assess tumor vasculature using near infrared fluorescent imaging (FLI) [53]. In this study, we visualized the specific binding of 800CW-PGN635 to PS in subcutaneous (s.c.) human GBM tumor models (Figure 1-3) and demonstrated the enhanced tumor contrast as a result of irradiation in both s.c. (Figure 1-4) and orthotropic brain tumor models (Figure 1-5) [53].

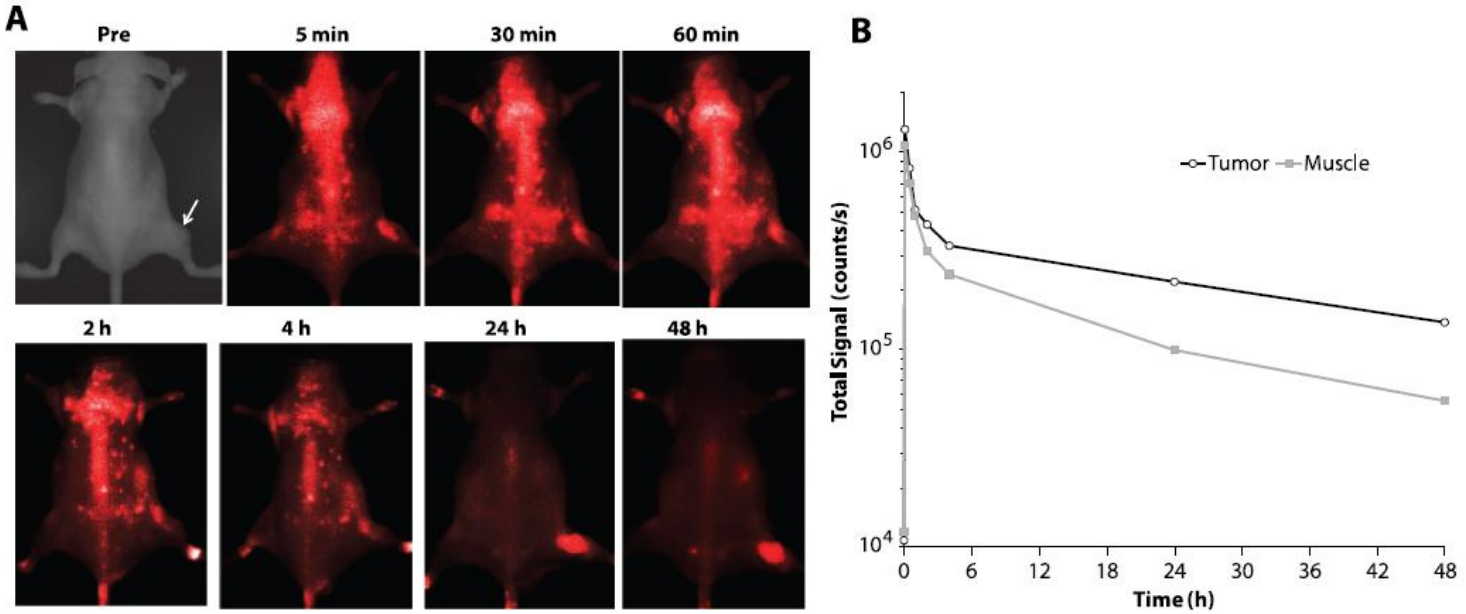

Figure 1-3 *In vivo* NIR imaging of baseline level of PS in a subcutaneous glioma.
(A) A mouse bearing a representative subcutaneous U87 glioma on the right thigh (arrow) was injected i.v. with 800CW-PGN635, and optical imaging was performed at various time points thereafter. During the first 4 hours, the light signal accumulated in the tumor area. However, by 24 hours, the light signal remained only in the tumor and persisted there for at least 48 hours after injection. (B) Mean light intensity curves for the tumor (open circles) and the contralateral muscle (solid squares) revealed that 800CW-PGN635 rapidly gave signals in both the tumor and the normal muscle but that the tumor signal was sustained while the muscle signal had washed out by 24 hours. The tumor-muscle ratios were 2.2 at 24 hours and 2.4 at 48 hours [53].

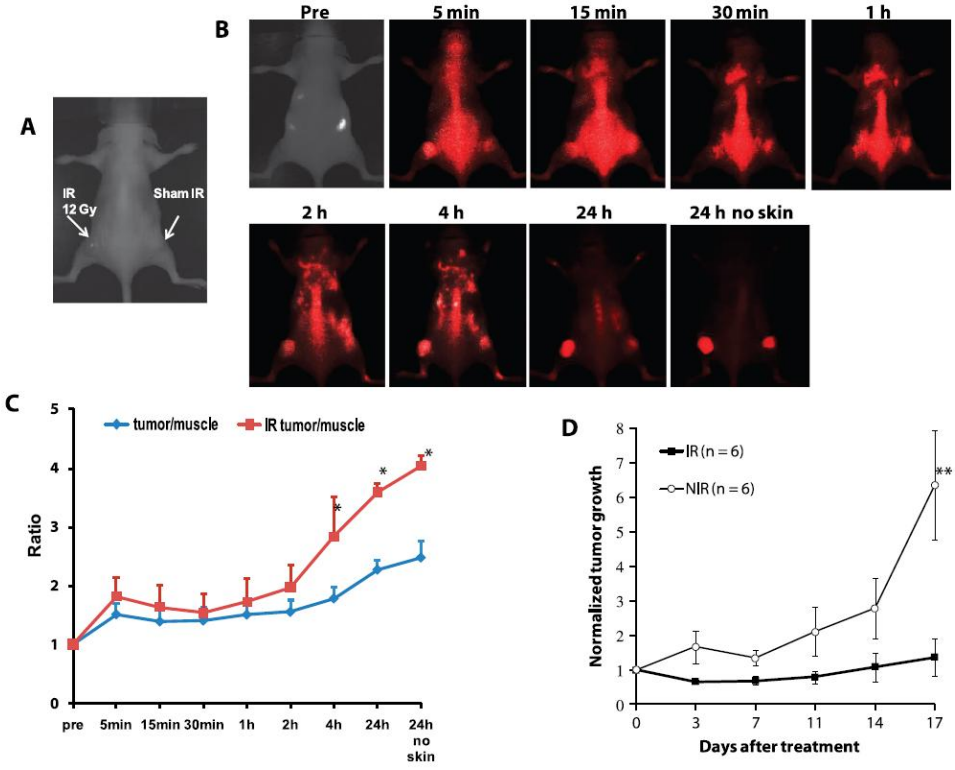

Figure 1-4 *In vivo* NIR imaging of exposed PS in gliomas before and after irradiation.

(A) A mouse bearing representative size-matched subcutaneous U87 tumors on each thigh received 12 Gy of irradiation to the left side tumor. (B) At 24 hours after radiation, 800CWPGN635 was injected through a tail vein, and a series of *in vivo* fluorescence images was acquired at different time points. The contrast between the nonirradiated tumor on the right side and normal muscle increased during the 24-hour period after injection to a tumor/normal ratio (TNR) of 2.6. Irradiation of the tumor on the left side increased levels of exposed PS to a TNR of 4.2. *P < .05 from non-IR. (C) A time course study revealed that the maximal TNR of 2.5 was achieved at 24 hours for nonirradiated tumors (n = 4; blue line). Irradiation increased the TNR of the irradiated tumor to 4.0 at 24 hours (n = 4; red line; P < .05). (D) Tumor growth curves showed that a single dose of 12 Gy of radiation significantly inhibited tumor growth (n = 6), compared with the non-irradiated control tumors (n = 6; **P < 0.01) [53].

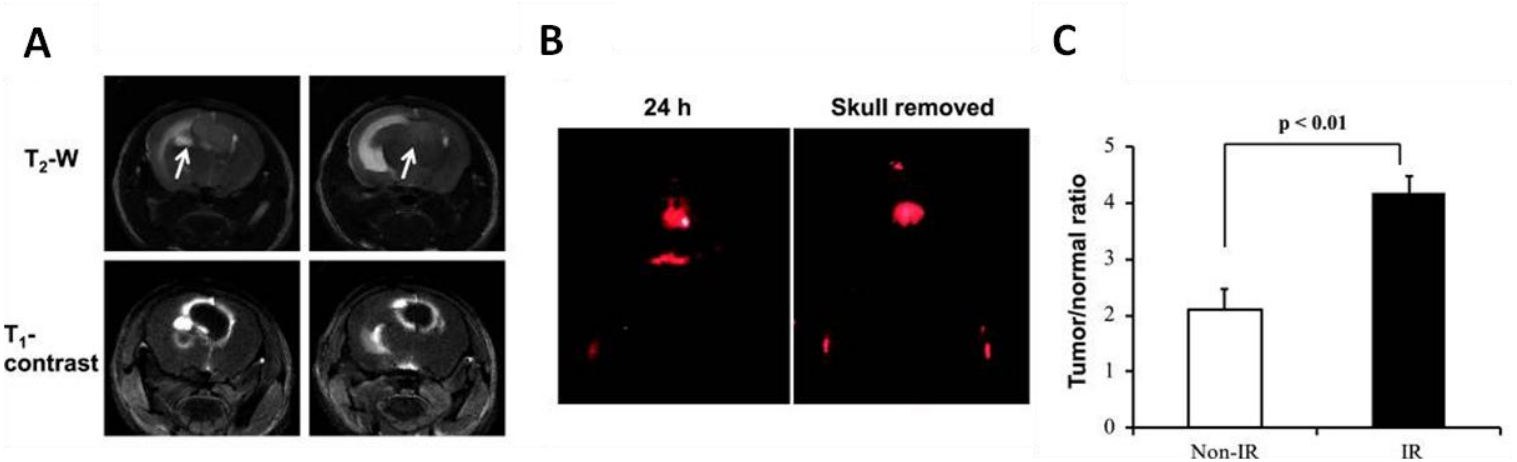

Figure 1-5 *In vivo* optical imaging of exposed PS in orthotopic gliomas.
A mouse bearing a representative orthotopic U87 glioma was irradiated with a single dose of 12 Gy to the whole brain using a D-shaped collimator. (A) Anatomic MRI revealed a 5-mm-diameter intracranial lesion crossing the midline to invade the left side brain on the consecutive T_2-weighted slices. T_1-weighted contrast-enhanced MRI showed the typical ring-shaped enhancement in the tumor periphery. (B) 800CW-PGN635 was injected into the mouse 24 hours after radiation, and dynamic NIR optical imaging was performed. As with the subcutaneous tumors, maximal tumor contrast was achieved 24 hours after injection. Removal of the skull increased the signal, and subsequent dissection confirmed that the signal was from the tumor. (C) The tumor-*versus*-contralateral normal brain ratio TNR was 4.2 ± 0.4 for irradiated tumors (n = 3), which was significantly higher than the TNR of 2.1 ± 0.4 for nonirradiated tumors (n = 3; P < .01) [53].

1.2 TUMOR IMAGING

Imaging approaches can be divided into three types based on the information it can provide: anatomical (morphological), physiological and cellular/molecular imaging. Macroscopic anatomical and physiological imaging techniques include X-ray radiography, computed tomography (CT), ultrasonography (US) and magnetic resonance imaging (MRI). Cellular/Molecular imaging includes positron emission tomography (PET) and single photon emission computed tomography (SPECT), which are the most widely used molecular imaging techniques in both clinical and preclinical studies. In preclinical research, fluorescent imaging (FLI), bioluminescent imaging (BLI) and molecular MRI with the use of targeted contrast agents have also been applied.

Advances in cellular and molecular imaging made it possible to visualize the metabolic activities and cellular and molecular events of cells longitudinally within the living subject. The imaging probes usually consist of at least two parts: a target-specific component and the imaging contrast agent (signaling component). The signaling components are different for each imaging modality: radiotracers are used for PET and SPECT imaging, fluorophores for FLI, microbubbles for US and gadolinium or iron oxide particles for MRI.

In this section, I will briefly discuss the fundamental principle of each imaging modality and summarize the available techniques for vascular imaging.

1.2.1 Basic principles of tumor imaging modalities

1.2.1.1 X-ray radiography and CT

When X-ray passes through a subject, a portion of the photon beam is absorbed by the tissue through photon-electron interaction, and the level of attenuation reflects the tissue density. This is the principle of both X-ray radiography and CT, with the former providing 2D projection images of the subject and the latter 3D reconstructed images. These two imaging approaches are relatively inexpensive, time-efficient, easy to use and provide high spatial resolution images (in the magnitude of 10 to 100um). However, X-ray and CT are most successful in skeleton, lung and breast imaging, since the soft tissue contrast is generally poor. The most common contrast agents used are Iodine-based, which increase absorption where the contrast agents are concentrated, given the high attenuation factor of Iodine. Even with contrast agents, X-ray and CT imaging of brain tumor only provides information about BBB and does not help in defining the tumor boundary. Radiation exposure also limits the number of studies applicable [54].

1.2.1.2 Ultrasonography (US)

US is a safe, easy-to-use, cost-efficient, real-time imaging technology routinely used in clinic. The high frequency sound waves are produced in a transducer and coupled to the subject. The receiver collects the reflection of the sound wave from different structures in the subject wherever there is a density change. The signal is then processed and transformed into images. US can provide good spatial resolution, however the soft tissue contrast is unsatisfactory. Imaging deep structures is usually difficult because of the limited accessibility. In particular, brain imaging is challenging because of the skull, whereas air soft tissue interface interfere with lung and intestine imaging.

Doppler US can be used to measure the speed and direction of BF through the Doppler Effect.

Microbubbles are used as contrast agents for US. Strong reflection can be generated on the interface of air bubbles and soft tissue and thus enhance the image of vasculature. Microbubbles have been studied in targeted imaging when conjugated with targeting ligands [54, 55].

1.2.1.3 MRI

Nuclear magnetic resonance (NMR) spins are the atomic nucleus consisting of odd number of protons or neutrons. The most common spin is ^{1}H nuclei (proton) given the abundance of water in body tissue. An MRI scanner contains

three main components to create image: superconducting magnet, radiofrequency (RF) coils and gradient coils. When the random oriented protons are placed inside a strong static magnetic field (B0), they align either with (low energy state) or against (high energy state) the direction of the main magnetic field. The slight difference between the populations of these spins in these two energy states determines the net magnetization. RF pulse at the resonant frequency is generated by the RF coil perpendicular to B0 to manipulate the magnetization. The RF excitation provides the energy needed for spins to jump from low to the high energy level. The duration of the RF pulse is usually from one to several microseconds. Once turned off, the spins release the energy and generate the NMR signal which is detected by the RF coils in a process called relaxation. The patterns of relaxation, contributed by the energy transfer of spin-lattice and spin-spin interaction, are described as T_1 recovery and T_2 decay, respectively. T_2* decay depicts the energy release caused by both spin-spin interaction and field inhomogeneity.

NMR signal doesn't contain spatial information. In order to form an image, gradient coils are used to generate the spatial information by slice selection, frequency encoding and phase encoding. The image is then reconstructed by the Fourier Transform.

Contrast agents for MRI alter the relaxation time to modulate the signal. The most common contrast agents are gadolinium based. They are paramagnetic,

and thus shorten the T_1, T_2 and T_2* decay. Depending on the size and structure, they can be used as blood pool agents or extracellular fluid agent.

Magnetic particles consisting of iron oxide cores (Fe_3O_4) have been widely applied to MR imaging both as blood pool agents and targeted imaging. They accelerate T_2 and T_2* relaxation by the susceptibility effect and, therefore, are used as negative contrast agents. Superparamagnetic iron oxide (SPIO) particles, typically with the core size less than 30 nm in diameter[56], exhibit a number of appealing properties, such as strong effect on signal, high biocompatibility, and straightforward linkage to various functional groups. These advantages make SPIO a preferred material for labeling [57].

1.2.1.4 PET and SPECT

PET and SPECT use radioactive materials to form the imaging signal. Positron-emitting radiotracers are used in PET. When the positron emitted from the tracer counters an electron, they react and annihilate, releasing a pair of gamma photons at 511keV in opposite directions. Cameras capture the paired photons and calculate the location of the reaction. However the annihilation can only happen when the positron loses most of the kinetic energy and is moving very slowly, which means the positron has traveled from the tracer to the location of the reaction for a distance. The sensitivity of PET is hampered by the spatial resolution, which limits the capability to resolve tumor lesions less than 0.8cm^3

[58, 59]. The most widely used and successful PET tracer is ^{18}F-FDG. It assesses the metabolic level by measuring the glucose uptake. The low spatial resolution and high background prevent efficient localization [13, 60-63].

The most common SPECT tracers are ^{99m}Tc and ^{123}I, both of which are gamma-emitting radioisotopes. Scanner captures the gamma photons and the location of the tracers can be reconstructed in 3D.

Other limitations of PET and SPECT include the availability, radiation exposure and very costly scans.

1.2.1.5 Fluorescent imaging

The special property of fluorophores is the basis of FLI. Fluorophores can absorb photons of certain wavelength and emit photons of longer wavelength (lower energy). Fluorophores can be used to study the perfusion and enhanced permeability and retention (EPR) effect of tumor. Or they can be linked with a targeting component and used as probes to certain protein markers. Optical imaging has been rapidly adopted in cancer research because of a number of advantages such as high sensitivity, high throughput, cost-efficiency, and easy of use. However, the limited depth of tissue penetration, strong light scattering and the background auto fluorescence limit FLI to superficial or intra-operative exposed tumors. Light in the near-infrared range is favored as it falls into the

absorption window of hemoglobin and water, and thus can travel in tissue much efficiently [64].

1.2.1.6 Bioluminescent imaging

Bioluminescent imaging (BLI) is based on the expression of luciferase enzyme, and the presence of the substrate luciferin, oxygen, and ATP. Usually the animals are bearing tumors transfected to express luciferase. After injecting luciferin, the substrate circulates in blood stream and crosses the cell membrane. In the presence of luciferase, luciferin can react with oxygen and ATP and emit light. Different from FLI, there's no background auto fluorescence, so BLI is highly sensitive. This technique has been rapidly adopted in preclinical cancer research [65].

1.2.2 Vascular imaging techniques

The diagnostic values of tumor vasculature have been recognized and applied in varies techniques. Previously, the understanding of tumor vascular perfusion was largely based on invasive measurements of the micro-vessel density (MVD). Micro-vessels consisting of arterioles, venules and capillaries are responsible for the microcirculation in tissue. MVD depicts the number of micro-vessels in a defined microscopic area. Various tumor studies showed that the

MVD correlated with tumor stage, invasiveness and malignancy [66-68]. However, the invasive nature of biopsy prevents longitudinal MVD measurements along tumor progression and during treatment [69, 70].

Noninvasive imaging modalities have been exploited to image tumor vascular permeability. With the administration of contrast agent, several semiquantitative or quantitative physiological parameters can be obtained using sophisticated mathematical models. Dynamic contrast enhanced (DCE) MRI/CT/US can provide Blood Perfusion-Vessel Permeability (Ktrans), Extravascular-Extracellular Volume Fraction (ve), blood volume (BV), and blood flow (BF) [62, 71-75].

Arterial spin labeling (ASL) MRI has been widely used to image cerebral blood flow (CBF) and cerebral blood volume (CBV). However, applying background subtraction strategies in ASL techniques is difficult in small animal imaging due to the short arterial transit time [76, 77].

Dynamic susceptibility contrast (DSC) MRI has been used to study tumor vascularity. It is one of the most applied MR imaging techniques for brain perfusion measurement [78, 79]. With intravenous injection of conventional MR contrast agent, such as Gd-DTPA, the changes in relaxation rate are proportional to tissue contrast agent concentration. The hemodynamic information provided by the signal drop is particularly useful to assess CBV [80-83]. A series of T_2 or T_2* weighted images are usually acquired to capture the rapid passage of contrast

agent. Several groups have shown that the relative cerebral blood volume (rCBV) derived from DSC MRI correlates with tumor grade and malignancy [84-86]. It has also been reported to be useful in distinguishing high and low grade gliomas [87], lymphomas and GBM [88, 89], dural metastasis and meningioma [90], GBM and solitary breast cancer metastases in brain [91].

PET can also be used to obtain blood volume, through an infusion of radio tracer such as ^{15}O-H_2O [92], which are less frequently used due to the high cost and limited availability.

In addition, increasing microvessel diameters is often regarded as a sign of tumor progression. Such information can be obtained through a relative value referred to as the vascular caliber index, which is the BV ratio derived from T_2* and T_2 weighted sequences [93].

Blood oxygen level dependent (BOLD) MRI has also been used to evaluate the vessel maturity [94-96]. BOLD depends on the deoxyhemglobin level in blood. Due to the paramagnetic properties of both deoxyhemoglobin ($dHbO_2$), blood has been used as an endogenous agent to evaluate the capability of delivering oxygen to tissue.

The cellular and molecular biomarkers of angiogenesis and/or tumor vasculature can be visualized and quantified by various molecular imaging techniques. Targeted imaging that detects VEGF and $\alpha_v\beta_3$ have been studied extensively with PET [97, 98], SPECT [99, 100], targeted US with the use of

microbubbles [101] , MRI with iron oxide particles [98, 101] and FLI with near-infrared fluorophores [97, 99]. As aforementioned, PS, the highly sensitive and specific tumor vascular marker, has successfully been used in vascular targeted imaging in PET [102] and FLI [53].

Indeed, vascular imaging provides valuable insights for tumor identification, grading and prognosis. In Chapter two, I explore the feasibility of using DSC MRI to obtain rCBV longitudinally in animal models. In Chapter three, I used the SPIO conjugated with PGN635 to image tumor vasculature.

CHAPTER TWO
Longitudinal MRI evaluation of intracranial development and vascular characteristics of breast cancer brain metastases in a mouse model

2.1 ABSTRACT

Longitudinal MRI was applied to monitor intracranial initiation and development of brain metastases and assess tumor vascular volume and permeability in a mouse model of breast cancer brain metastases. Using a 9.4T system, high resolution anatomic MRI and dynamic susceptibility contrast (DSC) perfusion MRI were acquired at different time points after an intracardiac injection of brain-tropic breast cancer MDA-MB231BR-EGFP cells. Three weeks post injection, multifocal brain metastases were first observed with hyperintensity on T_2-weighted images, but isointensity on T_1-weighted post contrast images, indicating that blood-tumor-barrier (BTB) at early stage of brain metastases was impermeable. Follow-up MRI revealed intracranial tumor growth and increased number of metastases that distributed throughout the whole brain. At the last scan on week 5, T_1-weighted post contrast images detected BTB disruption in 160 (34%) of a total of 464 brain metastases. Enhancement in some of the metastases was only seen in partial regions of the tumor, suggesting intratumoral heterogeneity of BTB disruption. DSC MRI measurements of relative cerebral

blood volume (rCBV) showed that rCBV of brain metastases was significantly lower (mean = 0.89 ± 0.03) than that of contralateral normal brain (mean = 1.00 ± 0.03; $p < 0.005$). Intriguingly, longitudinal measurements revealed that rCBV of individual metastases at early stage was similar to, but became significantly lower than that of contralateral normal brain with tumor growth ($p < 0.05$). The rCBV data were concordant with histological analysis of microvascular density (MVD). Moreover, comprehensive analysis suggested no significant correlation among tumor size, rCBV and BTB permeability. In conclusion, longitudinal MRI provides non-invasive *in vivo* assessments of spatial and temporal development of brain metastases and their vascular volume and permeability. The characteristic rCBV of brain metastases may have a diagnostic value.

2.2 INTRODUCTION

Brain metastasis is the most common intracranial malignancy in adults. The prognosis is extremely poor, with a median survival of 4-6 months even with aggressive treatment. Breast cancer is one of the three major primary cancers with a high morbidity of brain metastasis (15 - 25%) [103-105]. Benefited from the routine mammography tests and improved therapeutic options, mortality of breast cancer has been decreasing in the past decade [106]. Advances in chemotherapy and immunotherapy played an important role in treating primary breast cancer as

well as its systemic metastasis. However, the incidence of brain metastasis seems to have increased over the past decade, especially within patients undergoing these systematic therapies [14, 107-109]. In part, this is due to the fact that most chemotherapeutic agents that show efficacy against systemic disease have poor penetration of blood-brain barrier (BBB). Brain metastases containing an intact BBB are hereby inaccessible to the therapeutics and remain untreated [110-112].

Current understanding for vascular development in brain metastases is largely based on invasive histological studies of animal models [19, 113]. Several brain-tropic cancer lines derived from primary melanoma, lung or breast cancer are capable of developing brain metastases upon intracardiac or intracarotid injection [114-117]. Using this model, several studies by others have applied molecular tracers to evaluate BTB permeability by measuring their uptake in brain metastases versus normal brain tissues on *ex vivo* brain sections. These studies have shown that BTB is intact at earlier stage of brain metastases, but becomes disrupted when the metastases grow larger [19, 113]. However, histological studies normally require a large number of mice that are killed at different time points after tumor implantation. More importantly, information about temporal development in individual lesions is lacking from histological studies.

In vivo imaging promises greater efficiency since each animal serves as its own control and multiple time points can be examined sequentially. Not only

intra- and inter-tumoral heterogeneity but also temporal comparison in the same individual lesions can be studied with longitudinal imaging. MRI that has a superb spatial resolution is the most widely used imaging modality for brain tumors of clinical patients. MRI at 1.5 or 3 T has previously been applied by others to study the intracardiac model of brain metastasis of breast cancer MDA-MB231Br (231Br) in mice or rats. Successful detection of multifocal brain metastases and alteration of BTB permeability based on the leakage of MR contrast agents has been reported in their studies [118, 119].

Tumor blood perfusion is another main factor that may affect efficient delivery of chemotherapeutics to brain metastasis. There are several noninvasive imaging modalities available for vascular perfusion assessment. Dynamic susceptibility contrast (DSC) perfusion MRI is one of the most applied MR imaging techniques for brain perfusion measurement [78, 79]. A series of T_2^*-weighted images is acquired to capture the rapid passage of gadolinium contrast agent post i.v. injection. The perfusion parameters extracted from decreased signal intensity during the first pass of the contrast are used to calculate cerebral blood volume (rCBV) and flow (rCBF) in a disease site relative to the contralateral healthy brain region. DSC perfusion MRI has been widely used for noninvasive assessment of tumor vascularity in both preclinical and clinical settings [120-122]. However, there are currently no studies that have assessed vascular perfusion and their changes with intracranial development of brain

metastases. The characteristics of the 231Br model containing multifocal brain lesions that are widespread throughout the whole mouse brain present a technical challenge. To facilitate intertumoral rCBV comparison within and between individual animals, in contrast to the widely-used single normal reference, we have developed a novel approach that utilizes multiple normal references contralateral to the tumor lesions.

In this study, I applied a high field 9.4 T MRI system to monitor longitudinal development of brain metastases based on T_2-weighted images after intracardiac inoculation of breast cancer MDA-MB231Br cells. Along with intracranial tumor growth, changes in BTB and tumor vascular volume, rCBV were evaluated by longitudinal T_1-weighted post contrast images and DSC perfusion-weighted MRI, respectively. Comprehensive analysis was performed to study correlations between tumor volume, BTB disruption and rCBV in individual metastases.

2.3 MATERIALS AND METHODS

2.3.1 Cell preparation

Brain-tropic human breast cancer MDA-MB-231/BR-GFP cell line (231-BR) was previously described [115, 123]. The 231-BR cells (kindly provided by Dr. Steeg, NCI) were incubated in Dulbecco's modified Eagle's medium

(DMEM) with 10% FBS, 1% L-Glutamine and 1% penicillin-streptomycin at 37^{o}C with 5% CO_2. Once 80% confluence was reached, the cells were harvested, and suspended in serum-free medium.

2.3.2 Breast cancer brain metastasis model

All animal procedures were approved by the Institutional Animal Care and Use Committee of University of Texas Southwestern Medical Center. Female nude mice (n = 9; BALB/c nu/nu, 6-8 weeks old; NCI, Frederick, MD) were anesthetized with inhalation of 2% isoflurane. 2 x 10^5 231-BR cells (in 100 µl of serum free medium) were injected directly into the left ventricle of a mouse heart under the imaging guidance of a small animal ultrasound (Vevo 770, VisualSonics; Toronto, Canada). The process can be seen in Figure 2-1.

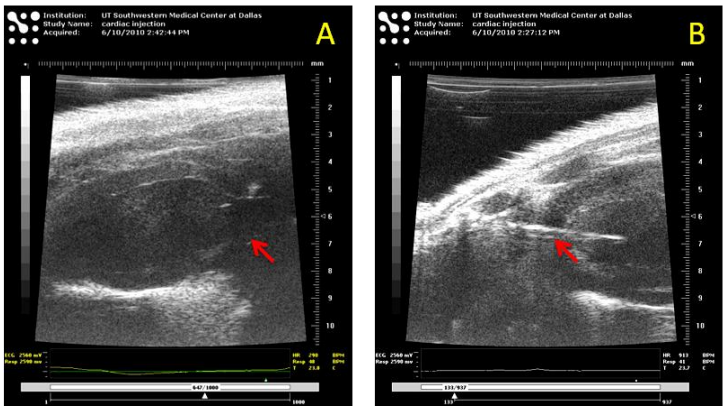

Figure 2-1 Ultrasound guided intracardiac injection.

(A) shows the left ventricle of the mouse heart, with an arrow indicating the aorta. (B) shows the needle (arrow) inside of the ventricle where the tumor cells were injected.

2.3.3 Monitoring the initiation and development of intracranial tumors using MRI

MRI was initiated two weeks after tumor implantation and repeated once a week for up to three weeks. Animals were sedated with 3% isoflurane and maintained under general anesthesia (1.5% isoflurane). Animal body temperature and respiration were monitored and maintained constant throughout the experiment. MR measurements were performed using a 9.4T horizontal bore magnet with a Varian INOVA Unity system (Palo Alto, CA). A tail vein of mouse was catheterized using a 27G butterfly for Gd-DTPA (Magnevist®; Bayer HealthCare, Wayne, NJ) contrast agent administration. High resolution multi-slice (14 slices with 1mm-thick, no gap) T_1- and T_2-weighted coronal images, covering the region from the frontal lobe to the posterior fossa, were acquired with the following parameters: T_1-weighted images: spin echo multiple slice (SEMS), TR/TE = 400 ms/20 ms, matrix: 256 x 256, FOV 20 x 20 mm, in plane resolution: 78 x 78 μm^2. T_2-weighted images: fast spin echo multiple slice (FSEMS) sequences, TR/TE = 2500 ms/48 ms, 8 echo trains, matrix: 256 x 256, FOV 20 x 20 mm, in plane resolution: 78 x 78 μm^2. The tumor size was determined on T_2-weighted images by manually outlining the enhancing portion of the mass on each

image by using MatLab (Mathworks, Natick, MA) programs written by us. With high spatial resolution, hyperintense lesions can be identified as small as 310 μm in diameter. Since the metastases in this study were very small and development of necrosis and edema was minimal, the hyperintense lesion on T_2-weighted images truly represented the tumor mass. Given most of the tumor diameters were smaller than the slice thickness (1 mm), the tumor size was presented as in plane area rather than the volume.

2.3.4 Dynamic susceptibility contrast (DSC) perfusion MRI

Once brain lesions were identified on T_2-weighted images, DSC MRI was performed on 4 of the slices containing most of the metastases. A series of GEMS T_2^*-weighted images over 5 mins was acquired before and after a bolus injection of Gd-DTPA contrast (0.1 mmol/kg body weight) via a tail vein. DSC MRI parameters: TR/TE = 27 ms/4 ms, FA = 20°, matrix: 64 x 64, FOV 20 x 20 mm, number of slices = 4 with 1mm thick. Raw data of signal intensity were extracted from the image series on a voxel-by-voxel basis and plotted into a time course curve. ΔR_2^* was calculated using equation:

$$\Delta R_2^* = \frac{-\log(S_t/S_0)}{TE} \qquad \text{eq(1)}$$

where St is the signal intensity (SI) of each time point, S_0 is the mean SI of baseline, and TE is the echo time. First-pass pharmacokinetic modeling (FPPM) fitting [124] was applied to ΔR_2^* curve to detect the starting and the ending points of the bolus. The equation used for this step is as follows:

$$C_t = Xs(p_i;t) + Y\int_0^t s(p_i;t')\exp(-k_{ep}(t-t'))dt' \qquad \text{eq(2)}$$

Where $X = Av_p;$ $Y = AK^{trans};$

And the bolus shape function is defined as:

$$s = g(t) + \lambda\int_0^t g(t-t')dt'$$

Where $$g = \begin{cases} (t-t_0)^{\alpha}\exp(-\beta(t-t_0)) & t > t_0 \\ 0 & t < t_0 \end{cases}$$

Baseline correction was separated into three parts. Pre-bolus baseline was set to zero. Then, a linear fit was applied from this point to the end of the data to obtain post bolus baseline, and connection of this two segments served as the under-bolus baseline (as shown in green dotted line in Figure. 2-3 B). Subtraction of ΔR_2^* with baseline obtained in previous step provided a corrected ΔR_2^*. CBV was calculated from the gamma-variate fitting applied to the corrected curve and

the area under the fitted curve was proportional to CBV [121]. Gamma fitting was obtained using the following equation:

$$\Delta R_2^* = k(t - t_0)^{\alpha} e^{\frac{-(t-t_0)}{\beta}} \qquad \text{eq(4)}$$

ROIs of brain metastases were drawn based on the high resolution T_2-weighted images. The corresponding contralateral normal ROIs were selected symmetrically to the tumor ROIs according to the distinct landmarks in brain, such as ventricles, hippocampus and the interfaces of different anatomical structures. In cases where the contralateral sites appeared abnormal, neighboring regions in the same anatomical structure were selected instead. The mean CBV value of all the normal ROIs in each animal served as the reference. rCBV for both individual metastases and the normal brain was determined by normalizing the CBV to the reference CBV. Analysis was performed on a home written MATLAB program. A color-coded rCBV map was obtained and overlaid on the corresponding T_2-weighted image.

2.3.5 Brain tumor barrier (BTB) permeability

T_1-weighted spin echo multislice images were immediately acquired after DSC MRI, about 5 mins post contrast injection to evaluate BTB permeability. A

non-permeable metastasis is isointense, while a permeable metastasis appears hyperintense to surrounding brain tissue on T_1-weighted post contrast image.

2.3.6 Histological and immunohistochemical studies

Animals were sacrificed immediately after the last MR follow-up and the brain was dissected and frozen for preparation of cryosections. H&E staining was performed on coronal brain sections (10 μm), while their adjacent sections were used for immunohistological staining. Vascular endothelium was stained using a rat anti-mouse CD31 antibody (Serotec Inc., Raleigh, NC) followed by Cy3-labeled goat anti-rat IgG (Jackson Immunoresearch Laboratory, West Grove, PA). Fluorescence images of tumor cells (green, GFP) and vasculature (red) were captured on the same microscopic field using a Coolsnap digital camera mounted on a Nikon microscope and analyzed with MetaVue software (Universal Imaging Corporation). Microvascular density (MVD) was calculated as follows: mean number of red vessels / mean area of green tumors. A total of twelve metastases and their contralateral normal brain tissues in 3 tumor-bearing mouse brains were evaluated.

2.3.7 Statistical analysis

Statistical analysis was conducted using R (R Development Core Team, 2012), a language and environment for statistical computing. A natural log transformation was applied to all the rCBV values to achieve normal distribution before Student's t-test was performed for significance analysis. The statistical analysis of correlation was based on Regression and Bivariate plots (SAS Inst. Inc., Cary, NC). Two sample paired Student's t-test was performed to evaluate the significant difference of rCBV or MVD of tumor and its contralateral reference tissue. After dividing tumors into two groups based on the permeability status, comparison of rCBV or tumor size between these two groups was evaluated using unpaired t-test. Paired t-test was performed for longtitudinal studies to assess the changes of individual lesions over time.

2.4 RESULTS

Ultrasound imaging-guided left ventricular injection of brain-tropic breast cancer 231BR cells ensured the accuracy so that every animal in this study developed brain metastases, as compared to a success rate of 50% with the manual injection used in previous studies. Longitudinal MRI monitoring was initiated 2 weeks post injection and repeated once a week for up to 3 more weeks (Figure.2-2). With the high spatial resolution of T_2-weighted images, metastatic lesions, appearing as hyperintense, became visible in mouse brain 3 or 4 weeks

post injection; the minimum detectable tumor was ~310 μm in diameter, whereas all of these early stage metastases were isointense on T_1-weighted post contrast images (Figures. 2-2 A and 2-6 A). Follow-up scans revealed increased tumor size and appearance of new lesions (Figures. 2-2 A and 2-6 A), which correlated well with H&E staining (Figure. 2-2 B). A total of 464 metastases, with a size ranging from 0.09 mm^2 to 1.7 mm^2, in 9 mice were depicted on T_2-weighted images of the last MR follow-up at week 5. These metastases distribute throughout the mouse brain with a higher incidence in the cerebral cortex (49%), whereas the least number in the thalamus, midbrain or cerebellum (5%; Figure. 2-2 C). Of these metastases, 160 (34%) lesions were enhanced on T_1-weighted post contrast images, indicating a locally disrupted BTB (Figures. 2-2 A, 2-4 and 2-6 A). However, enhancement in some of the metastases was only seen in partial regions of the tumor (Figure. 2-4 A), suggesting intratumoral heterogeneity of BTB disruption.

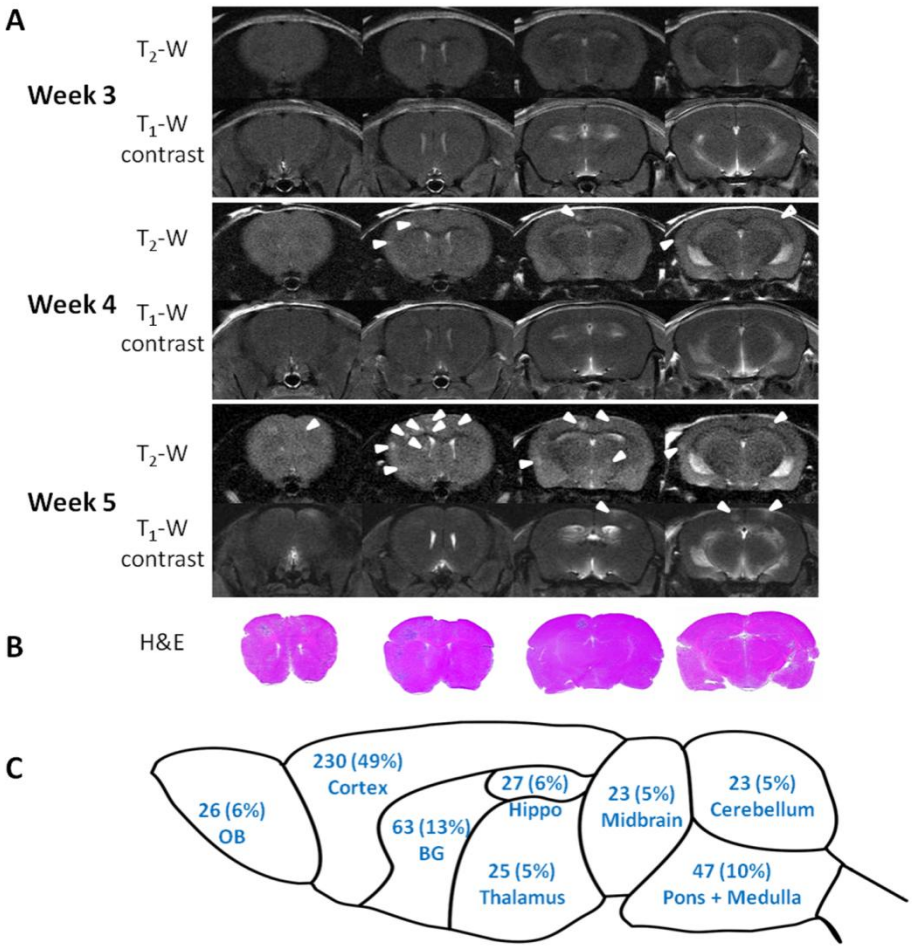

Figure 2-2 Longitudinal MRI monitoring the initiation and development of intracranial brain metastases.

(A) MRI scans of the whole mouse brain were initiated 3 weeks after intracardiac injection of MDA-MB231Br cells and repeated once a week for 2 weeks. Four consecutive coronal MRI sections of a representative mouse brain showed no apparent intracranial lesions on T_2-weighted images. However, follow-up images at week 4 identified multiple lesions with hyper-intensity on T_2-weighted images (arrowhead), but none of them was enhanced on T_1-weighted post contrast images. An increased number of lesions (arrowheads) appeared on the images at week 5, only a few of which (arrowheads) were enhanced post Gd-DTPA. (B) Corresponding histological sections of H&E staining showed a good correlation with MRI. (C) MRI evaluation of a total of 464 metastases in 9 mice brains indicated that these metastases distributed through the whole mouse brain with a

higher incidence in the brain cortex (49%). Note: OB: Olfactory bulb; BG: Basal ganglia; Hippo: Hippocampus.

Dynamic susceptibility contrast (DSC) MRI, based on a bolus injection of contrast agent Gd-DTPA into a tail vein, was applied for rCBV measurement (Figure. 2-3 A). The first pass of the contrast via brain vasculature was clearly depicted as the dip region in the signal intensity time cure (Figure. 2-3 B). A color-coded rCBV map of a normal mouse brain, projected on the T_2-weighted image, showed the high level of symmetry between hemispheres and significant higher rCBV in the cortical regions (Figure. 2-3 C). For brain metastases-bearing mice (n =9), 212 of the 464 metastases, identified at the last scan, were subject to rCBV measurements and compared with their contralateral normal brain. As shown in Figure. 2-4, the metastatic lesions were found to have significantly lower rCBV, compared to their contralateral normal brain (mean = 0.89 ± 0.0.03 (s.e.) vs. 1.00 ± 0.03 (s.e.), $p < 0.005$; Figure. 2-4 C). It is important to notice marked heterogeneity in rCBV between individual metastases, ranging from 0.16 to 2.84 (Figures. 2-4, 2-5 and 2-6). This is also true for rCBV in normal brain, as demonstrated in Figure. 2-3. Thus, it is necessary to compare rCBV between a specific metastasis and its contralateral normal brain. Further analysis showed no significant correlation between rCBV and tumor size ($R^2 < 0.02$; Figure. 2-5 A). When these metastases were separated into the permeable (n = 70) and non-permeable (n = 142) group, determined by whether it is enhanced by T_1 contrast

agent, the data showed that neither rCBV (mean = 0.88 ± 0.04 vs. 0.90 ± 0.03; $p > 0.1$; Figure. 2-5 B) nor tumor size (mean = 0.49 ± 0.11 mm^2 vs. 0.47 ± 0.14 mm^2; $p > 0.1$; Figure. 2-5 C) significantly differed between the two groups.

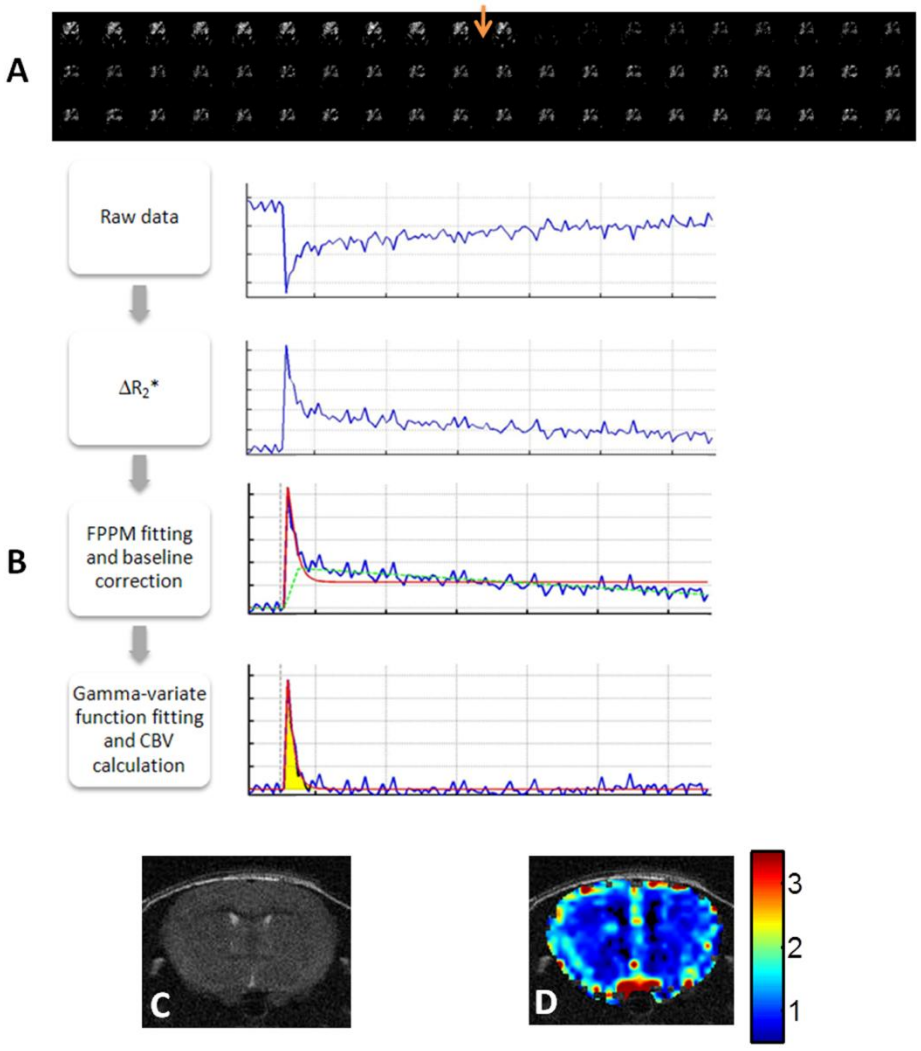

Figure 2-3 Dynamic susceptibility contrast (DSC) MRI of rCBV.
(A) A series of T_2^*-weighted images of a mouse brain was acquired before and after a bolus injection of the contrast agent, Gd-DTPA via a tail vein (arrow). Immediately after the injection, significant loss in signal intensity was observed,

which gradually recovered to the baseline level 5 mins later. (B) The flowchart illustrates the data process of DSC MRI to generate rCBV map. Raw data of DSC MRI signal versus time curve was first plotted, depicting the first pass of the contrast agent via the brain as the dip on the curve. The ΔR_2^* was then calculated from the signal time course. FPPM was applied to determine the general trend of ΔR_2^* and a three-segment baseline was generated. Finally, Gamma-variate fitting was used to correct ΔR_2^*, and the area under the bolus was calculated, which is proportional to CBV. (C) An anatomic T_2-weighted image was obtained from a normal mouse brain. A color-coded rCBV map generated from DSC MRI was overlaid on the T_2-weighted image showing symmetric distribution of rCBV between the two hemispheres (D).

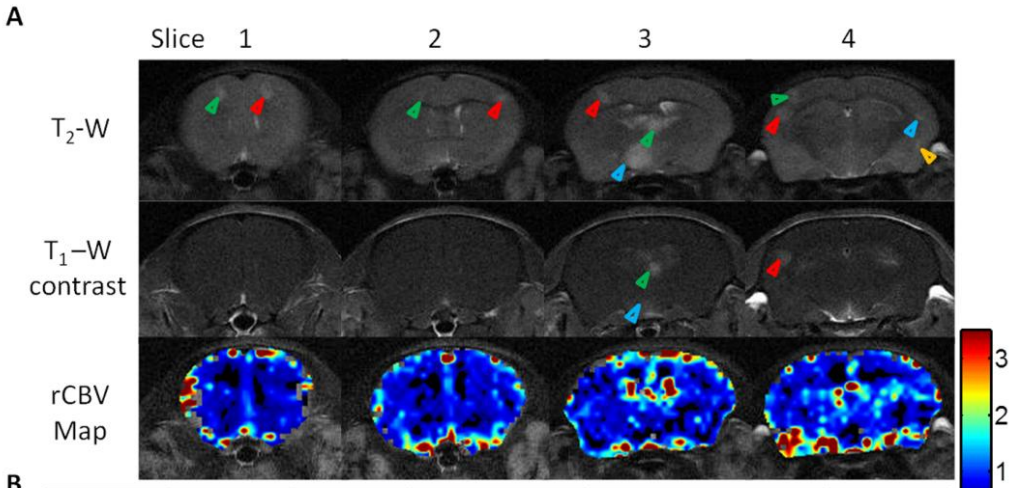

B

	slice 1		slice 2		slice3			slice4				Mean
Mets	0.72	0.60	1.19	0.45	0.54	1.12	0.68	0.57	1.04	0.83	0.56	0.76±0.08
Contralateral	1.09	1.13	0.58	0.78	0.88	1.61	0.41	0.81	0.97	1.04	1.71	1.00±0.12

Figure 2-4 Significantly lower rCBV in brain metastases than contralateral normal brain.

(A) Four weeks after intracardiac injection of 231Br cells, T_2-weighted MRI revealed multiple high signal intensity lesions (arrowheads) on four consecutive coronal sections of a representative mouse brain. Only a few of the lesions (arrowheads) were enhanced on T_1-weighted post contrast images, one (blue arrowhead in the third section) of which showed partial enhancement, indicating intratumoral heterogeneity of BTB disruption. rCBV maps of the four sections were generated and overlaid on the T_2-weighted images. (B) The rCBV values of the metastatic lesions and their contralateral normal brain were obtained and

summarized in the table. Note the color presented in the table coincides with the color of arrowhead on each of the MR images. Most of metastatic lesions had lower rCBV values than their contralateral counterparts of normal brain.

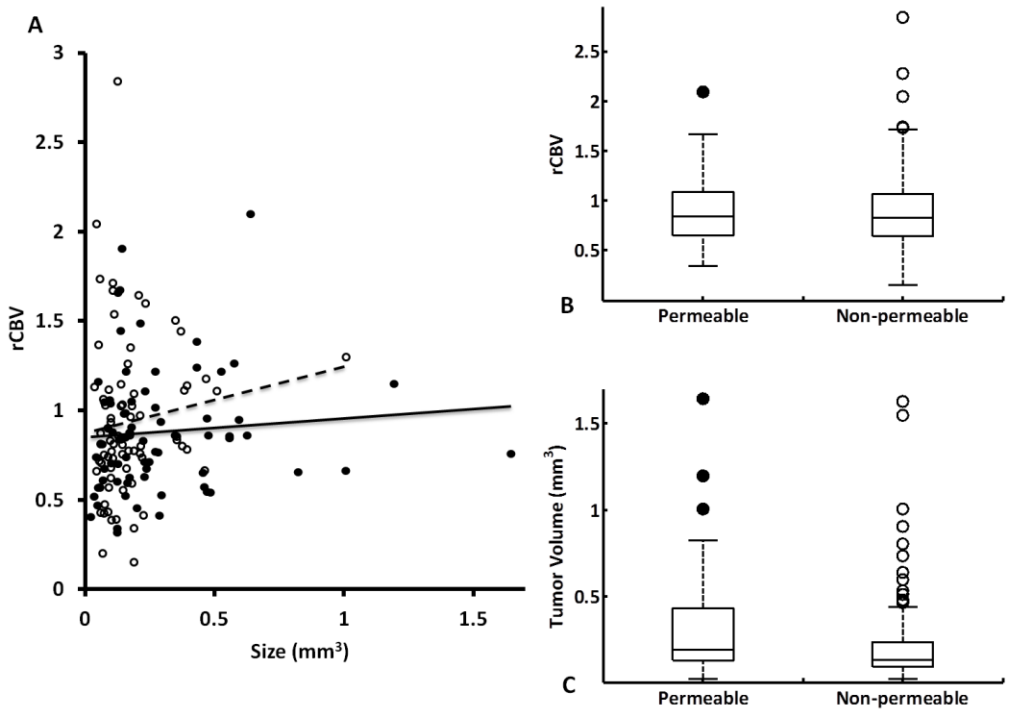

Figure 2-5 Lack of correlation between rCBV, tumor size and permeability of brain metastases.

Based on T_1-weighted contrast enhanced MRI, the 212 metastases studied by DSC MRI were separated into the permeable (enhanced, n = 70) and non-permeable (not enhanced, n = 142) group. **A.** A plot of rCBV versus individual tumor size showed no correlation in either the permeable (filled; $R^2 = 0.01$) or non-permeable group (empty; $R^2 < 0.02$). **B.** The rCBV values of the permeable lesions (median = 0.84, ranging from 0.34 to 2.10) were not significantly different from those of the non-permeable ones (median = 0.82, ranging from 0.16 to 2.84; $p > 0.1$). **C.** Further comparison found no significant difference in tumor size between the permeable (mean = 0.49 ± 0.11 mm^2) and the non-permeable (mean = 0.47 ± 0.14 mm^2; $p = 0.1$) metastases.

Longitudinal MRI studies allowed *in vivo* non-invasive evaluation of tumor growth and changes in BTB permeability and rCBV of individual brain metastases. Thirty two metastases that were identified from 5 of the 9 mouse brains in the scans of week 3 were followed a week later. As shown in a representative mouse brain in Figure. 2-6, five small hyperintense metastases first appeared on T_2-weighted images at week 3. All the 5 lesions grew larger, along with many other new lesions becoming visible in the following week's scan. All the 5 lesions showed no enhancement on T_1-weighted contrast images at week 3, only one of them became enhanced at week 4. DSC MRI found that rCBV values decreased in 4 of the 5 metastases (Figure. 2-6 B). For a total of 32 metastases, rCBV values were initially similar to those of their contralateral normal brain (mean = 1.05 ± 0.05 vs. 0.96 ± 0.04), but decreased significantly and became significantly lower than those of their contralateral normal brain in the late scan (mean = 0.88 ± 0.06 vs. 1.00 ± 0.06, $p < 0.05$; Figure. 2-6 C).

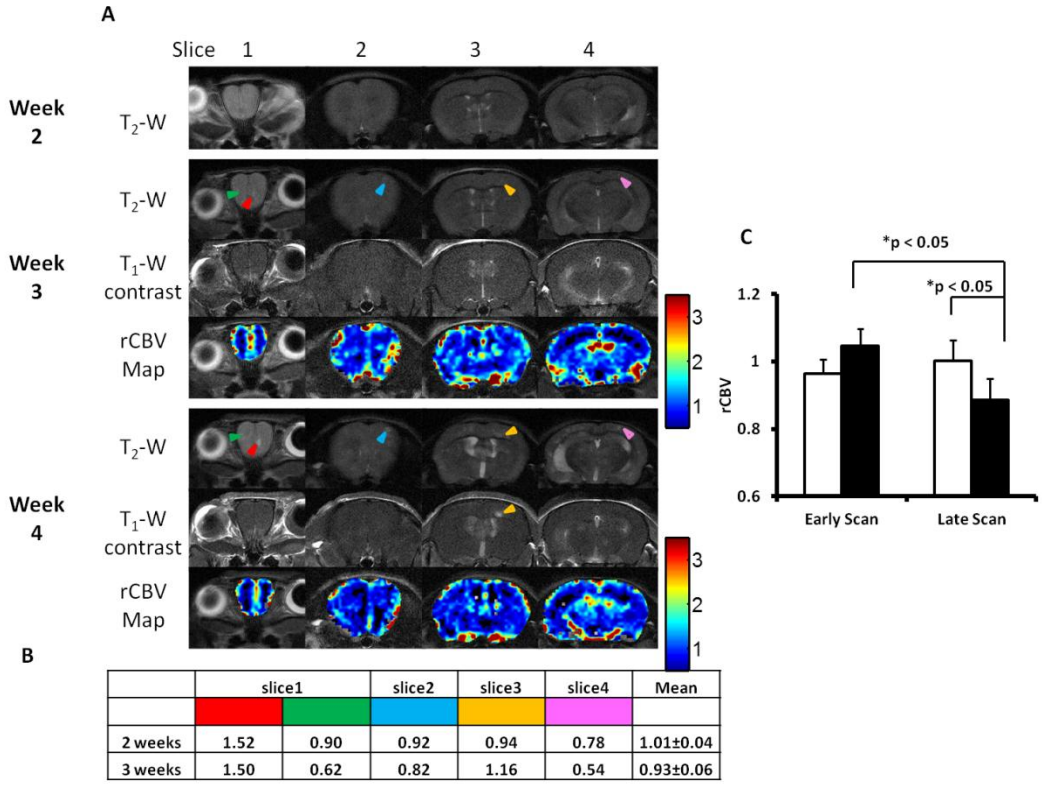

	slice1		slice2	slice3	slice4	Mean
2 weeks	1.52	0.90	0.92	0.94	0.78	1.01±0.04
3 weeks	1.50	0.62	0.82	1.16	0.54	0.93±0.06

Figure 2-6 Longitudinal MRI study of changes in BTB permeability and rCBV of brain metastases.

(A) Longitudinal MRI of a representative mouse brain was initiated 2 weeks after intracardiac injection of 231Br cells. At week 3, five small metastases (arrowhead) were identified on four consecutive T_2-weighted coronal images. At week 4, many more lesions appeared on T_2-weighted coronal images, while all the 5 lesions seen on week 3 were found to increase in size (arrowhead). Changes in BTB permeability and rCBV were then evaluated for these five lesions. There was initially no contrast enhancement seen in the five tumors at week 3, indicating an intact BTB. All the tumors except one (yellow arrowhead) still kept BTB intact at week 4. rCBV maps were created and rCBV values of the tumors were presented in the table (B). (C) A total of 32 lesions in 5 animals were seen on both scans of weeks 3 and 4. rCBV of brain metastases (solid) was initially similar to that of contralateral normal brain (open; mean = 1.05 ± 0.05 (se) vs. 0.96 ± 0.04), but decreased significantly ($p < 0.05$) and became significantly lower as compared to their contralateral normal brain in the late scan (mean = 0.88 ± 0.06 vs. 1.00 ± 0.06; $p < 0.05$).

Immunohistochmical staining of vascular endothelium (CD31) showed that MVD was 669 ± 201/mm^2 within the metastatic lesions (n = 12), which was significantly lower than that of the contralateral normal brain (965 ± 177/mm^2; $p < 0.05$; Figure. 2-7). Moreover, in contrast to the normal brain comprising of regularly-shaped micro-vessels, the irregular and dilated vessels were often seen for tumor vessels (Figure. 2-7).

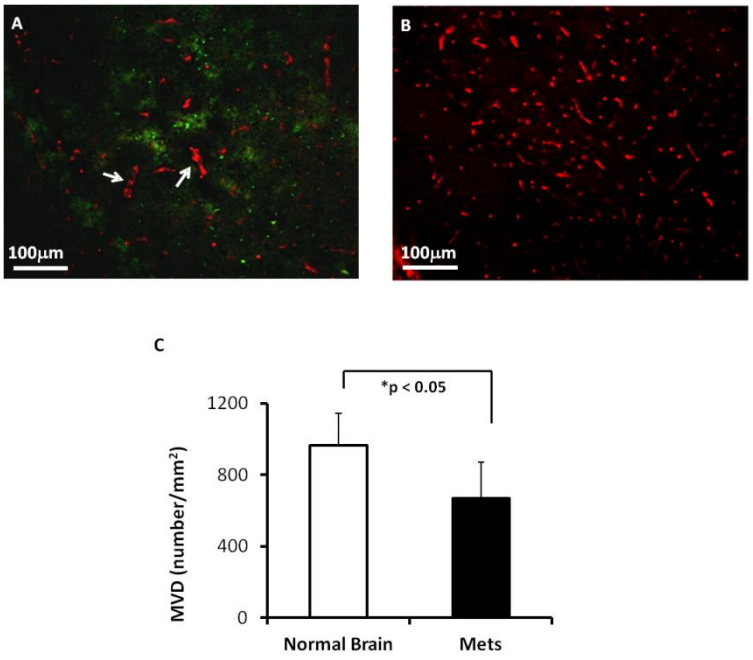

Figure 2-7 Immunohistochemical study of microvascular density (MVD) in brain metastases.
(A) Anti-CD31 staining was performed on a brain section bearing metastases. A cortical lesion (~ 600 μm in diameter) was depicted with green fluorescence (GFP). Microvessels (red) within the lesion appeared less dense, as compared to abundant fine vessels in the contralateral normal brain tissues (B). Some of the tumor vessels were irregular in shape and larger in diameter (arrow). (C) Quantitative data of MVD showed a significantly lower MVD in brain metastases versus contralateral normal brain (mean = 669 ± 201/mm^2 vs. 965 ± 177/mm^2; $p < 0.05$).

2.5 DISCUSSION

In the present study, I demonstrated the utility of longitudinal MRI to evaluate intracranial growth and vascularity of breast cancer brain metastases in a mouse model. Using the 9.4T MRI, high resolution T_2-weighted images enabled the detection of multifocal tumor initiation at a diameter of as small as 310 μm. Longitudinal monitoring of BTB permeability based on T_1-weighted contrast enhanced images revealed that BTB in early-stage (week 2 or 3) brain metastases were exclusively impermeable; even at the late stage (week 4 or 5), T_1 contrast enhancement was only found in a small proportion (34%) of brain metastases, indicating that the BTB is still intact in the majority of the metastases (Figures. 2-2, 2-4 and 2-6). This observation is in good agreement with a recent MRI study of the 231BR brain metastases mouse model. In that study, Percy et al [118] observed no contrast enhancement for brain metastases by day 20, while 28% of the metastases by day 30 appeared hyperintense on T_1-weighted post contrast images. The MRI data are consistent with histological studies conducted previously by others. Zhang et al [113] administered fluorescent dye, sodium fluorescein systemically into the mice bearing brain metastases to study BBB permeability. The microscopic observations on brain sections showed differential permeability of the dye among the metastases, of which lesions smaller than 0.2

mm^2 had intact BBB, while larger metastases were leaky because of tumor angiogenesis and/or central necrosis [113]. Although my data indicates that the mean tumor size of permeable metastases was larger than that of the non-permeable ones, there was no significant difference in tumor size between the two groups (Figure. 2-5 C). Similarly, lack of correlation between tumor size and BBB disruption was reported in a recent study by Lockman et al., suggesting other factors may also be involved in this dynamic process [19].

On many occasions, enhancement on T_1-contrast images was only seen in partial regions of the tumor (Figure. 2-4 C), implicating inhomogeneous disruption of BTB. This finding concurs with a recent study of biodistribution of anti-cancer drugs in brain metastases [19]. Lockman and colleagues assessed the uptake of radio-labeled paclitaxel or doxorubicin in brain metastases of MDA-MB231Br-Her2 mouse model. Heterogeneous intratumoral distribution of the chemotherapeutics was clearly visualized on *ex vivo* brain sections by phosphorescence. Even in the most permeable metastases, the drug concentrations were far below that in visceral metastases [19]. Taken together, all these data support the notion that systemic anti-cancer therapeutics has limited utility in treating brain metastases.

Despite its small molecular weight (MW ~ 500), the hydrophilic MRI contrast, Gd-DTPA is found not to penetrate across the intact BBB and is thus suitable for BBB permeability study. Many strategies to overcome this barrier

have been exploited to facilitate the delivery of effective anti-cancer therapeutics into brain tumors, i.e, hemispherical opening of the BBB using high-concentration intra-carotid injections of mannitol or temporary disruption of localized BBB by high-intensity focused ultrasound [125, 126]. Thus, it is critical to develop a means to enable non-invasive evaluation of BBB damage after exposure to intervention in order to predict drug delivery. Indeed, Treat et al recently reported a linear correlation between T_1 signal intensity post Gd-DTPA and doxorubicin concentrations in brain regions after BBB damage induced by sonication [127].

Perfusion MRI has been widely used to provide important diagnostic and prognostic information on pathological conditions. Arterial spin labeling (ASL) MRI, utilizing magnetically tagged arterial blood as endogenous contrast has proven it feasible in quantitative measurements of rCBF and rCBV in clinical studies [128, 129]. However, the low sensitivity and poor signal to noise ratio (SNR) of ASL perfusion MRI limits its application to mouse brain. Dynamic contrast susceptibility (DSC) MRI acquired after infusion of MRI contrast agents is another technique to measure rCBV. DSC MRI has been widely applied to study microvasculature and hemodynamics in brain tumors. Recent studies have correlated DSC MRI of rCBV with histological grade and degree of neovascularization in human glioma [121, 130, 131]. In a preclinical mouse glioma study, a positive correlation between rCBV and tumor microvascular density (MVD) was found [122]. However, little is known about rCBV

abnormality of brain metastases, in particular, its variation among individual brain metastases as well as its alteration with tumor development.

My data showed marked heterogeneity of rCBV for both normal brain and metastatic lesions (Figures. 2-3 and 2-5). To acquire an rCBV value of a lesion, a region of normal brain needs to be chosen to serve as a reference. Previously published clinical or preclinical works on vascular perfusion of a solitary brain tumor have utilized either a region of white matters or the normal brain contralateral to the tumor as a single reference [121]. The intracardiac brain metastasis model used in this study developed multiple intracranial lesions. As shown in Figure. 2-2, these multifocal metastases distributed well throughout the whole mouse brain. It is difficult to define a specific region of normal brain that can be used as a common reference for each individual case. Moreover, given the marked heterogeneity in vascular perfusion of normal brain, we applied multiple normal regions that locate contralaterally to the individual metastases as the references. The mean CBV value of all the normal ROIs in each animal was used to serve as the reference for both metastatic lesions and normal brain regions. In cases where the contralateral sites appeared abnormal, neighboring regions in the same anatomical structure were selected instead. As shown in Figure. 2-3 D, using this approach, the reliable rCBV map was generated in a normal mouse brain. We believe that this approach can significantly minimize the individual variation and facilitate a comparison of rCBV between individual animals.

DSC MRI measurement of rCBV revealed significantly lower rCBV of brain metastases (mean = 0.89 ± 0.03) than that of contralateral normal brain (mean = 1.00 ± 0.03; $p < 0.005$). The rCBV data were concordant with histological findings that MVD within the metastases was significantly lower than that of contralateral normal brain. Fidler's group has documented that the MVD within the metastases was 20 times lower that in the surrounding normal brain [113]. Unlike the robust angiogenesis observed in primary high grade glioma, vessel sprouting, the characteristic of angiogenesis is rarely seen in brain metastases. Instead, dilation of blood vessel lumen, as shown in Figure. 2-7, and reported elsewhere in both the experimental brain metastases and surgical specimens of human lung cancer brain metastases, is considered as a result of the division of endothelial cells [113, 132]. The characteristic rCBV may have a diagnostic value for brain metastases to differentiate them from those highly vascularized and perfused malignant gliomas.

Longitudinal MRI allows rCBV of individual brain metastases to be examined over time. Intriguingly, our data showed that rCBV of individual metastases at early stage was similar to, but became significantly lower than that of their healthy counterparts at the late stage of tumor development (Figure. 2-6 C; $p < 0.05$). By using multiphoton laser scanning microscopy and a mouse cranial window model, Kienast et al. followed in real time brain metastasis formation from lung cancer and melanoma in mouse brain. After extravasation,

the metastatic cells grow along the preexisting normal brain vessels [133]. In another study, Kusters et al. showed that a melanoma brain metastasis could grow up to 3 mm through co-opting preexisting blood vessels without induction of an angiogenic switch [134]. All these data indicate that there is no angiogenic compensation for the tissue volume increase at the lesion site, resulting in a lower MVD and rCBV, as compared to normal brain. For the pooled data, however, we found that rCBV was not correlated with either the size or permeability of metastasis (Figure. 2-5 A and B), implicating that the intertumoral heterogeneity of rCBV may result from regional variation in vascularity in normal brain where metastases locate.

In summary, I applied 9.4T MRI to study brain metastases formation after intracardiac injection of breast cancer MDA-MB231Br-GFP cells into mice. High resolution T_2-weighted MRI enables the detection of multifocal metastases at early stage. MRI contrast, Gd-DTPA based T_1-weighted contrast enhanced MRI and T_2^*-weighted DSC MRI allow non-invasive characterization of vascular permeability and blood volume during intracranial development of brain metastases. Significantly lower BTB permeability and vascular volume in brain metastases than that in normal brain underscore the urgent need to develop brain permeable drugs or a means to alter the BTB permeability in order to achieve therapeutic concentrations of anti-cancer therapeutics.

Acknowledgments: This work was supported in part by the DOD IDEA Awards W81XWH-08-1-0583. MRI experiments were performed in the Advanced Imaging Research Center, an NIH BTRP # P41-RR02584 facility, and ultrasound-guided intracardiac injection was performed with VisualSonics Vevo 770 under 1S10RR02564801. Thanks to Dr. Ming Chen for his help in statistical analysis. I am grateful to Dr. Glyn Johnson, New York University School of Medicine and Mr. Jason Reneau for technical and collegial support.

CHAPTER THREE
Phosphatidylserine (PS) targeted molecular MRI of tumor vasculature

3.1 ABSTRACT

Phosphatidylserine (PS), normally restricted to the inner leaflet of the plasma membrane, becomes exposed on the outer surface of viable (non-apoptotic) endothelial cells in tumor vasculature, but not in normal blood vessels. In the present study, we report the use of *in vivo* molecular MRI to detect exposed PS on tumor vasculature of 4T1 breast cancer based on a novel human monoclonal antibody, PGN635 that specifically targets PS. The $F(ab')_2$ fragments of PGN635 were conjugated to polyethylene glycol (PEG) coated paramagnetic iron oxide nanoparticles (IO). SPIO-PGN635 was able to specifically bind to exposed PS on vascular endothelial cells or tumor cells, induced by irradiation. Systemic administration of SPIO-PGN635 into mice bearing subcutaneous 4T1 tumors confirmed tumor vascular localization of the nanoprobes by histological studies. At 9.4 T MRI, longitudinal T_2-weighted images detected inhomogeneous signal loss in tumor as early as 2 h post i.v. injection of SPIO-PGN635. Irradiation induced a significant increase in PS exposure on tumor vascular endothelia, resulting in significantly more hypointense regions in tumor seen on MRI ($p < 0.05$). Localization of SPIO-PGN635 to tumor blood vessels was

antigen specific, since SPIO-Aurexis, a control probe of irrelevant specificity, showed minimal localization to the tumors. Our studies suggest that tumor vasculature can be successfully imaged *in vivo* by MRI to provide sensitive tumor detection.

3.2 INTRODUCTION

Molecular imaging of angiogenesis has recently been demonstrated using ligands that target biomarkers that are selectively exposed on tumor vasculature. The integrin alpha v beta III ($\alpha_v\beta_3$), which is overexpressed on the surface of tumor vascular endothelial cells, has been the most widely used target to imaging tumor angiogenesis. Various imaging contrast agents have been conjugated to $\alpha v\beta 3$ binding ligands, such as Arginine-Glycine-Aspartic Acid (RGD)-containing peptide, for optical imaging, PET, SPECT and MRI [98, 100]. In addition to its overexpression in angiogenic endothelial cells (EC), $\alpha_v\beta_3$ and several other integrins are found to present abundantly on tumor cells to play an important role on mediating interaction between tumor cells and their extracellular environment. In particular, significantly higher expression of $\alpha_v\beta_3$ has been observed in tumor cells of clinical glioblastoma (GBM). A recent study by Schnell, *et al.* has exploited [^{18}F] Galacto-RGD for PET imaging of $\alpha_v\beta_3$ expression in GBM patients [135].

Phosphatidylserine (PS) is the most abundant anionic phospholipid of the cell membrane. It has recently been observed that PS becomes exposed on the outer surface of viable endothelial cells in tumor blood vessels [43, 46, 47]. Although exact mechanisms are not fully understood, studies have shown that characteristics of tumor environment, in particular, hypoxia, acidity, inflammatory cytokines and the elevated ROS level contribute to PS exposure on ECs [43, 50, 51]. Vascular endothelium in normal tissues, even in these highly angiogenic ovarian blood vessels during the menstrual cycle, lacks exposed PS. Along with its localization on vascular lumen, PS represents an ideal biomarker for vascular targeted imaging. Dr. Thorpe's group has developed a series of monoclonal antibodies that recognize PS with higher specificity than Annexin V (A5). The antibodies bind to PS complexed with the PS-binding protein, β2-glycoprotein I (β2GP1) [43]. Bavituximab, a chimeric monoclonal PS-targeting antibody, is in advanced clinical trials in patients with lung and breast cancer [136, 137].

A new, fully human monoclonal PS targeting antibody, PGN635 has recently been developed. Like bavituximab, PGN635 has a high specificity and affinity to PS (Kd $\approx 10^{-10}$ M). $F(ab')_2$ fragments of PGN635 were conjugated to an NIR dye, IRDye800CW in the previous study. The 800CW-PGN635$F(ab')_2$ enabled sensitive and clear optical imaging of glioma of mouse models [53]. However, due to its inherent low spatial resolution and depth penetration, optical imaging provided little spatial information about intratumoral distribution of the

probes. In the present study, I extended this research to molecular MRI because MRI is commonly used imaging modality with high spatial resolution and excellent soft tissue contrast. I conjugated amino-terminal PGN635F(ab')$_2$ to carboxyl group on the distant terminus of PEG chains that are coating the paramagnetic iron oxide nanoparticles (IO). Specificity of SPIO-PGN635 binding to exposed PS was first studied *in vitro* on cultured vascular endothelial cells and tumor cells by histological staining and MRI. High field 9.4 T MRI was then applied to detect T_2-weighted signal intensity change in subcutaneous 4T1 tumors post i.v. injection of SPIO-PGN635. To explore whether SPIO-PGN635 could be used to monitor dynamic changes in levels of exposed PS, 4T1 tumors were imaged after irradiation induced elevation of PS exposure on vascular endothelium, and differences in spatial distribution and quantity of SPIO-PGN635 was analyzed. Histological analysis of Prussian staining and immunohistochemistry was finally applied to validate the vascular localization of SPIO-PGN635 in tumor tissues.

3.3 MATERIALS AND METHODS

3.3.1 Preparation of PGN635 F(ab')$_2$ fragments and labeling with SPIO nanoparticles

The human monoclonal antibody PGN635 was generated by Affitech A.S. (Oslo, Norway) in collaboration with Peregrine Pharmaceuticals. Inc. (Tustin, CA). It was produced under serum-free conditions by Avid Bioservices (Tustin, CA). Aurexis is a human monoclonal antibody that binds to an irrelevant antigen (*S. aureus* clumping factor A) and was used as a negative control antibody [138, 139]. PGN635 and Aurexis F(ab')$_2$ fragments were generated by reacting antibodies with pepsin at a molar ratio of 1:130 (antibody:pepsin) for 1 h at 37ºC. F(ab')$_2$ fragments (MW = 110 kD) were purified by FPLC using an *S-200 column (Pharmacia,* Piscataway, NJ) and PBS running buffer. F(ab')$_2$ fragments were then conjugated to polyethylene glycol (PEG) coated ultra small paramagnetic iron oxide (USPIO) nanoparticles with the iron oxide core diameter of 20 nm (SPP-20; Ocean Nanotech, AR). Briefly, carboxyl (-COOH) group on the distant terminus of the PEG chain of USPIO (1 mg) were activated with 1-Ethyl-3-[3-dimethylaminopropyl] carbodiimide hydrochloride (EDC) and N-hydroxysuccinimide (NHS) for 15 min, resulting in a semi-stable NHS or Sulfo-NHS ester, which were reacted with amino-group-containing antibody fragments

(1 mg) at room temperature for 2 hr with continuous mixing to yield amide bond. The conjugates were separated from unbound antibody fragments overnight at 4 ºC by using a DynaMag™ (Invitrogen, Grand Island, NY) magnetic separator. The products are referred to as SPIO-PGN635 or SPIO-Aurexis throughout the article. The iron concentration of IO-F(ab')$_2$ was determined by atomic absorption spectrometer (SpectrAA 50 spectrometer; air/acetylene flame; Varian Inc., Palo Alto, CA). The core size and hydrodynamic size of the nanoparticles before and after conjugation were measured by transmission electron microscope and dynamic light scattering using Zetasizer Nano ZS (Malvern Instruments, Worcestershire, UK).

The number of antibody fragments that were bound to each iron oxide nanoparticle was estimated by measuring the fluorescence intensity of near infrared dye labeled IO-F(ab')$_2$. F(ab')$_2$ was first labeled with IRDye-800CW (Li-COR, Lincoln, NE), as described in details previously [53]. The 800CW-F(ab')$_2$ was then conjugated with iron nanoparticles using aforementioned procedures. Optical light intensity of 800CW-F(ab')$_2$ or IO-F(ab')$_2$-800CW at various concentrations was obtained at the emission wavelength of 778 nm and used to determine the number of F(ab')$_2$.

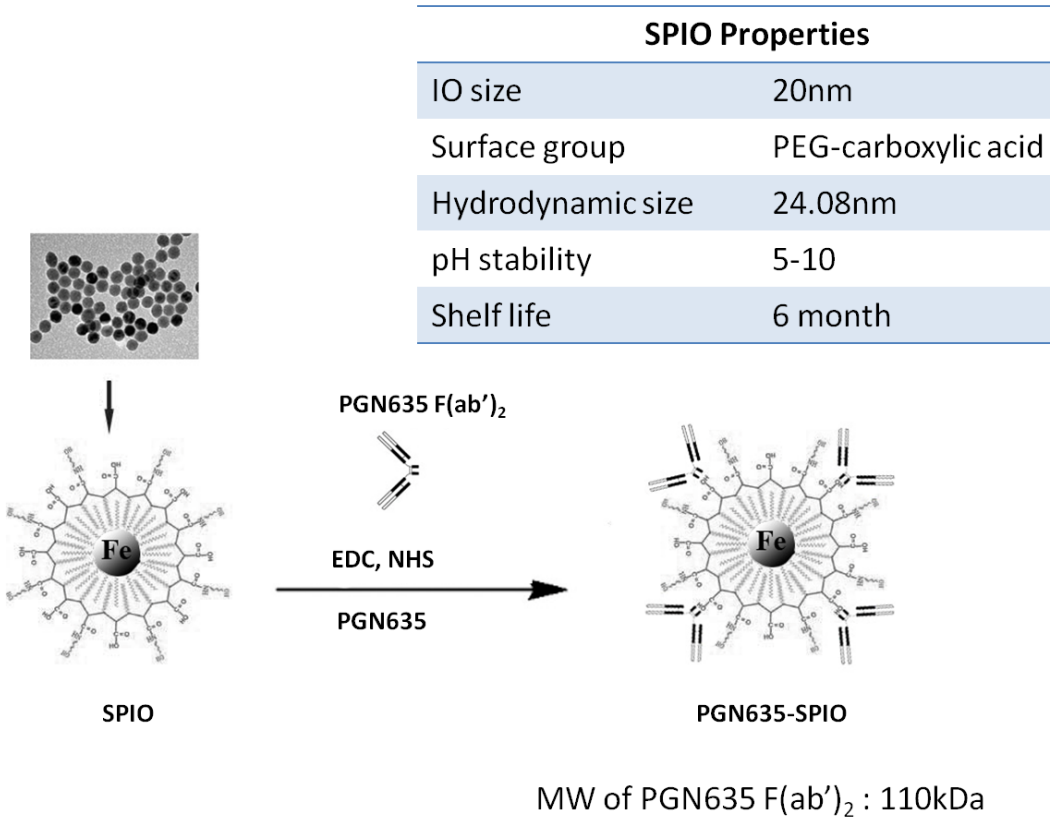

Figure 3-1 Diagram showing the steps of the conjugation process.
SPIO was functionalized by EDC and NHS and then linked to PGN635 F(ab')$_2$ fragments. The table in the top left corner shows the specifications of original SPIO.

3.3.2 In vitro binding specificity of SPIO-PGN635

Adult bovine aortic endothelial (ABAE) cells (Clonetics, Walkersville, MD) and 4T1 mouse breast carcinoma cells (American Type Cell Collection, Rockville, MD) were maintained in Dulbecco modified Eagle medium supplemented with 10% FBS 1% L-Glutamine and 1% penicillin-streptomycin.

To induce PS exposure, the cells were radiated with a single dose of 6 Gy X-radiation. Twenty-four hours later, the irradiated or non-irradiated cells were incubated with SPIO-PGN635 or the control SPIO-Aurexis at a concentration of 36 μg/ml iron for 1 hr. For the blocking study, the cells were pretreated with full length PGN635 (710 μg/ml) for 1 hr prior to SPIO-PGN635. Unbound particles were washed away with PBS, and then the cells were fixed with 4% paraformaldehyde (PFA). Prussian blue staining was performed to stain iron and the cells were then counterstained by nuclear fast red.

3.3.3 In vitro MRI of binding specificity of SPIO-PGN635

A subset of 4T1 cells used in prior *in vitro* study was subjected to *in vitro* MRI study. The cells that were irradiated or non-irradiated 24 hrs earlier were incubated with SPIO-PGN635 at different concentrations (18, 36 and 61μg/ml iron) or SPIO-Aurexis (36 μg/ml iron) for 1 hr. The same blocking study was performed here. After washing off all the unbound particles with PBS, 3×10^5 cells were mixed homogeneously with 0.8% agarose in 96-well-dish. The phantoms were imaged on a 9.4-T horizontal bore magnet with a Varian INOVA Unity system (Palo Alto, CA). A fast spin-echo multi-slice sequence (FSEMS; TR = 3000 ms, effective TE ranging from 40 to 120 ms with a 20 ms increment,

average = 2, number of slices = 10, acquisition time = 10 min) was used to acquire T_2-weighted images and obtain quantitative spin-spin relaxation time (T_2).

3.3.4 Tumor Model

All animal procedures were approved by the Institutional Animal Care and Use Committee of University of Texas Southwestern Medical Center. Two million 4T1 cells in 100 μl of serum-free medium containing 25% Matrigel (BD Biosciences, San Jose, CA) were injected subcutaneously on both thighs of anesthetized mice (n = 12; BALB/c nu/nu, 6-8 weeks old; NCI, Frederick, MD). Animals were sedated with 3% isoflurane and maintained under general anesthesia (2% isoflurane).

3.3.5 Radiation Treatment

When subcutaneous tumors on both thighs reached 6-8 mm in diameter, a single dose of 12 Gy of irradiation was delivered to the tumors on the left thigh using a small animal irradiator (XRAD320; Precision X-ray, Inc, North Branford, CT) fitted with a variable collimator to generate a single adjustable collimated iso-dose beam of x-rays at a dose rate of 10 Gy/min.

3.3.6 In vivo MRI of vascular targeting SPIO-PGN635 nanoprobes in 4T1 tumors

When the subcutaneous tumors reached 6-8 mm in diameter, *in vivo* MRI studies at 9.4T magnet were conducted 24 hours after radiation. Animals were sedated with 3% isoflurane and maintained under general anesthesia (1.5% isoflurane). Animal body temperature and respiration were monitored and maintained constant throughout the experiment. The same FSEMS sequence as used for *in vitro* study was applied for *in vivo* image acquisition. A series of FSEMS (number of slices = 10) images was acquired before and at different time points, typically 2, 4, 8, 24 and 48 hrs after *i.v.* injection of SPIO-PGN635 (n = 7) or SPIO-Aurexis (n = 5; 2.5mg iron/kg body weight in 100 μl volume) via a tail vein.

Analysis of MRI data was performed on a home written MATLAB program on both pixel-by-pixel and region of interest (ROI) basis. ROIs were drawn on both the tumors and adjacent thigh muscles on the high resolution T_2-weighted images. Signal intensity (SI) in these ROIs was measured for all the echoes of FSEMS images and a ratio of tumor to muscle (TMR) was obtained. To provide the spatial distribution of SPIO-PGN635 nanoprobes in tumors, 'hot-spot' maps showing the area with significantly low SI were created based on a pixel by

pixel analysis. Hot-spots were identified as voxels with SI values (based on effective TE = 80 ms) lower than 2 standard deviation of the baseline tumor parenchyma. Hot-spots were then overlaid on the corresponding high resolution T_2-weighted images. The total area of the hot-spots in individual MRI slices was summed and then divided by the whole tumor area to obtain the fraction of hot-spots.

3.3.7 Histological and immunohistochemical analysis

Immediately after MRI scan, tumor-bearing mice were sacrificed and tumor tissues were dissected out. The cryosections were immunostained with antibodies to the endothelial marker, CD31 (BD Biosciences, San Jose, CA) followed by horseradish peroxidase (HRP)-conjugated goat anti mouse secondary antibody (Serotec, Raleigh, NC). The same sections were then used for Prussian blue staining to detect SPIO-PGN635 nanoprobes and observe the localization of SPIO-PGN635 and their overlap with tumor vascular endothelial under microscope.

3.3.8 Statistical analysis

Statistical significance was assessed using an ANOVA on the basis of Fisher's protected least significant difference (PLSD; Statview; SAS Institute Inc., Cary, NC) or Student's t tests.

3.4 RESULTS

3.4.1 Characterization of SPIO-PGN635 nanoprobes

The average iron concentration of SPIO-PGN635 was 0.45 ± 0.03 mg/ml, determined by atomic absorption spectrometer. The average hydrodynamic size of SPIO before conjugation was 23.3 nm compared to 24.08 nm on the manufacture's manual (Figure 3-2). After conjugation the hydrodynamic sizes of SPIO-PGN635 became 24.7 nm. SPIO-PGN635 had a Zeta potential as -5.8 mV. Based on the measurement of fluorescent intensity produced from NIR-800CW dye conjugated to SPIO-PGN635, I estimated about 18 antibody fragments were attached to each nanoparticle via a covalent bound of amino group of antibody to the distant terminus of the polyethylene glycol (PEG) coated on the nanoparticle. No precipitation was visible in the solution of the conjugates for at least 2 weeks.

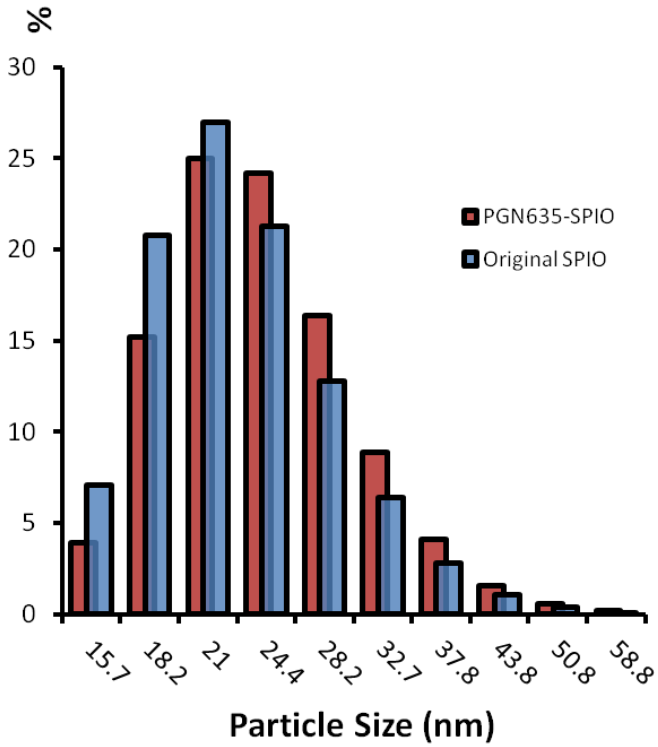

Figure 3-2 Histograms showing the hydrodynamic size of original and PGN635 conjugated SPIOs.

3.4.2 PS-targeting specificity of SPIO-PGN635 nanoprobes in vitro

Vascular endothelial ABAE cells and breast cancer 4T1 cells were irradiated 24 h earlier with a single dose of 6 Gy to induce exposure of PS on the outer membrane of the cells. For both cell types, specific binding of SPIO-PGN635 to PS was observed predominantly on the radiation-treated cells, evidenced by Prussian blue staining of iron (Figure 3-3B and E). Only minimal staining was seen on the non-irradiated cells (Figure 3-3A and F). The blue staining appeared to be surrounding the cells, implicating the SPIO-PGN635 is

indeed bound on the cell membrane. The specificity of SPIO-PGN635 was further confirmed by using control antibody conjugates, SPIO-Aurexis or pre-incubating with non-labeled PGN635 to block the binding of SPIO-PGN635, showing minimal bindings (Figure 3-3C and D).

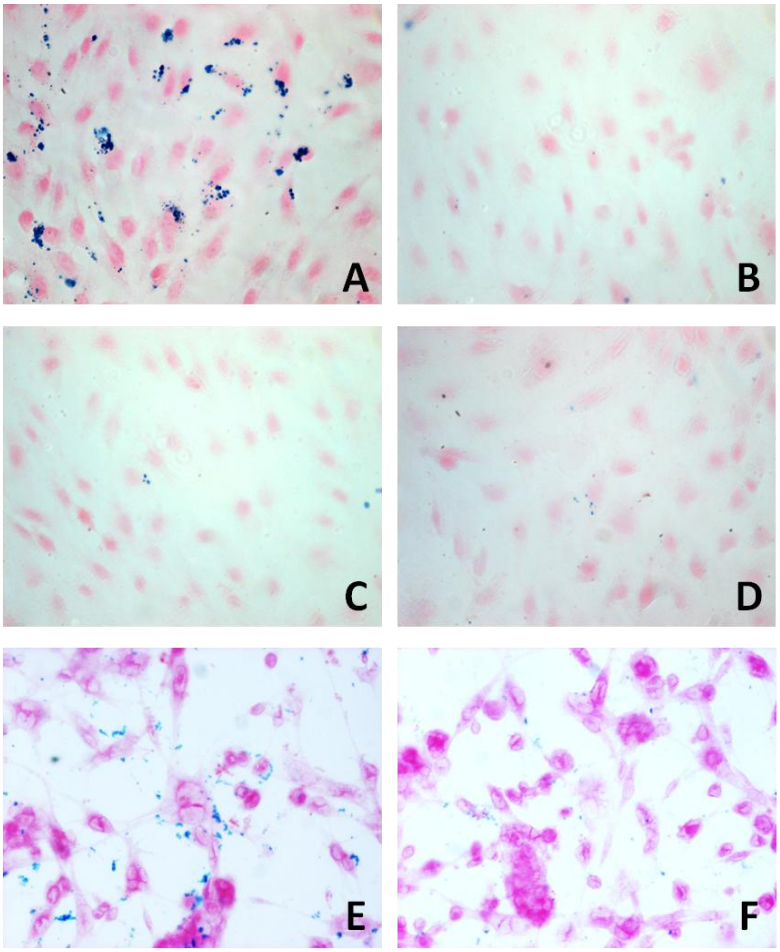

Figure 3-3 Prussian blue staining to determine SPIO-PGN635 bound specifically to exposed PS on the surface of vascular endothelia and tumor cells.
In vitro ABAE endothelial cells were either untreated (**A**) or pre-treated with 6 Gy radiation (**B-D**) 24 hr earlier. The cells were then incubated with SPIO-PGN635

(A and B) or the control antibody conjugates, SPIO-Aurexis (**C**), and the binding was detected by Prussian blue staining (counterstaining with nuclear fast red). Abundant blue iron staining was observed on the irradiated cells (**B**), but much less on the non-irradiated cells (**A**) or the irradiated cells incubated with SPIO-Aurexis (**C**). The specificity of SPIO-PGN635 was further confirmed by the competition study, showing significantly reduced binding after pre-treatment of the cells with PGN635. (**D**). Similarly, cell membrane localization of SPIO-PGN635 was detected on the irradiated 4T1 tumor cells (**E**), while a little blue staining was found on the non-irradiated 4T1 tumor cells (**F**).

3.4.3 In vitro MRI of PS-targeting specificity of SPIO-PGN635 nanoprobes

T_2-weighted fast spin echo MRI was used to evaluate agarose phantoms containing 4T1 cells that were pre-incubated with various SPIO conjugates. In good agreement with the *in vitro* histological data, marked reduction of SI was observed only in SPIO-PGN635-treated cells that were given 6 Gy irradiation previously (Figure 3-4A). A clear gradient of increased darkness accompanied with increased concentrations of the probes (Figure 3-4A bottom row). Minimal change of the signal observed for the SPIO-Aurexis-treated cells or the cells pre-incubated with non-labeled antibody again confirmed the specific binding of SPIO-PGN635 to exposed PS (Figure 3-4A top row). Significantly shortened T_2 values were observed in the irradiated cells treated with SPIO-PGN635, as compared to the control particles or PBS treated cells or the non-irradiated counterparts (Figure 3-4B and C; $p < 0.05$). A maximal reduction on T_2 was observed for the highest concentration of SPIO-PGN635 (Figure 3-4B and C).

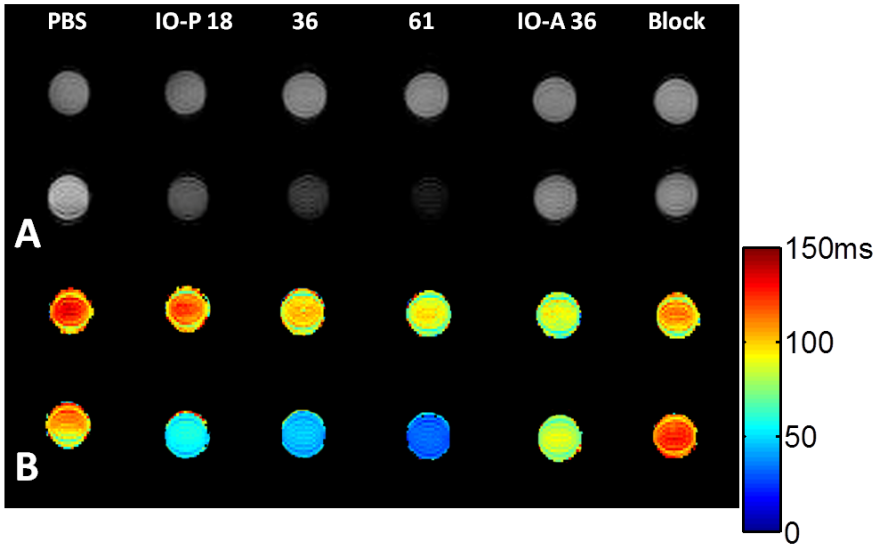

C

4T1 cells	T_2 values (ms)					
	PBS	IO-P (µg/ml)			IO-A 36	Block
		18	36	61		
Sham	128±10	121±10	112±7	106±7	104±7	116±9
IR	101±14	56±5*	45±4*	32±3*	83±7	120±9

Figure 3-4 MRI measurements of reduction of T_2-weighted signal intensity (SI) and T_2 values due to specific binding of SPIO-PGN635 to exposed PS on cultured 4T1 cells.

At 9.4T, MRI of homogeneous agarose phantoms containing 3 x 10^5 4T1 cells that were pre-incubated with either PBS, different concentrations of SPIO-PGN635 (IO-P, [Fe] at 18, 36 and 61 µg/ml) or the control antibody conjugates, SPIO-Aurexis (IO-A at 36 µg/ml). **A**. Minimal variations in SI were observed for the non-irradiated cells (top row). By contrast, the irradiated cells incubated with SPIO-PGN635 appeared darker (decreased SI) and maximal reduction of SI was observed at the highest iron concentration (61 µg/ml). Specific binding of SPIO-PGN635 to exposed PS was completely blocked by pre-treating the cells with unlabeled PGN635 antibodies. **B**. Corresponding maps of T_2 relaxation time showed significant reduction of T_2 values for the irradiated cells incubated with SPIO-PGN635. Absolute T_2 values were presented in **C** (* $p < 0.05$).

3.4.4 In vivo MRI detection of SPIO-PGN635 in 4T1 tumors

Longitudinal MRI was performed before and after i.v. injection of SPIO-PGN635 or SPIO-Aurexis. As shown in Figure 3-5, increased intratumoral hypointense regions, caused by specific binding of SPIO-PGN635 to exposed PS, were clearly visualized in both the non-irradiated and irradiated tumor as early as 2 h post SPIO-PGN635, as compared to pre-injection baseline images. Inhomogeneous distribution of the nanoprobes appeared throughout the tumors. As expected, irradiation significantly enhanced PS exposure, resulting in more SPIO-PGN635 binding than that of non-irradiated tumor. Follow-up MRI showed that the darkened regions in the irradiated tumor became more obvious at 8 h and persisted up to 48 h post injection. The time course of normalized TMR (tumor muscle ratio) of T_2-weighted signal intensity reached minimum at 2 hr for both the non-irradiated (22 ± 7%) and irradiated (34 ± 9%) tumor, which gradually recovered to the baseline level in the non-irradiated tumor, but stayed at low level in the irradiated tumor (Figure 3-5B). Histological analysis confirmed that blue stained SPIO-PGN635 co-localized with CD31-positive endothelial cells in non-irradiated tumor tissues (Figure 3-6 A). Consistent with imaging data, there were more SPIO-PGN635 nanoprobes binding to blood vessels of the irradiated tumors (Figure 3-6 C).

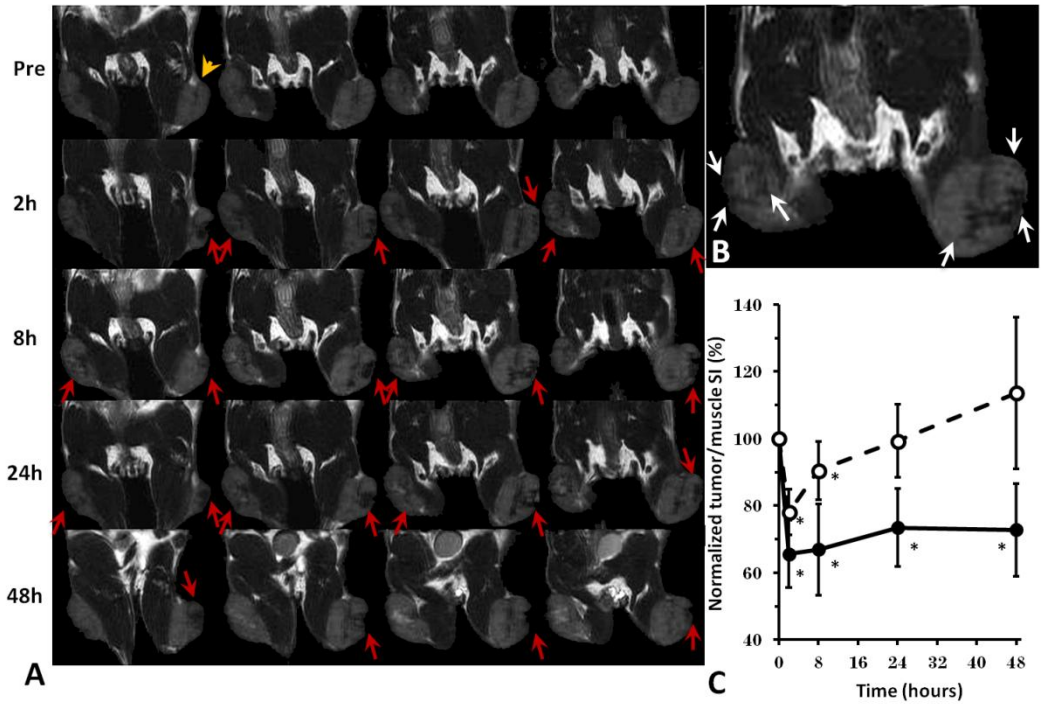

Figure 3-5 *In vivo* longitudinal MRI at 9.4T of exposed PS in 4T1 breast tumors following i.v injection of SPIO-PGN635.

A. A representative mouse bearing size-matched subcutaneous 4T1 tumors on each thigh received 12 Gy of irradiation to the left side tumor (arrowhead). 24 h after radiation, T_2-weighted FSEMS images (effective TE = 60 ms) were acquired at pre- and at different time points post injection of SPIO-PGN635 (2.5 mg Fe/kg) via a tail vein. From 2 h post injection, marked regional signal drops (arrows) were clearly observed intratumorally on four consecutive coronal sections (thickness = 1mm) of both side tumors, compared to the pre-injection baseline images. The irradiated tumor had more dark regions than the non-irradiated tumor, indicating more PS exposure induced by radiation. B) One representative section (the third section at 8 hour) with more magnification to show details of the SPIO-PGN635 uptake (white arrows). C) Plots of normalized T_2-weighted signal intensity (SI) change (TMR) showed a maximal mean decrease of 22 ± 7% and 34 ± 9% for the non-irradiated (open circle) and the irradiated (solid circle) tumor at 2 h, respectively. The signal decrease in the irradiated tumor persisted for at least 48 h after injection. However, SI of the non-irradiated tumor recovered gradually over time (* $p < 0.05$).

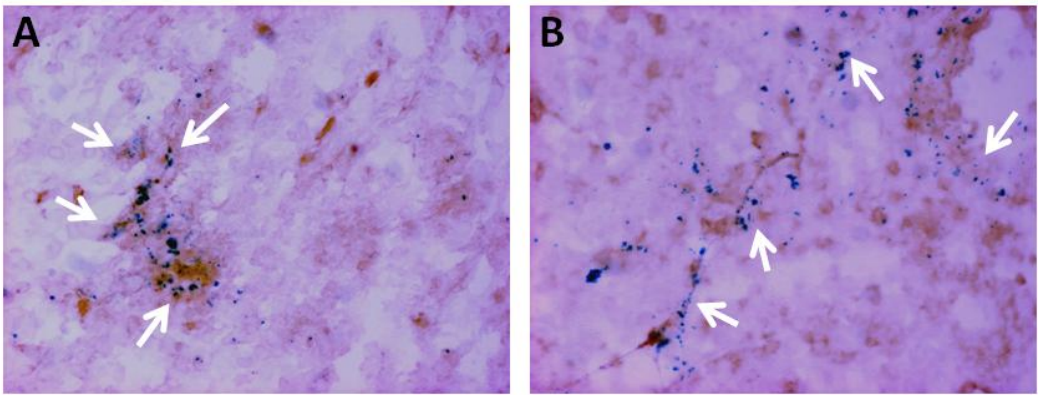

Figure 3-6 Co-staining with Prussian blue and CD31 (brown) shows radiation enhanced SPIO-PGN635 binding on both tumor vessels and tumor cells.
(A) Double staining of iron (Prussian blue; blue) and vascular endothelial cells (anti-CD31; brown) revealed coincidence of iron with tumor vessels (arrows) in the non-irradiated tumor. (B) Increased iron staining (arrows) was seen in the irradiated tumors and mainly located on the endothelial cells.

The antigen specificity of SPIO-PGN635 in subcutaneous tumors was evaluated by comparing the MRI pattern with the injection of negative control SPIO-Aurexis. No obvious particle disposition can be observed in either the irradiated or the sham-irradiated tumors. One representative animal can be seen in Figure 3-7. The mean signal loss of all slices after injection of SPIO-Aurexis reached the peak at 8.8% for the *non*-irradiated tumors, while for the irradiated tumors, mean signal intensity tumor to muscle ratio increased 5.5%.

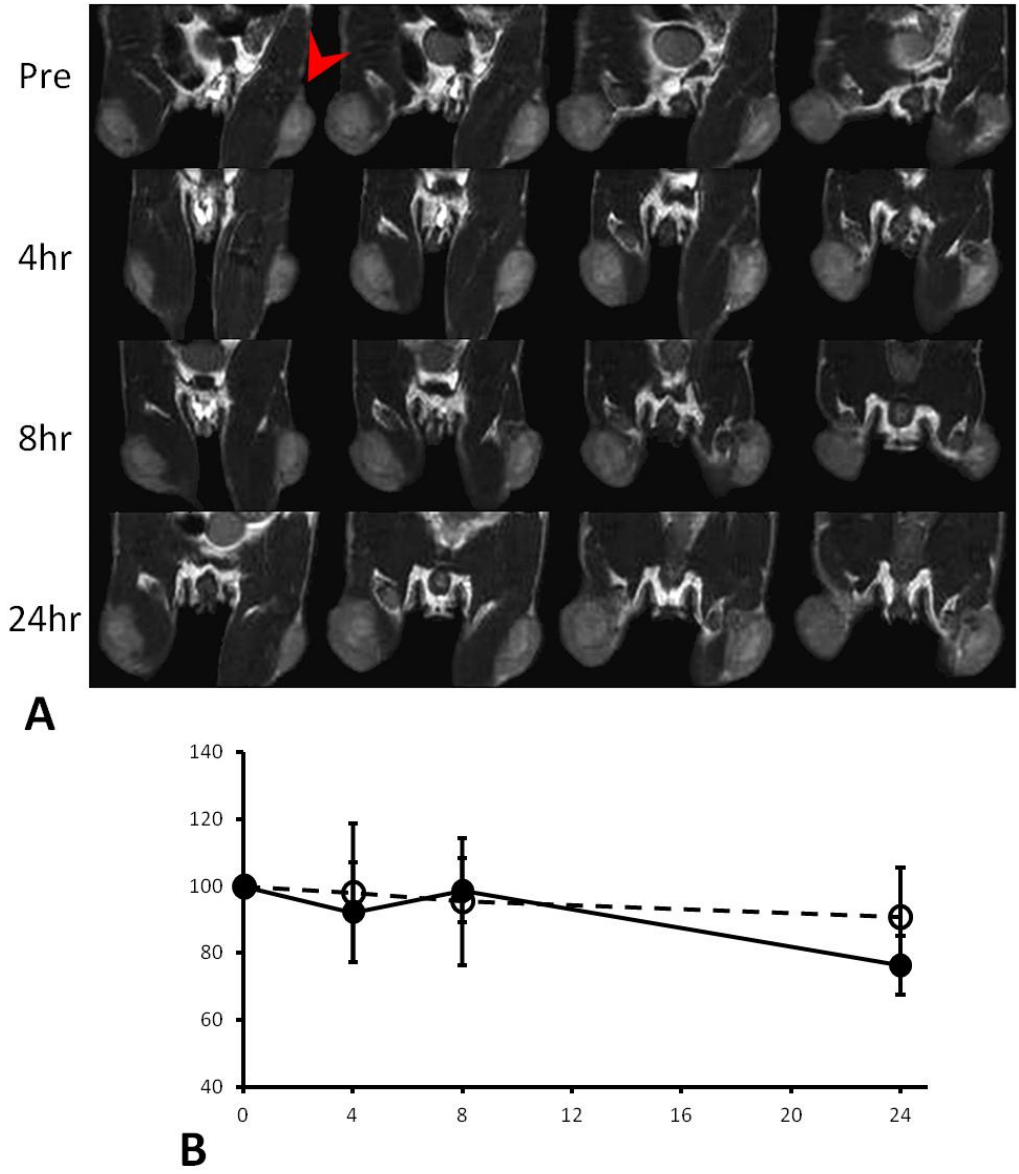

Figure 3-7 *In vivo* MRI of 4T1 subcutaneous tumors with an injection of 20nm SPIO-Aurexis.

A) Coronal sections showing four consecutive slices of a representative animal bearing 4T1 tumor implanted subcutaneously on both thighs. Tumor on the left side received 12 Gy radiation (red arrow head). No obvious signal loss can be seen after the administration of SPIO-Aurexis. B) Normalized T_2 signal intensity (SI) curves showing small changes in both the *non*-irradiated (empty) and irradiated (solid) tumor (8.8% and 5.5% respectively).

3.4.5 Spatial 'hot-spot' analysis of intratumoral distribution of SPIO-PGN635

To provide better understanding of the spatial distribution of SPIO-PGN635 in tumor, 'hot-spot' maps of the hypointense regions were created. Post SPIO-PGN635, increased numbers of hot-spots, typically seen as punctuate, were seen in both central and peripheral regions of non-irradiated tumor (Figure 3-8A), indicating baseline levels of PS exposure on tumor vascular endothelial. For the irradiated tumor, drastic increase in the number of hot-spots was observed after SPIO-PGN635. In addition to the punctuate pattern, most hot-spots in the irradiated tumor were clustered (Figure 3-8A). *In vivo* specific binding of SPIO-PGN635 was further confirmed by observing lack of change in SI or hot-spot after injection of the control antibody conjugate, SPIO-Aurexis. Dynamic change in fractions of hot-spots was plotted in Figure 3-8C. For the group of tumors receiving SPIO-PGN635 (n = 7), mean fractions of hot-spots increased significantly in both the irradiated and non-irradiated tumors, with the maximal increase of 5.0 ± 1.1% and 2.7 ± 0.4%, respectively ($p < 0.05$; Figure 3-9). No obvious change was observed for the IO-Aurexis $F(ab')_2$ group (n = 5).

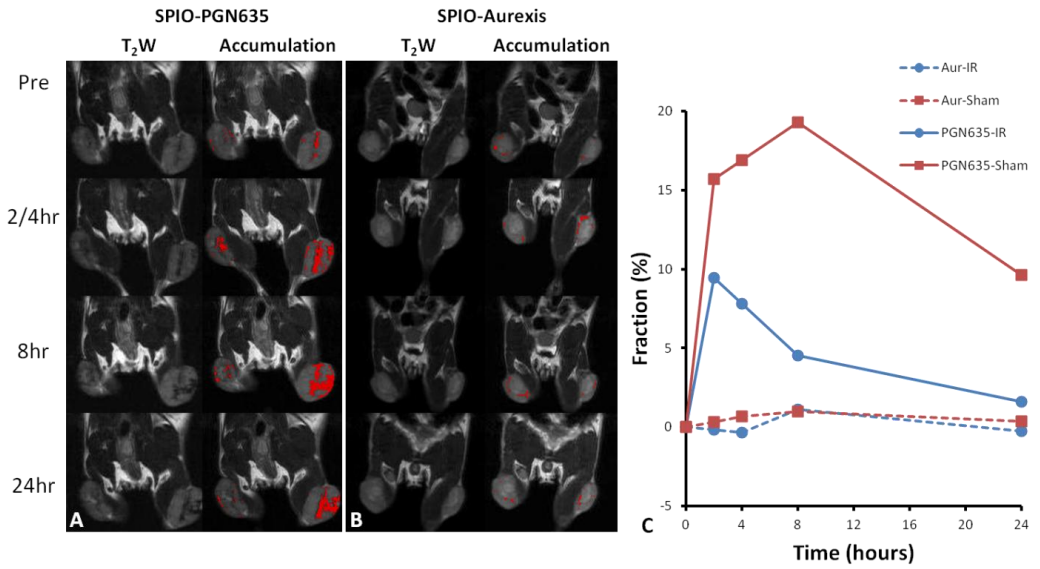

Figure 3-8 Quantitative 'hot spots' analysis of heterogeneous intratumoral distribution of SPIO-PGN635 in two representative cases.
Hot-spot maps were created by identifying hypointense regions in tumor on T_2-weighted images and then overlaying them on the corresponding T_2-weighted images. **A**. Baseline level of hot-spots prior to injection of SPIO-PGN635 is presented in a representative non-irradiated and irradiated tumor (arrowhead; the same animal as shown in Figure 3-5). Increased 'hot spots' were observed in both of the tumors after injection of SPIO-PGN635. Compared to the non-irradiated tumor, the irradiated tumor appeared to have more 'hot spots'. **B.** By contrast, there was essentially no change in 'hot spots' before and after injection of the control antibody conjugates, SPIO-Aurexis in either a non-irradiated or irradiated tumor (arrowhead). **C.** A fraction of 'hot spots' over the whole tumor was obtained for each tumor in **A** and **B**. Both the non-irradiated (solid line blue) and irradiated (solid line red) tumor showed marked increase in the fraction of hot spots after injection of SPIO-PGN635 with the maximal change of 9.5% and 19.3% achieved at 2 hr and 8 hr, respectively. However, there was minimal change for the SPIO-Aurexis-treated non-irradiated (dotted line blue) or irradiated (dotted line red) tumor.

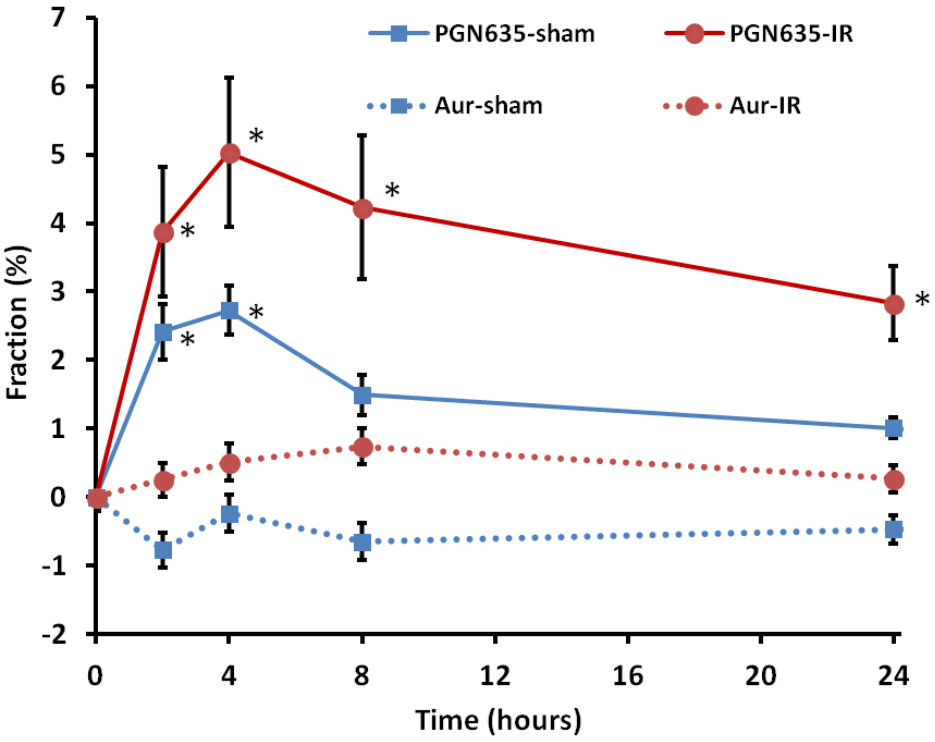

Figure 3-9 Changes in mean fractions of 'hot-spot' in tumors post injection of SPIO-PGN635 or SPIO-Aurexis.

After i.v injection of SPIO-PGN635, both the irradiated (n = 7, solid red) and non-irradiated (n = 7; solid blue) tumors showed a significant increase in the mean fraction of 'hot spots' (* $p < 0.05$). For the SPIO-Aurexis groups, no significant change was observed for either the irradiated (n = 5, dotted line red) or non-irradiated (n = 5, dotted line blue) tumors.

3.5 DISCUSSION

The present study demonstrated the feasibility of using PGN635F(ab')$_2$-conjugated, PEGylated SPIOs for in vivo MR imaging of tumor vasculature that contains PS exposed vascular endothelium in subcutaneous 4T1 breast tumors. *In vivo* MRI detected inhomogeneous signal loss in peripheral and central regions of the tumors, where SPIO-PGN635 bound to exposed PS on tumor vasculature. In contrast to the punctuate distribution pattern in non-irradiated tumors, clustered hypointense regions were seen after a single dose of 12 Gy radiation, indicating that irradiation induced elevation of PS exposure (Figure 3-8). The heterogeneous distribution of the nanoprobes detected by MRI accorded well with histological studies showing that SPIO-PGN635 localized solely on tumor vascular endothelia. In irradiated tumors, significantly increased levels of PS exposure were seen on tumor vessels. The antigen-binding specificity of SPIO-PGN635 was verified by competition experiments with unconjugated PGN635 (Figure 3-4) and by the lack of signal change with the irrelevant control SPIO-Aurexis (Figs. 2 and 4C).

The current MRI data are in accordance with the previous optical imaging of 800CW-PGN635F(ab')$_2$ in mouse glioma models. A clear tumor contrast in non-irradiated U87 gliomas was visualized as early as 4 h after injection of

800CW-PGN635F(ab')$_2$ by near infrared optical imaging. Irradiation enhanced the tumor contrast in both subcutaneous and orthotopic U87 gliomas [53]. However, the MRI data of the present study differed from the optical data in both signal distribution and magnitude change. Optical signals seemed homogeneous throughout the tumor, while only small fractions of tumor regions (2.7% for non-irradiated and 5% for irradiated tumors; Figure 3-5) were detected as hypointense by MRI. Moreover, optical imaging revealed a tumor/normal ratio of ~3 for non-irradiated tumors and 4 for irradiated tumors, while 22% and 34% MRI signal intensity change was observed for the non-irradiated and irradiated tumor, respectively, as shown in Figure 3-5 C. These variations actually provide a good example of how the two imaging modalities differ in terms of sensitivity and spatial resolution. Compared to optical and nuclear imaging methods, MRI is limited by its inherent low sensitivity. A tiny concentration of contrast agents, *e.g.*, at the nanomolar range, is insufficiently detectable by MRI, but can emit enough photons for optical imaging to capture. Thus, MR imaging of SPIO-PGN635 in this study may underestimate the tumor regions where PS is exposed on tumor vessels. However, the drawbacks of optical imaging such as light reflection, scattering and limited tissue penetration are attributed to its low spatial resolution. We also noticed the difference in the intratumoral distribution between SPIO-PGN635 and 800CW-PGN635F(ab')$_2$ in the irradiated tumors. In addition to tumor vascular localization, the optical 800CW-PGN635F(ab')$_2$ (dye : antibody

= 1:1) were also seen binding to tumor cells after irradiation induced PS exposure on them. By contrast, SPIO-PGN635, comprising the high molecular weight SPIO conjugated with multiple large antibody fragments (n = 18), were exclusively confined to tumor vessels (Figure 3-6 A), suggesting that preferential homing of the SPIO-PGN635 to vasculature was responsible for the MRI signal change. Lack of MRI signal change in the 4T1 tumors treated with the control antibody conjugates, SPIO-Aurexis also suggested a minimal EPR effect of the IO conjugates. Indeed, my data are in good agreement with previous reports by others. Kiessling et al. have recently shown in their $\alpha_v\beta_3$–targeted MR imaging studies that RGD-conjugated SPIO (10 nm in diameter) were observed predominantly on $\alpha_v\beta_3$-expressing tumor vasculature of several mouse tumor models [140]. However, Xie et al. found that RGD-conjugated ultrasmall SPIO (4.5 nm) dramatically increased cellular uptake by tumor cells [141]. Thus, increasing particle size, *i.e.*, encapsulating IO into micelles or liposomes, will probably enhance vascular localization if blood vessels are the desired targets.

Unlike the T_1 contrast agent, gadolinium, SPIO mainly generates negative contrast on T_2 or T_2^*-weighted images. Compared to paramagnetic T_1 contrast, SPIO has much higher molar relaxivity, thus, is widely used for molecular MRI. Signal loss due to SPIO shortening T_2 relaxation time, however, is often difficult to discriminate from background tissue with varying contrast, B_0 inhomogeneity or susceptibility artifacts. A simple analysis of T_2 signal loss, as shown in Figure

3-5, proved to be less informative about spatial distribution of the nanoprobes. Therefore, hot-spot analyses of the hypointense regions before and after injection of IO nanoprobes were applied to distinguish SPIO-induced signal voids from initial baseline level of dark signals, and obtain spatial distribution information.

Successful cancer imaging requires imaging probes that recognize cancer-specific markers with great specificity and sensitivity. Cell surface-exposed PS is an attractive target for molecular imaging. PS is strictly located in the inner leaflet of the plasma membrane bilayer in most normal cell types, including the vascular endothelium [40, 41]. Besides tumor vasculature, loss of PS asymmetry also occurs during apoptosis and necrosis [42, 43]. Much interest has been generated in developing molecular imaging probes that bind to the exposed PS in order to noninvasively monitor the response of patients' tumors to various treatments from the induction of tumor apoptosis [49, 52]. Annexin V (A5) is the PS binding ligand that is most widely used for this purpose. PGN635 and bavituximab, a chimeric monoclonal antibody that is currently evaluated in clinical trials [136, 137], have a more restricted specificity for PS than does A5, which recognizes PE in addition to PS and other anionic phospholipids [43].

In summary, I have evaluated a tumor vascular targeted imaging nanoprobe for molecular MRI. By conjugating PGN635F(ab')$_2$, a novel monoclonal PS targeting antibody, with MRI contrast PEG coated iron oxide nanoparticles, we detected heterogeneous intratumoral distribution of the nanoprobes by using in

vivo MRI, which coincided with tumor vascular endothelial cells. Irradiation increased the vascular PS exposure, correlating with significantly increased MRI contrast. The high specificity of PGN635 can serve as an alternative and unique vascular biomarker to facilitate molecular imaging and vascular targeting therapy.

Acknowledgments: Thanks to Dr. Rami R. Hallac for his help in MR experiment and data analysis, Dr. Jason H. Stafford and Dr. Philip E. Thorpe for providing antibody. Thanks to Dr. Yiguang Wang, Dr. Gang Huang and Dr. Shanrong Zhang for their help and valuable input in particle characterization, to Dr. Debabrata Saha for his help in using irradiator and immunocytochemistry techniques and Henry Dunn for his help in EM and other technical support. I am grateful to Dr. Jinming Gao and Dr. Ralph P. Mason for sharing the instruments and facility with me. We thank Peregrine Pharmaceuticals Inc., Tustin, CA, for the provision of PGN635 antibody. This work was supported in part by DOD W81XWH-12-1-0317 and by the Meredith D. Chesler Foundation, Dallas, TX. MRI experiments were performed in the Advanced Imaging Research Center, an NIH BTRP # P41-RR02584 facility.

CHAPTER FOUR
Dynamic Near-Infrared Optical Imaging of 2-Deoxyglucose Uptake by Intracranial Glioma of Athymic Mice

4.1 ABSTRACT

It is recognized that cancer cells exhibit highly elevated glucose metabolism compared to non-tumor cells. I have applied *in vivo* optical imaging to study dynamic uptake of a near-infrared dye-labeled glucose analogue, 2-deoxyglucose (2-DG) by orthotopic glioma in a mouse model.

The orthotopic glioma model was established by surgically implanting U87-luc glioma cells into the right caudal nuclear area of nude mice. Intracranial tumor growth was monitored longitudinally by bioluminescence imaging and MRI. When tumor size reached >4 mm diameter, dynamic fluorescence imaging was performed after an injection of the NIR labeled 2-DG, IRDye800CW 2-DG. Real-time whole body images acquired immediately after i.v. infusion clearly visualized the near-infrared dye circulating into various internal organs sequentially. Dynamic fluorescence imaging revealed significantly higher signal intensity in the tumor side of the brain than the contralateral normal brain 24 h after injection (tumor/normal ratio, TNR = 2.8±0.7). Even stronger contrast was achieved by removing the scalp (TNR = 3.7±1.1) and skull (TNR = 4.2±1.1) of

the mice. In contrast, a control dye, IRDye800CW carboxylate, showed little difference (1.1±0.2). *Ex vivo* fluorescence imaging performed on ultrathin cryosections (20 μm) of tumor bearing whole brain revealed distinct tumor margins. Microscopic imaging identified cytoplasmic locations of the 2-DG dye in tumor cells.

My results suggest that the near-infrared dye labeled 2-DG may serve as a useful fluorescence imaging probe to noninvasively assess intracranial tumor burden in preclinical animal models.

4.2 INTRODUCTION

Glioblastoma multiform (GBM) is a lethal intracranial cancer, which exhibits a relentless malignant progression and is highly resistant to conventional multimodal therapies. GBM is characterized by the nature of extensive infiltration into surrounding normal brain tissue, which results in incomplete tumor resection and consequent recurrence [142, 143]. It is imperative to improve diagnostic imaging to evaluate intracranial tumor growth and therapeutic responses. Optical imaging has been rapidly adapted to cancer research. Recently, optical imaging using fluorescent dye labeled tumor-specific molecules has been successfully applied to imaging glioma in preclinical animal models based on overexpression of such markers in glioma [144-146]. In the clinic, several recent studies have

demonstrated the ability of fluorescence imaging to facilitate radical resection of GBM during surgery [147-149]. Promising results reported by Stummer, *et al.* have shown that gross total resection of glioma guided by intraoperative fluorescence imaging is associated with improved prognosis of the patients with a median survival of 15–18 months, compared to 10–12 months after a subtotal resection or about 6 months after biopsy alone [149].

It is well recognized that cancer cells exhibit highly elevated glucose metabolism and up-regulated glucose transporters (GLUTs) compared to non-tumor cells. On this basis, ^{18}FDG, the glucose analogue, has been used as the most common PET radiotracer to visualize clinical tumors and their metastases. However, a drawback of ^{18}FDG PET for brain tumors is strong background signals of normal brain tissues, which often compromise the ability to diagnose the brain tumors. Moreover, PET has a low spatial resolution in spite of high sensitivity. Optical imaging by visualizing fluorescently labeled tumor cells has recently emerged as an attractive approach to facilitate identification of infiltrative tumors and sentinel lymph node metastases [150-155]. Alternative to radioactive deoxyglucose, fluorescent derivatives of 2-DG, *e.g.*, 2-[*N*-(7-nitrobenz-2-oxa-1,3-diazol-4-yl)amino]-2-deoxy-D-glucose(2-NBDG) have shown a great tendency to be delivered and trapped in tumor cells [156, 157]. However, the short wavelength of 2-NBDG (excitation, 475 nm; emission, 550 nm) limits its applications for *in vivo* imaging. Near infrared fluorescence has several

advantages over the use of visible fluorophores including deeper penetration due to less tissue absorption and scattering of light, and minimal autofluorescence. IRDye800CW 2-DG (Li-Cor Bioscience), a NIR dye conjugated with 2-deoxyglucose (peak excitation 785 nm, emission 810 nm), has recently been developed and demonstrated as a tumor-targeting optical contrast agent in various tumors implanted subcutaneously in mice, which can be visualized *in vivo* by fluorescence imaging [158, 159]. Moreover, a recent study of pharmacokinetics has shown that there is essentially no retention of the dye in normal mouse brain 24 h after injection [160]. Thus, the 2-DG NIR dye may serve as an ideal contrast agent for optically imaging brain tumors.

In this study, I used bioluminescence imaging (BLI) and MRI to assess non-invasively intracranial tumor growth in an orthotopic glioma model in nude mice. I then exploited IRDye800CW 2-DG for dynamic *in vivo* imaging of these brain tumors. *In vivo* observations were validated by both *ex vivo* fluorescence imaging of cryosections of tumor bearing brain tissues and histological staining. Finally, fluorescence microscopic studies were performed to identify locations of the 2-DG dye in tumors and normal brain.

4.3 MATERIALS AND METHODS

4.3.1 Orthotopic Glioma Xenografts

All animal procedures were approved by the Institutional Animal Care and Use Committee of University of Texas Southwestern Medical Center. Human glioma U87 MG cells (ATCC, Manassas, VA, USA) were infected with a lentivirus containing a firefly luciferase reporter, and highly expressing stable clones were isolated. A ~1 cm long incision of skin was made along the midline of the brain of an anesthetized nude mouse (BALB/c nu/nu; Harlan, Indianapolis, IN). Using a high-speed drill, a 1 mm burr hole of the skull was made in the right hemisphere, anterior to the coronal fissure. About 5×10^4 U87-luc cells in 3 µl mixture of PBS and Matrigel (25%, BD Biosciences, San Jose, CA) were injected directly into right caudal diencephalon, 1.5 mm beneath the dura mater using a 32G Hamilton syringe. Usage of a 32G fine needle minimizes tissue damage. The burr hole was filled with bone wax and the scalp was closed with sutures.

4.3.2 *In vivo* BLI

BLI was initiated for monitoring intracranial tumor growth about 10 days after tumor implantation and repeated once a week using the IVIS Spectrum

system (Caliper, Xenogen, Alameda, CA). The tumor bearing mice (n = 7) were anesthetized (isoflurane/O_2 in an induction chamber; isoflurane from Baxter International Inc., Deerfield, IL) and a solution of *D*-luciferin (120 mg/kg in PBS in a total volume of 80 µl; Biosynthesis, Naperville, IL) was administered s.c. in the neck region. Anesthesia was maintained with isoflurane (2%) in oxygen (1 dm^3/min). Five minutes after luciferin injection, an array of various exposure time (1, 5, 30, 60 s) was applied for image acquisition. Data were quantified with the Living Imaging software by using absolute photon counts (photons/s) in an ROI, manually drawn to outline the BLI signal of the brain.

4.3.3 *In vivo* MRI

Once a BLI signal was observed, MRI was performed to assess tumor volume and growth using a 4.7 T horizontal bore magnet with a Varian INOVA Unity system (Palo Alto, CA). Each mouse was maintained under general anesthesia (air and 2% isoflurane). A 27 G butterfly (Abbott Laboratories, Abbott Park, IL) was placed in a tail vein for contrast agent administration. Pertinent image slice positions were based on fast sagittal scout images. T_1-weighted (TR = 250 ms; TE = 20 ms; slice thickness = 1.5 mm; FOV = 25×25; in plane resolution 195 µm) and corresponding T_2-weighted (TR = 1900 ms; TE = 80 ms) spin-echo multislice coronal images were acquired. T_1-weighted contrast enhanced images

were acquired after i.v. bolus injection of the contrast agent Gd-DTPA-BMA (0.1 mmol/kg body weight; Omniscan^{TM}, Amersham Health Inc., Princeton, NJ) through the tail vein catheter. I determined tumor volume on T_2-weighted images by manually outlining the enhancing portion of the mass, excluding congested CSF signal in ventricles, on each image by using standard "browser" software provided with the Varian Inova imaging system. The area measurements were automatically calculated and multiplied by the MRI section thickness to calculate a per-section tumor volume. The total tumor volume was obtained by summing the volume calculations for all sections.

4.3.4 Near Infrared Fluorescence Imaging

4.3.4.1 *In vivo* real-time imaging of first pass perfusion.

When the intracranial tumors grew to larger than 4 mm in diameter based on T_2-weighted MRI, *in vivo* fluorescence imaging was performed using a Maestro imaging system (CRI Inc. Woburn, MA). Each mouse was anesthetized by i.p. injection of a ketamine/xylazine cocktail (40 µl). A 27 G butterfly (Abbott Laboratories) was placed in a tail vein for administration of the 2-DG dye, IRDye800CW 2-DG (15 nmol/mouse in 150 µl saline, Li-Cor Biosciences, Lincoln, NB) or a control dye, IRDye800CW carboxylate (15 nmol/mouse in 150

µl saline, Li-Cor Biosciences). Based on the methodology developed by Hillman and Moore [161], an excitation filter (671–705 nm) was applied. A series of whole body images was acquired before and after a bolus injection of the 2-DG dye or the control dye. Typically, 5 frames/s for the first 20 s, 2 frames/s for the next 30 s and 1 frame/s for the rest of ~2 min were acquired. Image processing and data analysis were performed using the DyCE software provided with the Maestro software 2.8.

4.3.4.2 *In vivo* dynamic imaging of 2-DG uptake by intracranial tumors.

The brain-focused fluorescence images were acquired before and 10 min, 30 min, 2 h, 4 h, and 24 h after injection of the 2-DG or the control dye. A set of filters specifically for NIR imaging (excitation, 671–705 nm; emission, 730–950 nm) was applied. At each time point, the mouse was anesthetized by i.p. injection of the ketamine/xylazine cocktail (40 µl). Immediately after the last image at 24 h, the scalp of the mouse was surgically reflected to expose the skull and a fluorescence image was acquired. Before sacrificing the mouse, the skull was removed to expose both sides of the brain tissues and a last *in vivo* image was obtained. The whole surgical procedure and imaging was completed within 15 min on the anesthetized animals and no obvious bleeding was observed.

4.3.4.3 *Ex vivo* fluorescence imaging on cryosections of tumor bearing brain.

Immediately after sacrificing the animals, the whole brains were dissected and embedded in O.C.T. and then transferred to −80°C freezer. On the second day, a series of coronal sections (20 µm) of the brain was cut. The frozen sections containing tumor tissues were identified by cresyl violet staining. The adjacent tissue sections were used for *ex vivo* fluorescence imaging and fluorescence microscopic study, as described in detail below. The *ex vivo* images were taken by using the same Maestro system as used for *in vivo* studies. Typically, an exposure time of 2.5 s was applied for image acquisition.

4.3.4.4 Analysis of Fluorescence Imaging

Fluorescence images were obtained using the Maestro system and processed with the Maestro software 2.8. The spectrum of background signal (peak emission ~770 nm) was first obtained from a mouse before the IRDye 800cw dye injection, while the spectrum of IRDye 800cw dye (peak emission ~810 nm) was detected from a solution of the dye in PBS (0.1 nmol/µl). The spectra were then imported and used to unmix the NIR dye signal from the background signal for both *in vivo* and *ex vivo* studies. The whole set of *in vivo* images of an individual mouse, obtained before and at various times after injection of the dye, was examined for quantification. A common ROI was based on the most obvious signal of the

tumor, which was observed on the image of the skull-deprived mouse 24 h after injection in each of the 2-DG animals, was applied on both the tumor side and the contralateral normal brain of each image. A total of photon counts (counts/s) in the identical ROI was used for comparison of dynamic change in signal intensity.

4.3.5 Histology and Fluorescence Microscope

Cresyl violet staining was performed on the cryosections (20 μm). Tumor margins were determined under microscope and correlated with the NIR light signal acquired by *ex vivo*fluorescence imaging. The cryosections, unstained or counterstained by 4′,6-diamidino-2- phenylindole (DAPI), were used for fluorescence microscopy study. The NIR fluorescence signal was detected using a Zeiss AxioObserver (Carl Zeiss MicroImaging, Inc., Thornwood, NY) equipped with NIR filters. The NIR signals were recorded and overlaid on either a dark image or an image counterstained by DAPI of the same field. For luciferase staining, monoclonal mouse antiluciferase mAb (1:150; AbD Serotec, Raleigh, NC) and cy3-conjugated goat anti-mouse secondary antibody (Jackson Immunoresearch Laboratories, West Grove, PA) were used.

4.3.6 Statistical Analysis

Statistical significance was assessed using an ANOVA on the basis of Fisher's protected least significant difference (PLSD; Statview; SAS Institute Inc., Cary, NC) or Student's t tests.

4.4 RESULTS

Immunohistochemical study showed extensive expression of luciferase in the U87-luc cells of intracranial tumor tissues (Figure 4-1 A). Longitudinal BLI studies revealed a weak signal initially 11 days after tumor implantation, which became stronger on follow-up to day 24 (Figure 4-1 B). The mean light intensity detected on day 24 for the group of tumor bearing mice was significantly greater than on day 11 (1.6×10^8 versus 1.1×10^7 photons/s; $p<0.05$). MRI studies based on T_2-weighted and T_1-weighted contrast enhanced images confirmed an intracranial tumor located in the right side of the brain of each animal (Figure 4-1 C). A significant correlation was found between BLI signal and actual tumor volume measured by MRI ($r = 0.8$, $p<0.05$; Figure 4-1 D). Tumor volume determined on the last MRI scan (one day before the *in vivo* fluorescence imaging) varied from 42 to 136 mm^3 in the seven animals. There was no significant difference in tumor

volume between the group receiving the 2-DG dye or the control dye when the *in vivo* fluorescence imaging was performed ($p = 0.5$).

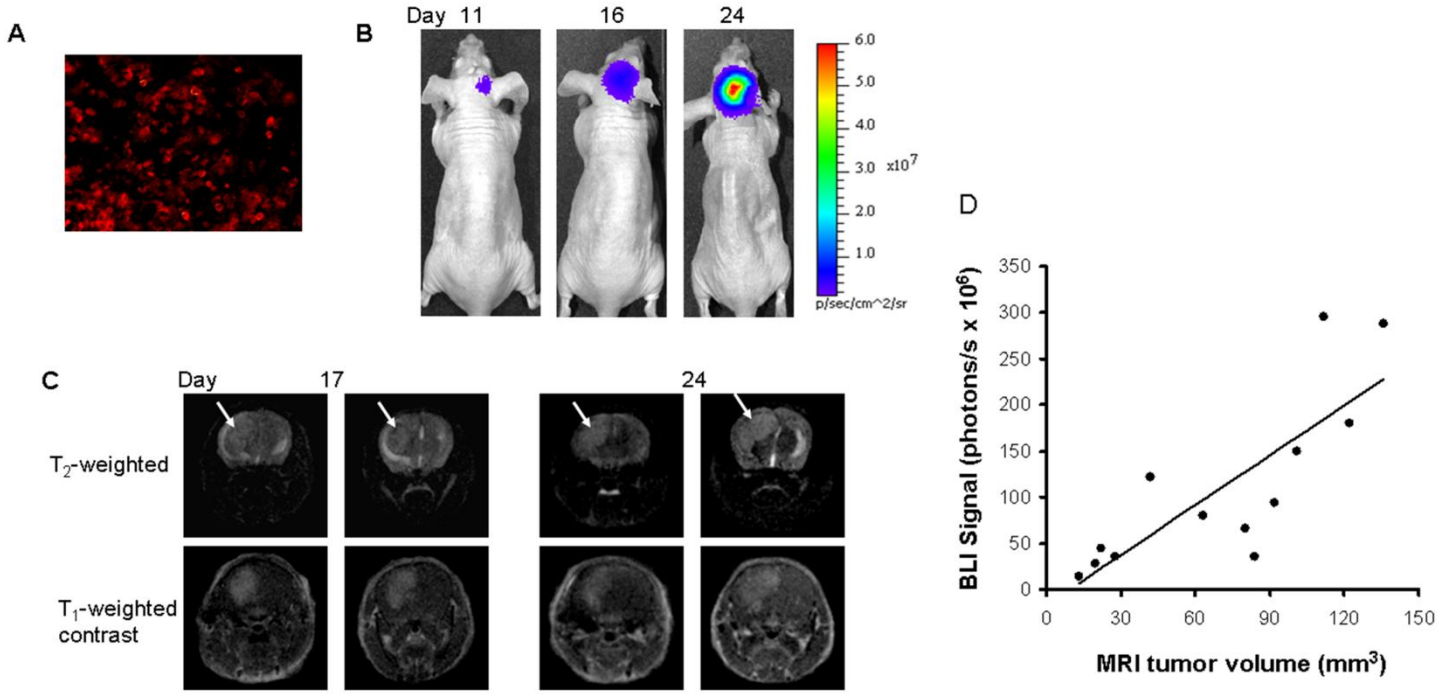

Figure 4-1 BLI and MRI monitoring of intracranial growth of U87 glioma in a mouse.
(A) Immunostaining with anti-luciferase antibody showed extensive expression of luciferase in tumor tissues. **(B)** BLI showed increasing light intensity in the mouse brain over time. **(C)** Transaxial MRI detected an intracranial tumor on consecutive slices (arrows) based on both T_2- weighted and T_1-weighted contrast enhanced MRI, which was found to grow in size on the follow-up study (84 mm^3 on day 17, 136 mm^3 on day 24). **(D)** A good correlation between the BLI signal and actual intracranial tumor volume was observed ($r = 0.8$, $p<0.05$).

The real-time whole body NIR optical imaging, acquired immediately after i.v. injection of the 2-DG dye, IRDye 800CW 2-DG (15 nmol/mouse) or the control dye, IRDye 800CW carboxylate (15 nmol/mouse), visualized the first pass of the dye sequentially through various organs and tissues (Figure 4-2). By narrowing the field of view (FOV), brain-focused *in vivo* imaging showed dynamic changes in fluorescence signal intensity on the tumor side of the brain (right) in comparison with the contralateral normal brain (left). Relatively higher signal intensity was observed for the 2-DG dye in both sides of the brain than the rest of the mouse body (Figure 4-3). Time course curves showed that the signal intensity in both sides of the brain had a maximum value of $1.2\times10^{7}\pm0.2\times10^{7}$ counts/s 10 min after injection, and gradually washed out over 4 h. There was no significant difference in signal intensity between the two sides of the brain during the first 4 h after injection (Figures 4-3A and 4; $p>0.3$). Twenty four hours later, a dramatic drop in signal intensity was observed. However, significantly higher light signal was clearly seen in the tumor side of the brain than the contralateral normal side ($1.8\times10^{5}\pm0.2\times10^{5}$ versus $0.7\times10^{5}\pm0.4\times10^{5}$; $p<0.05$; Figure 4-4 A). A mean tumor/normal ratio (TNR) for the group of 4 tumors was 2.8±0.7 (Figure 4-4 B). In contrast, the control dye showed little difference ($0.54\times10^{5}\pm0.1\times10^{4}$versus $0.43\times10^{5}\pm0.3\times10^{4}$; TNR = 1.1±0.3; Figure 4-4 B and C). To confirm that the signal originated from the brain tumor, I

performed surgical procedures to reflect scalp and further remove skull to expose the brain. A brighter and more focused light signal emitted from the region of the tumor implantation was seen (Figure 4-3 A). Stronger contrast was achieved by reflecting the scalp (TNR = 3.7±1.1) and further removal of the skull of the mouse revealed a highest TNR of 4.2±1.1 (Figure 4-4 C). For the control dye, similar to the observation in the intact animals, no significant difference was found (TNR = 1.4±0.2 and 1.4±0.1, respectively; Figure 4-4 C). Comparison of *in vivo* BLI and 2-DG fluorescence imaging of intracranial tumors also showed a strong linear correlation albeit in a small number of animals (n = 4; r = 0.9; Figure 4-4 D). After sacrificing the mice, the whole brain was dissected and ultrathin sections (20 μm) of tumor bearing brain were imaged using the same fluorescence imaging system as used for *in vivo*. Most intriguingly, distinct tumor margins, even the tracks of migration of small number of tumor cells, were identified based on the fluorescence images, which correlated well with histological staining of the tumor (Figure 4-5). In good agreement with *in vivo* imaging data, uptake of the 2-DG dye was found to be significantly higher in tumor than the contralateral normal brain (TNR = 3.7±1.1; $p<0.01$; Figure 4-5 I). Finally, fluorescence microscopy showed more uptake of the 2-DG dye in tumor regions, compared to the control dye (Figure 4-6). Co-registration of the NIR signal with the DAPI stained nuclei showed a cytoplasmic localization of the 2-DG dye (Figure 4-6 G).

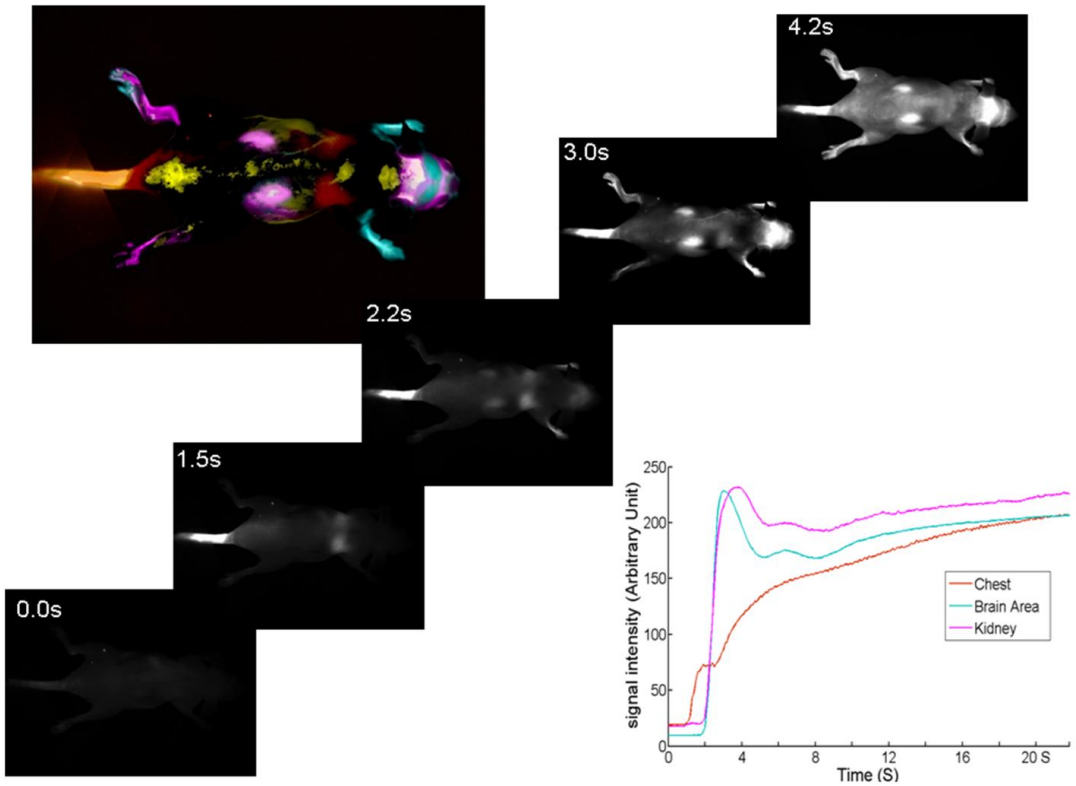

Figure 4-2 *In vivo* real-time near infrared imaging of a mouse.
A series of whole body images was acquired before and after injection of near infrared dye labeled 2-DG, IRDye800CW 2-DG, via a mouse tail vein. Selected images captured the first pass perfusion of the dye into various internal organs: heart and lung area at 1.2 s, brain and upper limbs at 2.5 s, kidney at 4.5 s, etc. Principal Component Analysis of the kinetics was used to identify tissue regions based on DyCE software as shown in the color presentation (top left) and representative time courses (bottom right).

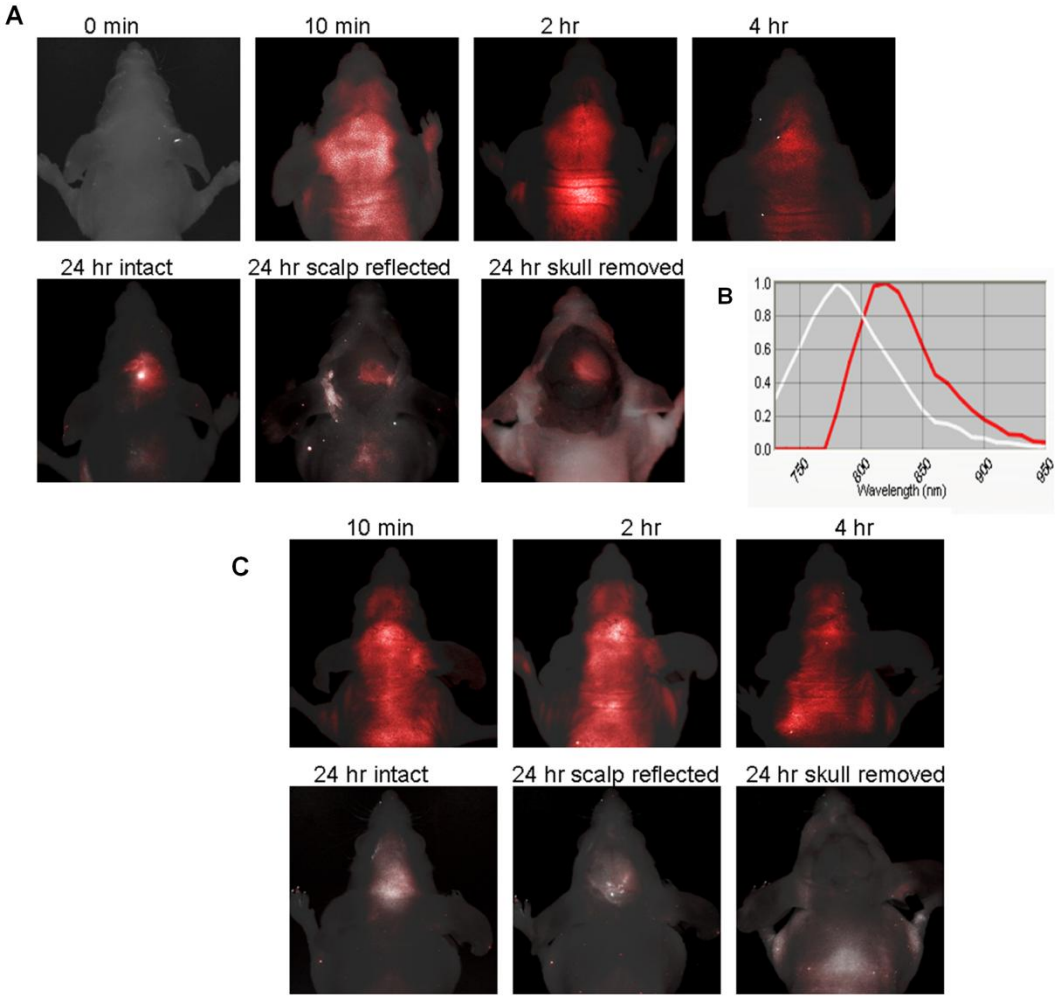

Figure 4-3 Dynamic *in vivo* fluorescence imaging of the 2-DG dye uptake by intracranial glioma.

(A) After i.v. injection of IRDye800CW 2-DG repeated *in vivo* fluorescence imaging was performed. During the first four hours, unmixed images showing stronger signal of the dye in the brain area, but there was no obvious contrast between the tumor side of the brain and the normal brain. However, 24 h later, the light signal remained only in the tumor side of the intact brain. Even better contrast was seen after reflection of the scalp or further removal of the skull. **(B)** Normalized emission spectra showing the near infrared 2-DG dye with a peak emission wavelength at 810 nm (red), while the background signal (white) was at ~770 nm. **(C)** As a control of the 2-DG dye, IRDye800CW carboxyl was injected into a mouse bearing orthotopic glioma. No significant difference in light intensity between the two sides of the brain was observed at any time points.

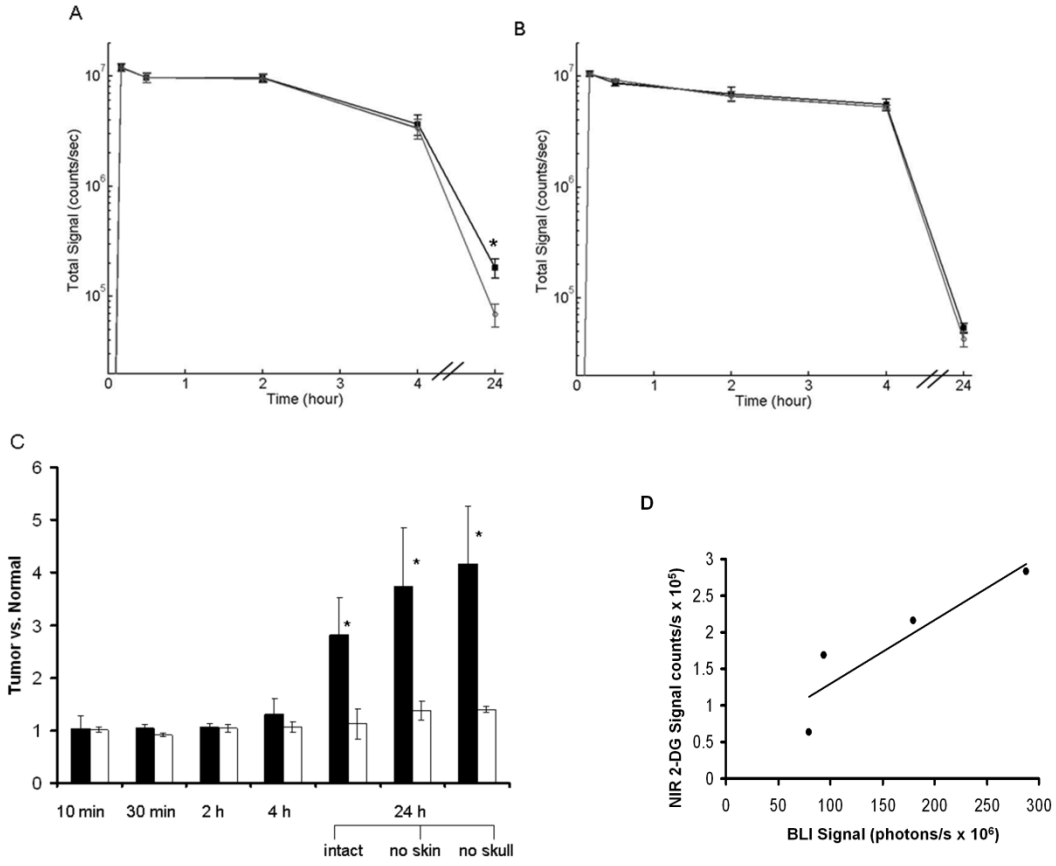

Figure 4-4 Time course of light intensity of *in vivo* fluorescence imaging of the 2-DG dye.

Mean light intensity curves shown for the tumor side (solid square) and the contralateral normal brain (open circle) of intact mice. **(A)** For the 2-DG dye (n = 4), the curves were essentially identical for the first 4 h post injection, but after 24 h, there was a significant difference ($1.8\times10^5\pm0.2\times10^5$ versus $0.7\times10^5\pm0.4\times10^5$; $p<0.05$). **(B)** In contrast, the control carboxylated dye showed no difference during the whole course (n = 3). **(C)** Time course of tumor to normal tissue ratio (TNR) showing a significantly higher TNR in the 2-DG dye group (mean = 2.8±0.7; solid bar) versus the control group of the control dye (n = 3; 1.1±0.3; open bar) 24 h after injection ($p<0.05$). An even bigger TNR was obtained in the 2-DG group by removing the scalp (3.7±1.1) or skull (4.1±1.1). **(D)** A strong linear correlation was observed between light intensity of *in vivo* BLI and 2-DG NIR imaging of intracranial tumors (r = 0.9).

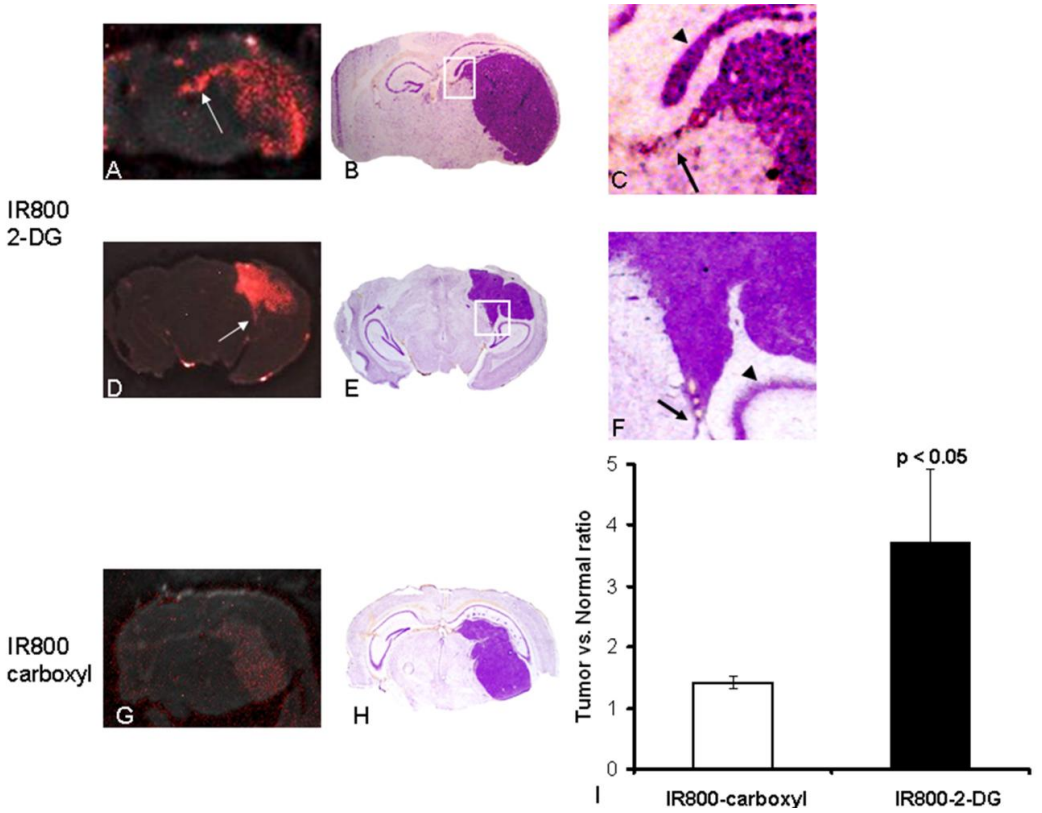

Figure 4-5 *Ex vivo* near infrared fluorescence imaging of ultrathin cryosections of tumor bearing brain tissues.

Unstained coronal brain sections (20 µm) containing tumor tissues were obtained immediately after the 24 h *in vivo* image for *ex vivo* imaging. For the tumors with 2-DG dye, representative images for a larger (A) and a small (D) intracranial tumor showed predominant accumulation of the dye within the tumor mass. Tumor mass was clearly delineated from the surrounding normal tissues. Even a track of migrated tumor cells was depicted in each case (arrows in A and D), which correlated well with cresyl violet staining of the corresponding regions enlarged from B and E (arrows in C and F). Arrow heads refer to the dentate gyrus. The control dye showed no significant difference between the tumor regions and the normal brain (G and H). Tumor/normal ratio (TNR) of the 2-DG dye was significantly higher than that of the control dye (3.7±1.2 vs. 1.4±0.1; $p<0.05$; I).

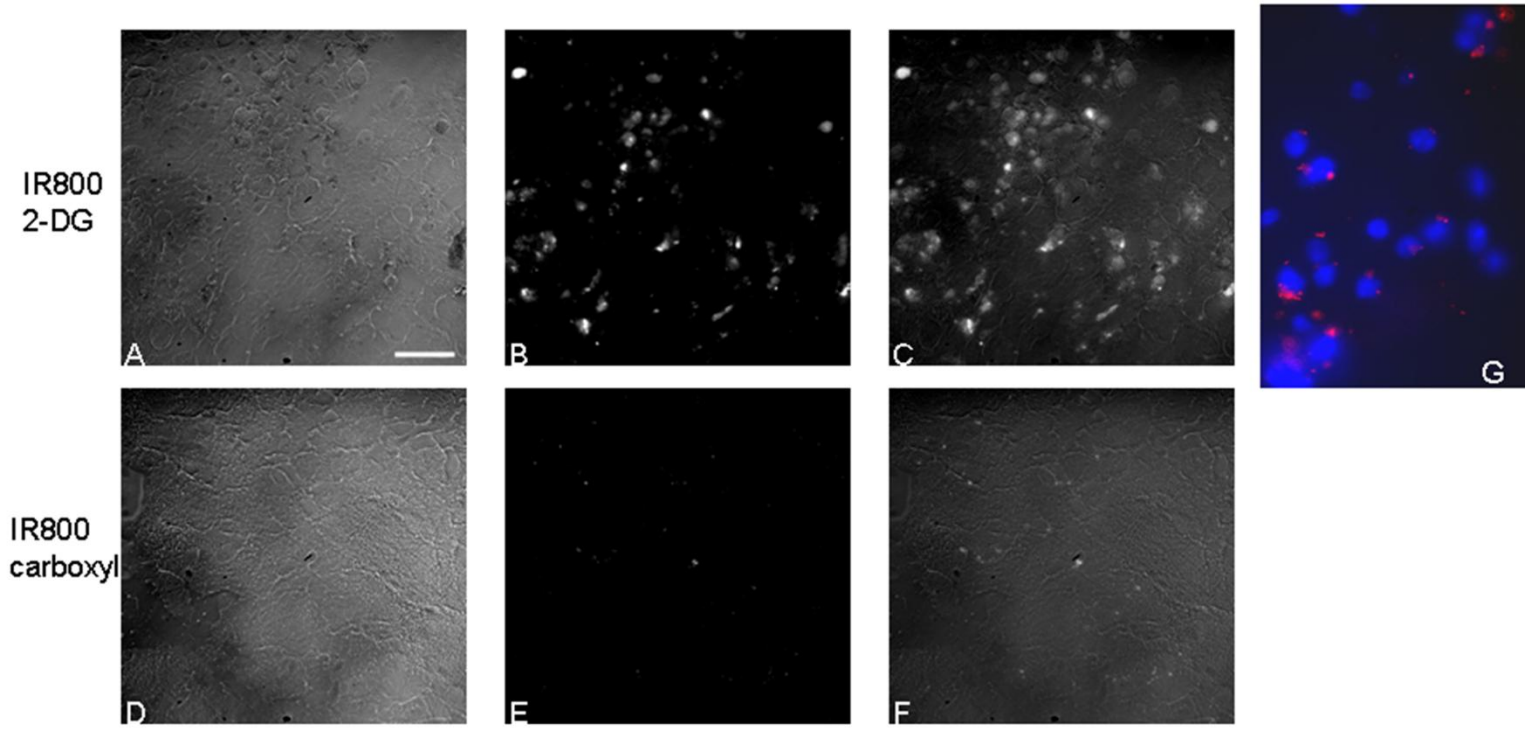

Figure 4-6 Microscopic fluorescence imaging determined localization of the 2-DG dye.
The unstained frozen sections of tumor bearing brain tissues, also used in Figure 4-5 , were scanned under dark field (A and D). Near infrared signals (B and E) of the same fields detected with an infrared filter were overlaid on the dark field images (C and F). Significantly higher signal was seen in tumor tissues of the mouse injected with the 2-DG dye, compared to the one with control dye. Co-staining of nuclei of tumor cells with DAPI indicated cytoplasmic localization of the 2-DG dye (red; G).

4.5 DISCUSSION

I have demonstrated the feasibility of using the NIR dye labeled 2-deoxyglucose, IRDye800CW 2-DG, for *in vivo* fluorescence imaging of orthotopic glioma in a mouse model (Figure 4-3). *Ex vivo* fluorescence imaging of tumor sections and microscopic imaging confirmed significantly higher accumulation of the 2-DG dye in intracranial tumors than in normal brain. Good correlations were found between each imaging modality in terms of *in vivo* evaluation of intracranial tumor burden (Figures 4-1 and 4D).

Small animal imaging has been increasingly adapted for preclinical cancer research. *In vivo* imaging promises greater efficiency since each animal serves as its own control and multiple time points can be examined sequentially. In particular, multimodal imaging approaches provide comprehensive information about both tumor anatomy and pathophysiology and even molecular mechanisms [145, 162-165]. In this study, I combined optical imaging (bioluminescence and fluorescence imaging) with MRI to study longitudinal development of intracranial tumors and their uptake of a glucose analogue, 2-DG. There was good agreement between increased BLI signal intensity over time and enlarged tumor volume measured by MRI, as also reported by others previously for intracranial tumors in rodent models [65, 145]. Thus, the cheap, fast and high-throughput BLI seems to

be just as effective in monitoring the deep-seated orthotopic tumor models as the expensive and time consuming MRI. However, BLI does not provide anatomic details due to the poorer spatial resolution and limited depth of light penetration. Recent progress in BLI tomography should facilitate three-dimensional analysis. In addition to providing detailed anatomic structure, MRI is also useful to obtain pathophysiological information, *i.e.*, tumor vascular perfusion and permeability, oxygenation, and apoptosis or necrosis, though not reported here.

Fluorescence imaging can be used to evaluate small reporter molecule pharmacokinetics, avoiding the need for genetic modification of cells. In particular, near infrared fluorescence (NIR) imaging has found a greater potential for clinical application because of its long wavelength (650–900 nm), where light absorbance and scattering are significantly lower, and autofluorescence of normal tissues is also greatly reduced [166]. In view of this approach, various target-specific NIR conjugates have been reported for targeting tumor imaging, *e.g.*, tumor integrin, $\alpha_v\beta_3$ [145], tumor growth factors or their receptors [159, 167-171], glycoprotein [172], or tumor specific protease [163]. Successful applications in various preclinical tumor models have been reported, though most of these studies were performed on surface tumors. *In vivo* NIR imaging of deep-seated orthotopic tumor models, in particular, intracranial tumors, remains challenging. By targeting the overexpressed $\alpha_v\beta_3$ in tumor, Hsu, *et al.* recently reported visualization of orthotopic glioma of mouse *in vivo* by NIR imaging via Cy5.5-

RGD. Peak of tumor uptake was found 2 h post injection and TNR = 2.6 was achieved with a craniotomy [145]. More recent work with an orthotopic mouse brain tumor McCann, *et al.* successfully applied fluorescent molecular tomographic imaging to monitor protease activity in tumor by using protease activatable fluorescence, ProSense680 (peak light emission at 680 nm). By co-registering fluorescence images with MRI, localization of the active protease in tumor was determined [146].

Here, I applied the commercially available NIR labeled 2-deoxyglucose to imaging intracranial tumors based on the simple mechanism of differential levels of glucose metabolism between tumors and normal tissues. Tumor cells both require more energy for their higher proliferation rate and utilize the inefficient glycolytic pathway to produce energy. Thus, tumor cells need more glucose compared to normal cells. On this basis, ^{18}FDG has been used as the most common PET radiotracer to visualize clinical tumors and their metastases. However, ^{18}FDG PET imaging of brain tumor is often compromised by strong background signals of normal brain tissues. Due to the short half life of fluorine-18 (<2 h), PET imaging is normally performed within 1 h after injection of ^{18}FDG. The lower contrast between tumor and normal brain may be partly attributed to this timing, at which a maximum ratio of uptake is not reached. Indeed, I found no significant difference in light signal in the tumor side of the brain versus the normal side of the brain during the first 4 hours post injection.

The peak tumor to normal ratio was actually observed at 24 h, which is consistent with a previous study of subcutaneous U87 tumors using cy5.5 labeled D-glucosamine. However, a control dye, cy5.5-NHS used in that study also produced a high TNR [156]. The study is also in a good agreement with another study that detected essentially no retention of IRDye800CW 2-DG in normal brain after 24 h assessed by*ex vivo* imaging [160]. In addition to tumor diagnostic imaging, pyropheophorbide labeled 2-deoxyglucosamine has shown a potential for photodynamic therapy on tumors [173, 174].

The results of *ex vivo* fluorescence imaging showed that the 2-DG dye distributed well into the whole tumor despite some heterogeneity (Figure 4-5). This observation may suggest delivery and distribution of the 2-DG dye to the tumor does not need the BBB disruption, which is the prerequisite condition for the dyes currently used for neurosurgery. Indeed, uncoupling of tumor vascular perfusion and permeability and uptake of FDG has been reported previously[175, 176]. However, it is still possible that the dye first leaks out through the disrupted BBB, from which it diffuses into the whole tumor. Further studies will be necessary using earlier stage of tumors, when the Gd contrast leakage is not obviously seen by T_1-weighted contrast enhanced MRI, to prove this hypothesis. Furthermore, the usefulness of the 2-DG dye to stain the infiltrative tumor cells is limited by the tumor model used in this study. The U87 tumor has relatively sharp tumor-brain boundaries. GBM models showing more aggressiveness will be

needed to test the ability to stain the finger-shaped infiltrative tumors. Instead of the established GBM cell lines, using surgically resected tumor tissues directly from GBM patients and passing them in animals will generate stable orthotopic GBM xenografts, which show oncogene patterns very similar to primary tumors of patients.

In summary, fluorescence imaging of deoxyglucose uptake in more clinically relevant orthotopic glioma models has not yet been reported. The results may suggest an optimal time for imaging brain tumors based on the glucose analogues. The near-infrared dye labeled 2-DG may serve as a novel imaging probe to noninvasively monitor intracranial tumor burden in preclinical animal models. From a clinical perspective, development of NIR labeled tumor-specific molecules may have the potential to identify the infiltrating glioblastoma intra-operatively, and to improve the extent of resection of selected tumors.

Acknowledgments: I am grateful to Drs. Li Liu and Phillip Thorpe and Mr. Abhijit Bugde for technical and collegial support.

CHAPTER FIVE
Conclusions and future work

Cancer research reveals potential imaging biomarkers that help in tumor diagnosis and prognosis.

The abnormal tumor vasculature has been seen as an important biomarker for tumor imaging. In Chapter 2, I focused on the measurement of rCBV based on DSC MRI. I evaluated the intracranial growth, permeability and BV changes of breast cancer brain metastases in mouse model longitudinally using high field strength MRI. High resolution T_2-weighted images enabled the detection of multifocal tumor initiation at very early stage (lesions with diameter as small as 310 μm were visible). Longitudinal monitoring of BTB permeability based on T_1-weighted contrast enhanced images showed that at early stages (week 2 or 3) brain metastases, the BTB was exclusively impermeable. At later stage (week 4 or 5), T_1 contrast enhancement was only found in a small proportion (34%) of brain metastases, indicating that the BTB was still intact in the majority of the metastases. Notably, partial enhanced lesions were observed indicating the inhomogeneity of BTB disruption. DSC MRI measurement of rCBV revealed significantly lower rCBV of brain metastases than that of contralateral normal brain. The rCBV data were in agreement with histological findings. MVD was significantly lower in metastatic tumors compared to contralateral normal brain. No correlations were found between tumor size, permeability and rCBV.

Longitudinal rCBV measurement showed that rCBV of individual metastases at early stage was similar to their healthy counterparts, but became significantly lower at later stages.

In chapter 2, intracardiac injection of 231-Br cells was used to mimic the hemodynamic spread of breast cancer in clinic scenarios. Using this tumor cell line, I demonstrated the feasibility of monitoring the development of multi-focal intracranial metastases as well as the changes in vasculature permeability and perfusion. However, the rapid progression of the brain metastasis caused the short life span of the animals. Usually, the animals were only able to survival for one to two additional weeks after the lesions became visible. Majority of the lesions remained small (mean diameter = 0.7mm) with intact BBB at the last time point. Rodent breast cancer 4T1 and human breast cancer MCF7 cells form solitary lesions in brain following intracardiac injection. The lesions from those cell lines are often larger in size compared to the multi-focal lesions of 231-Br. Extending the study to 4T1 and MCF7 cell lines allows the assessment of breast cancer metastases with more variety in size for a longer period of time. Those studies can provide further insight into the longitudinal tumor perfusion changes along with the breast cancer metastases development.

In addition, solitary breast cancer metastasis in brain is often seen in patients with similar conventional MRI appearance, and distinguishing metastases from primary tumor is necessary for treatment planning. Comparison of the rCBV

values of different breast cancer brain metastases models (multi-focal metastases from 231-Br, or solitary lesion formed by 4T1 or MCF7) with orthotopic GBM model may provide valuable information in this aspect.

In addition to the morphology and functional changes of tumor vasculature, I studied the abnormality of tumor vessels on the cellular and molecular level. In Chapter 3, I demonstrated the use of PGN635 to image PS using MRI. Both *in vitro* and *in vivo* study verified the binding of SPIO conjugated PGN635 and showed elevated PS binding upon irradiation. In the subcutaneous tumor models, the distribution of the contrast appeared to be inhomogeneous across the tumors. Sparse signal loss was observed on the T_2 weighted images after the administration of SPIO-PGN635. The area of signal loss was calculated and normalized to the percentage fractions of whole tumor volume. An increase was observed in the irradiated tumor (5.0±1.1%), which was significantly larger than the non-irradiated tumor (2.7±0.4%). Prussian blue staining confirmed the accumulation of SPIO-PGN635 in the tumors. Control antibody conjugated SPIOs did not show this effect confirming the antigen specificity.

Future studies can be performed to image metastatic lesions in brain. Although previously high level of PS exposure had been observed in the brain metastases following intracardiac injection of 231-Br cells, no significant particle deposition can be seen on T_2 and T_2* MRI. The sensitivity of SPIO-PGN635 was not sufficient in detecting the small lesions. Relatively large sized single nodule

can be achieved by intracardiac injection of 4T1 or MCF7 cells, which may help increase the number of SPIO accumulated in one lesion. They may serve as a good animal model to test the agent in intracranial metastases. Another possible direction for future work is to increase the sensitivity of the imaging agent itself. Larger sized iron oxide or a group of clustered SPIO encapsulated by liposomes or micelles can significantly increase the contrast payload, cause greater susceptibility and thus enhance the sensitivity. I have previously observed stronger signal loss in subcutaneous tumor models (U87 and 4T1) using micro-particles of iron oxide or liposome encapsulating a group of SPIO. SPIO-encapsulated liposome is especially promising. When compared to SPIO-PGN635 which were mostly binding to cell membrane and staying outside of the cells, the liposome can be absorbed by the ECs through endocytosis. This feature highlights the potential of combining imaging and therapy by encapsulating drugs together with SPIOs in the liposome.

In Chapter 4, I demonstrated the feasibility of using IRDye800CW 2-DG, for *in vivo* FLI of orthotopic glioma in a mouse model. The *in vivo* imaging results were confirmed by ex vivo fluorescent imaging and microscopic imaging. The intracranial tumor boundary including the infiltrative tumor was nicely visualized in ex vivo FLI. IRDye800CW 2-DG showed potential use as an intra-operative imaging probe to help identify the tumor boundary and improve GBM resection.

However, the underlying principles of the tumor uptake of IRDye800CW 2-DG remain obscure. It is not clear if the dye was transferred into the cells through GLUTs like glucose. Applying GLUT inhibitors before administration of IRDye800CW 2-DG, should potentially helps better understand the mechanism. If the signal is significantly weaker comparing to the previous results without GLUT inhibiting, then IRDye800CW 2-DG is probably transferred into the cells by GLUTs.

Bibliography

1. Centers for Disease Control and Prevention. *Leading Causes of Death*. 2010.
2. *Central Brain Tumor Registry of the United States (CBTRUS): 2010 CBTRUS Statistical Report: Primary Brain and Central Nervous System Tumors Diagnosed in the United States in 2004-2006* 2010.
3. Kelly, K.A., J.M. Kirkwood, and D.S. Kapp, *Glioblastoma multiforme: Pathology, natural history and treatment.* Cancer Treatment Reviews, 1984. **11**(1): p. 1-26.
4. Iacob, G. and E.B. Dinca, *Current data and strategy in glioblastoma multiforme.* Journal of Medicine & Life, 2009. **2**(4): p. 386-393.
5. Ferrarese, F., V. Baggio, P. Zorat, and D. Fiore, *Treatment and prophylaxis for brain metastases from non-small cell lung cancer: whole brain radiation treatment versus stereotactic radiosurgery.* Annals of Oncology, 2006. **17**.
6. Petrovich, Z., C. Yu, S.L. Giannotta, S. O'day, and M.L.J. Apuzzo, *Survival and pattern of failure in brain metastasis treated with stereotactic gamma knife radiosurgery.* Journal of Neurosurgery, 2002. **97**(supplement 5): p. 499-506.
7. Alexander, E., T.M. Moriarty, R.B. Davis, P.Y. Wen, H.A. Fine, P.M. Black, H.M. Kooy, and J.S. Loeffler, *Stereotactic Radiosurgery for the Definitive, Noninvasive Treatment of Brain Metastases.* Journal of the National Cancer Institute, 1995. **87**(1): p. 34-40.
8. Bindal, R.K., R. Sawaya, M.E. Leavens, and J.J. Lee, *Surgical treatment of multiple brain metastases.* Journal of Neurosurgery, 1993. **79**(2): p. 210-216.
9. Schouten, L.J., J. Rutten, H.A.M. Huveneers, and A. Twijnstra, *Incidence of brain metastases in a cohort of patients with carcinoma of the breast, colon, kidney, and lung and melanoma.* Cancer, 2002. **94**(10): p. 2698-2705.
10. Yamanaka, R., *Medical Management of Brain Metastases from Lung Cancer*. Brain Tumors - Current and Emerging Therapeutic Strategies2011.
11. Miller, K.D., T. Weathers, L.G. Haney, R. Timmerman, M. Dickler, J. Shen, and G.W. Sledge Jr, *Occult central nervous system involvement in patients with metastatic breast cancer: prevalence, predictive factors and impact on overall survival.* Annals of Oncology, 2003. **14**(7): p. 1072-1077.

12. Tsukada, Y., A. Fouad, J.W. Pickren, and W.W. Lane, *Central nervous system metastasis from breast carcinoma autopsy study.* Cancer, 1983. **52**(12): p. 2349-2354.
13. McWilliams, R.R., R.D. Rao, J.C. Buckner, M.J. Link, S. Markovic, and P.D. Brown, *Melanoma-induced brain metastases.* Expert review of anticancer therapy, 2008. **8**(5): p. 743-755.
14. Carbonell, W.S., O. Ansorge, N. Sibson, and R. Muschel, *The Vascular Basement Membrane as "Soil" in Brain Metastasis.* PLoS ONE, 2009. **4**(6): p. e5857.
15. Black, K. and N. Ningaraj, *Modulation of Brain Tumor Capillaries for Enhanced Drug Delivery Selectively to Brain Tumor.* Cancer control, 2004. **11**(3): p. 165-173.
16. Cheng, X. and M.-C. Hung, *Breast cancer brain metastases.* Cancer and Metastasis Reviews, 2007. **26**(3): p. 635-643.
17. Clark, R.K., *Anatomy and physiology: understanding the human body.* 2005.
18. Lesniak, M.S. and H. Brem, *Targeted therapy for brain tumours.* Nat Rev Drug Discov, 2004. **3**(6): p. 499-508.
19. Lockman, P.R., R.K. Mittapalli, K.S. Taskar, V. Rudraraju, B. Gril, K.A. Bohn, C.E. Adkins, A. Roberts, H.R. Thorsheim, J.A. Gaasch, S. Huang, D. Palmieri, P.S. Steeg, and Q.R. Smith, *Heterogeneous blood-tumor barrier permeability determines drug efficacy in experimental brain metastases of breast cancer.* Clin Cancer Res, 2010. **16**(23): p. 5664-78.
20. Weinhouse, S., O. Warburg, D. Burk, and S.A. L., *On Respiratory Impairment in Cancer Cells.* Science, 1956. **124**(3215): p. 267-272.
21. Gatenby, R.A. and R.J. Gillies, *Why do cancers have high aerobic glycolysis?* Nature Reviews Cancer, 2004. **4**(11): p. 891-899.
22. Folkman, J., *Tumor Angiogenesis: Therapeutic Implications.* New England Journal of Medicine, 1971. **285**(21): p. 1182-1186.
23. Papetti, M. and I.M. Herman, *Mechanisms of normal and tumor-derived angiogenesis.* American Journal of Physiology - Cell Physiology, 2002. **282**(5): p. C947-C970.
24. Klagsbrun, M. and P.A. D'Amore, *Regulators of angiogenesis.* Annual Review of Physiology, 1991. **53**(1): p. 217-239.
25. Brown, J.M. and A.J. Giaccia, *The Unique Physiology of Solid Tumors: Opportunities (and Problems) for Cancer Therapy.* Cancer Research, 1998. **58**(7): p. 1408-1416.
26. Turkbey, B., H. Kobayashi, M. Ogawa, M. Bernardo, and P.L. Choyke, *Imaging of Tumor Angiogenesis: Functional or Targeted?* American Journal of Roentgenology, 2009. **193**(2): p. 304-313.

27. Hanahan, D. and Robert A. Weinberg, *Hallmarks of Cancer: The Next Generation.* Cell, 2011. **144**(5): p. 646-674.
28. Fidler, I.J., S. Yano, R.-d. Zhang, T. Fujimaki, and C.D. Bucana, *The seed and soil hypothesis: vascularisation and brain metastases.* Lancet Oncology, 2002. **3**: p. 53-57.
29. Leenders, W.P., B. Küsters, K. Verrijp, C. Maass, P. Wesseling, A. Heerschap, D. Ruiter, A. Ryan, and R. de Waal, *Antiangiogenic therapy of cerebral melanoma metastases results in sustained tumor progression via vessel co-option.* Clinical Cancer Research, 2004. **10**(18): p. 6222-6230.
30. Wesseling, P., D.J. Ruiter, and P.C. Burger, *Angiogenesis in brain tumors; pathobiological and clinical aspects.* Journal of Neuro-Oncology, 1997. **32**(3): p. 253-265.
31. Küsters, B., W.P. Leenders, P. Wesseling, D. Smits, K. Verrijp, D.J. Ruiter, J.P. Peters, A.J. van der Kogel, and R.M. de Waal, *Vascular endothelial growth factor-A165 induces progression of melanoma brain metastases without induction of sprouting angiogenesis.* Cancer Research, 2002. **62**(2): p. 341-345.
32. Vermeulen, P.B., C. Colpaert, R. Salgado, R. Royers, H. Hellemans, E. Van den Heuvel, G. Goovaerts, L.Y. Dirix, and E. Van Marck, *Liver metastases from colorectal adenocarcinomas grow in three patterns with different angiogenesis and desmoplasia.* The Journal of pathology, 2001. **195**(3): p. 336-342.
33. Leenders, W.P., B. Küsters, and R.M. de Waal, *Vessel co-option: how tumors obtain blood supply in the absence of sprouting angiogenesis.* Endothelium, 2002. **9**(2): p. 83-87.
34. Yu, J.X., R.R. Hallac, S. Chiguru, and R.P. Mason, *New Frontiers and Developing Applications in< sup> 19</sup> F NMR.* Progress in Nuclear Magnetic Resonance Spectroscopy, 2013.
35. Bergers, G. and L.E. Benjamin, *Tumorigenesis and the angiogenic switch.* Nature Reviews Cancer, 2003. **3**: p. 401-410.
36. Holash, J., S. Wiegand, and G. Yancopoulos, *New model of tumor angiogenesis: dynamic balance between vessel regression and growth mediated by angiopoietins and VEGF.* Oncogene, 1999. **18**(38): p. 5356.
37. Vajkoczy, P., M. Farhadi, A. Gaumann, R. Heidenreich, R. Erber, A. Wunder, J.C. Tonn, M.D. Menger, and G. Breier, *Microtumor growth initiates angiogenic sprouting with simultaneous expression of VEGF, VEGF receptor-2, and angiopoietin-2.* Journal of Clinical Investigation, 2002. **109**(6): p. 777-786.
38. Neri, D. and R. Bicknell, *Tumour vascular targeting.* Nature Reviews Cancer, 2005. **5**(6): p. 436-446.

39. Mailhos, C., J. Lewis, D. Ish-Horowicz, U. Modlich, A. Harris, and R. Bicknell, *Delta4, an endothelial specific Notch ligand expressed at sites of physiological and tumor angiogenesis.* Differentiation, 2001. **69**(2-3): p. 135-144.
40. Zwaal, R.F.A. and A.J. Schroit, *Pathophysiologic Implications of Membrane Phospholipid Asymmetry in Blood Cells.* Blood, 1997. **89**(4): p. 1121-1132.
41. Balasubramanian, K. and A.J. Schroit, *AMINOPHOSPHOLIPID ASYMMETRY: A Matter of Life and Death.* Annual Review of Physiology, 2003. **65**(1): p. 701-734.
42. Bombeli, T., A. Karsan, J.F. Tait, and J.M. Harlan, *Apoptotic Vascular Endothelial Cells Become Procoagulant.* Blood, 1997. **89**(7): p. 2429-2442.
43. Ran, S., A. Downes, and P.E. Thorpe, *Increased Exposure of Anionic Phospholipids on the Surface of Tumor Blood Vessels.* Cancer Research, 2002. **62**(21): p. 6132-6140.
44. Boyle, E.M., Jr, T.H. Pohlman, C.J. Cornejo, and E.D. Verrier, *Endothelial Cell Injury in Cardiovascular Surgery: Ischemia-Reperfusion.* Ann Thorac Surg, 1996. **62**(6): p. 1868-1875.
45. Sugimura, M., R. Donato, V.V. Kakkar, and M.F. Scully, *Annexin V as a probe of the contribution of anionic phospholipids to the procoagulant activity of tumour cell surfaces.* Blood coagulation & fibrinolysis : an international journal in haemostasis and thrombosis, 1994. **5**(3): p. 365-73.
46. Ran, S., J. He, X. Huang, M. Soares, D. Scothorn, and P.E. Thorpe, *Antitumor Effects of a Monoclonal Antibody that Binds Anionic Phospholipids on the Surface of Tumor Blood Vessels in Mice.* Clinical Cancer Research, 2005. **11**(4): p. 1551-1562.
47. Ran, S. and P.E. Thorpe, *Phosphatidylserine is a marker of tumor vasculature and a potential target for cancer imaging and therapy.* International journal of radiation oncology, biology, physics, 2002. **54**(5): p. 1479-1484.
48. Stafford, J.H. and P.E. Thorpe, *Increased exposure of phosphatidylethanolamine on the surface of tumor vascular endothelium.* Neoplasia (New York, NY), 2011. **13**(4): p. 299.
49. He, J., Y. Yin, T.A. Luster, L. Watkins, and P.E. Thorpe, *Antiphosphatidylserine Antibody Combined with Irradiation Damages Tumor Blood Vessels and Induces Tumor Immunity in a Rat Model of Glioblastoma.* Clinical Cancer Research, 2009. **15**(22): p. 6871-6880.
50. Huang, X., M. Bennett, and P.E. Thorpe, *A Monoclonal Antibody that Binds Anionic Phospholipids on Tumor Blood Vessels Enhances the*

Antitumor Effect of Docetaxel on Human Breast Tumors in Mice. Cancer Research, 2005. **65**(10): p. 4408-4416.

51. Zulueta, J.J., F.S. Yu, I.A. Hertig, V.J. Thannickal, and P.M. Hassoun, *Release of hydrogen peroxide in response to hypoxia-reoxygenation: role of an NAD(P)H oxidase-like enzyme in endothelial cell plasma membrane.* American Journal of Respiratory Cell and Molecular Biology, 1995. **12**(1): p. 41-9.
52. He, J., T.A. Luster, and P.E. Thorpe, *Radiation-Enhanced Vascular Targeting of Human Lung Cancers in Mice with a Monoclonal Antibody That Binds Anionic Phospholipids.* Clinical Cancer Research, 2007. **13**(17): p. 5211-5218.
53. Zhao, D., J. Stafford, H. Zhou, and P. Thorpe, *Near-infrared Optical Imaging of Exposed Phosphatidylserine in a Mouse Glioma Model.* Translational oncology, 2011. **4**(6): p. 355-364.
54. Brindle, K., *New approaches for imaging tumour responses to treatment.* Nature Reviews Cancer, 2008. **8**(2): p. 94-107.
55. Morgan, B., *Opportunities and pitfalls of cancer imaging in clinical trials.* Nature Reviews Clinical Oncology, 2011. **8**(9): p. 517-527.
56. Cole, A.J., V.C. Yang, and A.E. David, *Cancer theranostics: the rise of targeted magnetic nanoparticles.* Trends in biotechnology, 2011. **29**(7): p. 323-332.
57. Bulte, J.W.M. and D.L. Kraitchman, *Iron oxide MR contrast agents for molecular and cellular imaging.* NMR in Biomedicine, 2004. **17**(7): p. 484-499.
58. Gatenby, R.A. and R.J. Gillies, *Why do cancers have high aerobic glycolysis?* Nat Rev Cancer, 2004. **4**(11): p. 891-899.
59. Gambhir, S.S., *Molecular imaging of cancer with positron emission tomography.* Nat Rev Cancer, 2002. **2**(9): p. 683-693.
60. Cai, W., K. Chen, K.A. Mohamedali, Q. Cao, S.S. Gambhir, M.G. Rosenblum, and X. Chen, *PET of Vascular Endothelial Growth Factor Receptor Expression.* Journal of Nuclear Medicine, 2006. **47**(12): p. 2048-2056.
61. Chen, X., Y. Hou, M. Tohme, R. Park, V. Khankaldyyan, I. Gonzales-Gomez, J.R. Bading, W.E. Laug, and P.S. Conti, *Pegylated Arg-Gly-Asp Peptide: 64Cu Labeling and PET Imaging of Brain Tumor αvβ3-Integrin Expression.* Journal of Nuclear Medicine, 2004. **45**(10): p. 1776-1783.
62. Kessinger, C.W., C. Khemtong, O. Togao, M. Takahashi, B.D. Sumer, and J. Gao, *In vivo angiogenesis imaging of solid tumors by αvβ3-targeted, dual-modality micellar nanoprobes.* Experimental Biology and Medicine, 2010. **235**(8): p. 957-965.

63. Zhang, X., Z. Xiong, Y. Wu, W. Cai, J.R. Tseng, S.S. Gambhir, and X. Chen, *Quantitative PET Imaging of Tumor Integrin αvβ3 Expression with 18F-FRGD2.* Journal of Nuclear Medicine, 2006. **47**(1): p. 113-121.
64. Svoboda, K. and S.M. Block, *Biological applications of optical forces.* Annual review of biophysics and biomolecular structure, 1994. **23**(1): p. 247-285.
65. Rehemtulla, A., L.D. Stegman, S.J. Cardozo, S. Gupta, D.E. Hall, C.H. Contag, and B.D. Ross, *Rapid and quantitative assessment of cancer treatment response using in vivo bioluminescence imaging.* Neoplasia (New York, N.Y.), 2000. **2**(6): p. 491-495.
66. Leon, S.P., R.D. Folkerth, and P.M. Black, *Microvessel density is a prognostic indicator for patients with astroglial brain tumors.* Cancer, 1996. **77**(2): p. 362-372.
67. Weidner, N., *Current pathologic methods for measuring intratumoral microvessel density within breast carcinoma and other solid tumors.* Breast cancer research and treatment, 1995. **36**(2): p. 169-180.
68. Weidner, N., *Intratumor microvessel density as a prognostic factor in cancer*. The American journal of pathology, 1995. **147**(1): p. 9.
69. Chandrachud LM, Pendleton N, Chisholm DM, Horan MA, and S. AM., *Relationship between vascularity, age and survival in non-small-cell lung cancer*. 1997;76(10):1367-75., 1997. **76**(10): p. 367-75.
70. Weidner, N., J.P. Semple, W.R. Welch, and J. Folkman, *Tumor Angiogenesis and Metastasis — Correlation in Invasive Breast Carcinoma.* New England Journal of Medicine, 1991. **324**(1): p. 1-8.
71. Artemov, D., N. Mori, B. Okollie, and Z.M. Bhujwalla, *MR molecular imaging of the Her-2/neu receptor in breast cancer cells using targeted iron oxide nanoparticles.* Magnetic Resonance in Medicine, 2003. **49**(3): p. 403-408.
72. Khemtong, C., C.W. Kessinger, J. Ren, E.A. Bey, S.-G. Yang, J.S. Guthi, D.A. Boothman, A.D. Sherry, and J. Gao, *In vivo Off-Resonance Saturation Magnetic Resonance Imaging of αvβ3-Targeted Superparamagnetic Nanoparticles.* Cancer Research, 2009. **69**(4): p. 1651-1658.
73. Mulder, W.J.M., G.J. Strijkers, J.W. Habets, E.J.W. Bleeker, D.W.J. van der Schaft, G. Storm, G.A. Koning, A.W. Griffioen, and K. Nicolay, *MR molecular imaging and fluorescence microscopy for identification of activated tumor endothelium using a bimodal lipidic nanoparticle.* The FASEB Journal, 2005. **19**(14): p. 2008-2010.
74. O'Connor, J.P.B., A. Jackson, G.J.M. Parker, and G.C. Jayson, *DCE-MRI biomarkers in the clinical evaluation of antiangiogenic and vascular disrupting agents.* Br J Cancer, 2007. **96**(2): p. 189-195.

75. Roberts, H.C., T.P.L. Roberts, T.-Y. Lee, and W.P. Dillon, *Dynamic, Contrast-Enhanced CT of Human Brain Tumors: Quantitative Assessment of Blood Volume, Blood Flow, and Microvascular Permeability: Report of Two Cases.* American Journal of Neuroradiology, 2002. **23**(5): p. 828-832.
76. Thomas, D.L., M.F. Lythgoe, L. van der Weerd, R.J. Ordidge, and D.G. Gadian, *Regional variation of cerebral blood flow and arterial transit time in the normal and hypoperfused rat brain measured using continuous arterial spin labeling MRI.* J Cereb Blood Flow Metab, 2005. **26**(2): p. 274-282.
77. Shen, Q. and T. Duong, *Background suppression in arterial spin labeling MRI with a separate neck labeling coil.* NMR in Biomedicine, 2010. **24**: p. 1111-1118.
78. Rosen, B.R., J.W. Belliveau, H.J. Aronen, D. Kennedy, B.R. Buchbinder, A. Fischman, M. Gruber, J. Glas, R.M. Weisskoff, M.S. Cohen, F.H. Hochberg, and T.J. Brady, *Susceptibility contrast imaging of cerebral blood volume: Human experience.* Magnetic Resonance in Medicine, 1991. **22**(2): p. 293-299.
79. Kosaka, N., H. Uematsu, H. Kimura, Y. Ishimori, T. Kurokawa, T. Matsuda, and H. Itoh, *Assessment of the Vascularity of Uterine Leiomyomas Using Double-Echo Dynamic Perfusion-Weighted MRI With the First-Pass Pharmacokinetic Model: Correlation With Histopathology.* Investigative Radiology, 2007. **42**(9): p. 629-635 10.1097/RLI.0b013e318059ae69.
80. Johnson, G., S.G. Wetzel, S. Cha, J. Babb, and P.S. Tofts, *Measuring blood volume and vascular transfer constant from dynamic, T 2*-weighted contrast-enhanced MRI.* Magnetic Resonance in Medicine, 2004. **51**(5): p. 961-968.
81. Uematsu, H., M. Maeda, N. Sadato, T. Matsuda, Y. Ishimori, Y. Koshimoto, H. Yamada, H. Kimura, Y. Kawamura, T. Matsuda, N. Hayashi, Y. Yonekura, and Y. Ishii, *Vascular Permeability: Quantitative Measurement with Double-Echo Dynamic MR Imaging—Theory and Clinical Application1*. Radiology, 2000. **214**(3): p. 912-917.
82. Villringer, A., B.R. Rosen, J.W. Belliveau, J.L. Ackerman, R.B. Lauffer, R.B. Buxton, Y.-S. Chao, V.J. Wedeenand, and T.J. Brady, *Dynamic imaging with lanthanide chelates in normal brain: Contrast due to magnetic susceptibility effects.* Magnetic Resonance in Medicine, 1988. **6**(2): p. 164-174.
83. Rosen, B.R., J.W. Belliveau, J.M. Vevea, and T.J. Brady, *Perfusion imaging with NMR contrast agents.* Magnetic Resonance in Medicine, 1990. **14**(2): p. 249-265.

84. Aronen, H.J., I.E. Gazit, D.N. Louis, B.R. Buchbinder, F.S. Pardo, R.M. Weisskoff, G.R. Harsh, G.R. Cosgrove, E.F. Halpern, and F.H. Hochberg, *Cerebral blood volume maps of gliomas: comparison with tumor grade and histologic findings.* Radiology, 1994. **191**(1): p. 41-51.
85. Bruening, R., K. Kwong, M. Vevea, F. Hochberg, L. Cher, G. Harsh, 4th, P. Niemi, R. Weisskoff, and B. Rosen, *Echo-planar MR determination of relative cerebral blood volume in human brain tumors: T1 versus T2 weighting.* AJNR Am J Neuroradiol, 1996. **17**(5): p. 831-840.
86. Sugahara, T., Y. Korogi, M. Kochi, I. Ikushima, T. Hirai, T. Okuda, Y. Shigematsu, L. Liang, Y. Ge, Y. Ushio, and M. Takahashi, *Correlation of MR imaging-determined cerebral blood volume maps with histologic and angiographic determination of vascularity of gliomas.* Am. J. Roentgenol., 1998. **171**(6): p. 1479-1486.
87. Provenzale, J.M., G.R. Wang, T. Brenner, J.R. Petrella, and A.G. Sorensen, *Comparison of permeability in high-grade and low-grade brain tumors using dynamic susceptibility contrast MR imaging.* American Journal of Roentgenology, 2002. **178**(3): p. 711-716.
88. Kremer, S., S. Grand, C. Remy, F. Esteve, V. Lefournier, B. Pasquier, D. Hoffmann, A. Benabid, and J. Le Bas, *Cerebral blood volume mapping by MR imaging in the initial evaluation of brain tumors.* Journal of neuroradiology. Journal de neuroradiologie, 2002. **29**(2): p. 105.
89. Hartmann, M., S. Heiland, I. Harting, V.M. Tronnier, C. Sommer, R. Ludwig, and K. Sartor, *Distinguishing of primary cerebral lymphoma from high-grade glioma with perfusion-weighted magnetic resonance imaging.* Neuroscience letters, 2003. **338**(2): p. 119-122.
90. Kremer, S., S. Grand, C. Remy, B. Pasquier, A. Benabid, S. Bracard, and J. Le Bas, *Contribution of dynamic contrast MR imaging to the differentiation between dural metastasis and meningioma.* Neuroradiology, 2004. **46**(8): p. 642-648.
91. Young, G.S. and K. Setayesh, *Spin-Echo Echo-Planar Perfusion MR Imaging in the Differential Diagnosis of Solitary Enhancing Brain Lesions: Distinguishing Solitary Metastases from Primary Glioma.* AJNR Am J Neuroradiol, 2009. **30**(3): p. 575-577.
92. Jennings, D., N. Raghunand, and R. Gillies, *Imaging hemodynamics.* Cancer and Metastasis Reviews, 2008. **27**(4): p. 589-613.
93. Farrar, C.T., W.S. Kamoun, C.D. Ley, Y.R. Kim, S.J. Kwon, G. Dai, B.R. Rosen, E. di Tomaso, R.K. Jain, and A.G. Sorensen, *In vivo validation of MRI vessel caliber index measurement methods with intravital optical microscopy in a U87 mouse brain tumor model.* Neuro-Oncology, 2010. **12**(4): p. 341-350.

94. O'Connor, J.P.B., J.H. Naish, A. Jackson, J.C. Waterton, Y. Watson, S. Cheung, D.L. Buckley, D.M. McGrath, G.A. Buonaccorsi, S.J. Mills, C. Roberts, G.C. Jayson, and G.J.M. Parker, *Comparison of normal tissue R1 and R*2 modulation by oxygen and carbogen.* Magnetic Resonance in Medicine, 2009. **61**(1): p. 75-83.
95. Hallac, R.R., Y. Ding, Q. Yuan, R.W. McColl, J. Lea, R.D. Sims, P.T. Weatherall, and R.P. Mason, *Oxygenation in cervical cancer and normal uterine cervix assessed using blood oxygenation level-dependent (BOLD) MRI at 3T.* NMR Biomed, 2012. **early view**: p. DOI: 10.1002/nbm.2804.
96. Jiang, L., D. Zhao, A. Constantinescu, and R.P. Mason, *Comparison of BOLD contrast and Gd-DTPA dynamic contrast-enhanced imaging in rat prostate tumor.* Magnetic Resonance in Medicine, 2004. **51**(5): p. 953-960.
97. Backer, M.V., Z. Levashova, V. Patel, B.T. Jehning, K. Claffey, F.G. Blankenberg, and J.M. Backer, *Molecular imaging of VEGF receptors in angiogenic vasculature with single-chain VEGF-based probes.* Nature medicine, 2007. **13**(4): p. 504-509.
98. Kessinger, C.W., O. Togao, C. Khemtong, G. Huang, M. Takahashi, and J. Gao, *Investigation of in vivo targeting kinetics of αvβ3-specific superparamagnetic nanoprobes by time-resolved MRI.* Theranostics, 2011. **1**: p. 263.
99. Hsu, A.R., L.C. Hou, A. Veeravagu, J.M. Greve, H. Vogel, V. Tse, and X. Chen, *In vivo near-infrared fluorescence imaging of integrin α v β 3 in an orthotopic glioblastoma model.* Molecular Imaging and Biology, 2006. **8**(6): p. 315-323.
100. Gaertner, F., M. Schwaiger, and A. Beer, *Molecular imaging of avb3 expression in cancer patients.* The quarterly journal of nuclear medicine and molecular imaging: official publication of the Italian Association of Nuclear Medicine (AIMN)[and] the International Association of Radiopharmacology (IAR),[and] Section of the Society of... 2010.
101. Jun, Y.-w., J.-t. Jang, and J. Cheon, *Magnetic nanoparticle assisted molecular MR imaging.* Bio-Applications of Nanoparticles, 2007: p. 85-106.
102. Jennewein, M., M.A. Lewis, D. Zhao, E. Tsyganov, N. Slavine, J. He, L. Watkins, V.D. Kodibagkar, S. O'Kelly, P. Kulkarni, P.P. Antich, A. Hermanne, F. Rösch, R.P. Mason, and P.E. Thorpe, *Vascular Imaging of Solid Tumors in Rats with a Radioactive Arsenic-Labeled Antibody that Binds Exposed Phosphatidylserine.* Clinical Cancer Research, 2008. **14**(5): p. 1377-1385.
103. Schouten, L.J., J. Rutten, H.A. Huveneers, and A. Twijnstra, *Incidence of brain metastases in a cohort of patients with carcinoma of the breast,*

colon, kidney, and lung and melanoma. Cancer, 2002. **94**(10): p. 2698-705.

104. Lin, N.U., J.R. Bellon, and E.P. Winer, *CNS metastases in breast cancer.* J Clin Oncol, 2004. **22**(17): p. 3608-17.
105. Eichler, A.F., E. Chung, D.P. Kodack, J.S. Loeffler, D. Fukumura, and R.K. Jain, *The biology of brain metastases-translation to new therapies.* Nat Rev Clin Oncol, 2011.
106. Jemal, A., R. Siegel, J. Xu, and E. Ward, *Cancer Statistics, 2010.* CA Cancer J Clin, 2010. **60**(5): p. 277-300.
107. Hurwitz, H., L. Fehrenbacher, W. Novotny, T. Cartwright, J. Hainsworth, W. Heim, J. Berlin, A. Baron, S. Griffing, E. Holmgren, N. Ferrara, G. Fyfe, B. Rogers, R. Ross, and F. Kabbinavar, *Bevacizumab plus irinotecan, fluorouracil, and leucovorin for metastatic colorectal cancer.* N Engl J Med, 2004. **350**(23): p. 2335 - 2342.
108. Bendell, J.C., S.M. Domchek, H.J. Burstein, L. Harris, J. Younger, I. Kuter, C. Bunnell, M. Rue, R. Gelman, and E. Winer, *Central nervous system metastases in women who receive trastuzumab-based therapy for metastatic breast carcinoma.* Cancer, 2003. **97**(12): p. 2972-2977.
109. Melisko, M., D. Moore, P. Sneed, J. De Franco, and H. Rugo, *Brain metastases in breast cancer: clinical and pathologic characteristics associated with improvements in survival.* Journal of Neuro-Oncology, 2008. **88**(3): p. 359-365.
110. Subramanian, A., A. Harris, K. Piggott, C. Shieff, and R. Bradford, *Metastasis to and from the central nervous system--the 'relatively protected site'.* Lancet Oncol, 2002. **3**(8): p. 498-507.
111. Begley, D.J., *Delivery of therapeutic agents to the central nervous system: the problems and the possibilities.* Pharmacol Ther, 2004. **104**(1): p. 29-45.
112. Doolittle, N.D., L.E. Abrey, W.A. Bleyer, S. Brem, T.P. Davis, P. Dore-Duffy, L.R. Drewes, W.A. Hall, J.M. Hoffman, A. Korfel, R. Martuza, L.L. Muldoon, D. Peereboom, D.R. Peterson, S.D. Rabkin, Q. Smith, G.H. Stevens, and E.A. Neuwelt, *New frontiers in translational research in neuro-oncology and the blood-brain barrier: report of the tenth annual Blood-Brain Barrier Disruption Consortium Meeting.* Clin Cancer Res, 2005. **11**(2 Pt 1): p. 421-8.
113. Zhang, R.D., J.E. Price, T. Fujimaki, C.D. Bucana, and I.J. Fidler, *Differential permeability of the blood-brain barrier in experimental brain metastases produced by human neoplasms implanted into nude mice.* Am J Pathol, 1992. **141**(5): p. 1115-24.
114. Yoneda, T., P.J. Williams, T. Hiraga, M. Niewolna, and R. Nishimura, *A bone-seeking clone exhibits different biological properties from the MDA-*

MB-231 parental human breast cancer cells and a brain-seeking clone in vivo and in vitro. J Bone Miner Res, 2001. **16**(8): p. 1486-95.

115. Palmieri, D., J.L. Bronder, J.M. Herring, T. Yoneda, R.J. Weil, A.M. Stark, R. Kurek, E. Vega-Valle, L. Feigenbaum, D. Halverson, A.O. Vortmeyer, S.M. Steinberg, K. Aldape, and P.S. Steeg, *Her-2 overexpression increases the metastatic outgrowth of breast cancer cells in the brain.* Cancer Res, 2007. **67**(9): p. 4190-8.
116. Francia, G., W. Cruz-Munoz, S. Man, P. Xu, and R.S. Kerbel, *Mouse models of advanced spontaneous metastasis for experimental therapeutics.* Nat Rev Cancer, 2011. **11**(2): p. 135-41.
117. Lorger, M. and B. Felding-Habermann, *Capturing changes in the brain microenvironment during initial steps of breast cancer brain metastasis.* Am J Pathol, 2010. **176**(6): p. 2958-71.
118. Percy, D.B., E.J. Ribot, Y. Chen, C. McFadden, C. Simedrea, P.S. Steeg, A.F. Chambers, and P.J. Foster, *In vivo characterization of changing blood-tumor barrier permeability in a mouse model of breast cancer metastasis: a complementary magnetic resonance imaging approach.* Invest Radiol, 2011. **46**(11): p. 718-25.
119. Song, H.T., E.K. Jordan, B.K. Lewis, W. Liu, J. Ganjei, B. Klaunberg, D. Despres, D. Palmieri, and J.A. Frank, *Rat model of metastatic breast cancer monitored by MRI at 3 tesla and bioluminescence imaging with histological correlation.* J Transl Med, 2009. **7**: p. 88.
120. Villringer, A., B.R. Rosen, J.W. Belliveau, J.L. Ackerman, R.B. Lauffer, R.B. Buxton, Y.S. Chao, V.J. Wedeen, and T.J. Brady, *Dynamic imaging with lanthanide chelates in normal brain: contrast due to magnetic susceptibility effects.* Magn Reson Med, 1988. **6**(2): p. 164-74.
121. Knopp, E.A., S. Cha, G. Johnson, A. Mazumdar, J.G. Golfinos, D. Zagzag, D.C. Miller, P.J. Kelly, and Kricheff, II, *Glial neoplasms: dynamic contrast-enhanced T2*-weighted MR imaging.* Radiology, 1999. **211**(3): p. 791-8.
122. Cha, S., G. Johnson, Y.Z. Wadghiri, O. Jin, J. Babb, D. Zagzag, and D.H. Turnbull, *Dynamic, contrast-enhanced perfusion MRI in mouse gliomas: correlation with histopathology.* Magn Reson Med, 2003. **49**(5): p. 848-55.
123. Yoneda, T., P.J. Williams, T. Hiraga, M. Niewolna, and R. Nishimura, *A Bone-Seeking Clone Exhibits Different Biological Properties from the MDA-MB-231 Parental Human Breast Cancer Cells and a Brain-Seeking Clone In Vivo and In Vitro.* Journal of Bone and Mineral Research, 2001. **16**(8): p. 1486-1495.
124. Johnson, G., S.G. Wetzel, S. Cha, J. Babb, and P.S. Tofts, *Measuring blood volume and vascular transfer constant from dynamic, T_2*-weighted*

contrast-enhanced MRI. Magnetic Resonance in Medicine, 2004. **51**(5): p. 961-968.

125. Peereboom, D.M., *Chemotherapy in brain metastases.* Neurosurgery, 2005. **57**(5 Suppl): p. S54-65; discusssion S1-4.
126. Steeg, P.S., K.A. Camphausen, and Q.R. Smith, *Brain metastases as preventive and therapeutic targets.* Nat Rev Cancer, 2011. **11**(5): p. 352-63.
127. Treat, L.H., N. McDannold, N. Vykhodtseva, Y. Zhang, K. Tam, and K. Hynynen, *Targeted delivery of doxorubicin to the rat brain at therapeutic levels using MRI-guided focused ultrasound.* Int J Cancer, 2007. **121**(4): p. 901-7.
128. Kim, S.G., *Quantification of relative cerebral blood flow change by flow-sensitive alternating inversion recovery (FAIR) technique: application to functional mapping.* Magn Reson Med, 1995. **34**(3): p. 293-301.
129. Wong, E.C., R.B. Buxton, and L.R. Frank, *A theoretical and experimental comparison of continuous and pulsed arterial spin labeling techniques for quantitative perfusion imaging.* Magn Reson Med, 1998. **40**(3): p. 348-55.
130. Danchaivijitr, N., A.D. Waldman, D.J. Tozer, C.E. Benton, G. Brasil Caseiras, P.S. Tofts, J.H. Rees, and H.R. Jager, *Low-grade gliomas: do changes in rCBV measurements at longitudinal perfusion-weighted MR imaging predict malignant transformation?* Radiology, 2008. **247**(1): p. 170-8.
131. Aronen, H.J., I.E. Gazit, D.N. Louis, B.R. Buchbinder, F.S. Pardo, R.M. Weisskoff, G.R. Harsh, G.R. Cosgrove, E.F. Halpern, F.H. Hochberg, and et al., *Cerebral blood volume maps of gliomas: comparison with tumor grade and histologic findings.* Radiology, 1994. **191**(1): p. 41-51.
132. Fidler, I.J., S. Yano, R.D. Zhang, T. Fujimaki, and C.D. Bucana, *The seed and soil hypothesis: vascularisation and brain metastases.* Lancet Oncol, 2002. **3**(1): p. 53-7.
133. Kienast, Y., L. von Baumgarten, M. Fuhrmann, W.E. Klinkert, R. Goldbrunner, J. Herms, and F. Winkler, *Real-time imaging reveals the single steps of brain metastasis formation.* Nat Med, 2010. **16**(1): p. 116-22.
134. Kusters, B., W.P. Leenders, P. Wesseling, D. Smits, K. Verrijp, D.J. Ruiter, J.P. Peters, A.J. van Der Kogel, and R.M. de Waal, *Vascular endothelial growth factor-A(165) induces progression of melanoma brain metastases without induction of sprouting angiogenesis.* Cancer Res, 2002. **62**(2): p. 341-5.
135. Schnell, O., B. Krebs, J. Carlsen, I. Miederer, C. Goetz, R.H. Goldbrunner, H.-J. Wester, R. Haubner, G. Pöpperl, and M. Holtmannspötter, *Imaging of integrin αvβ3 expression in patients with*

malignant glioma by [18F] Galacto-RGD positron emission tomography. Neuro-Oncology, 2009. **11**(6): p. 861-870.

136. Galluzzi, L., E. Vacchelli, W.H. Fridman, J. Galon, C. Sautès-Fridman, E. Tartour, J. Zucman-Rossi, L. Zitvogel, and G. Kroemer, *Trial Watch: Monoclonal antibodies in cancer therapy.* OncoImmunology, 2012. **1**(1): p. 28-37.
137. DeRose, P., P.E. Thorpe, and D.E. Gerber, *Development of bavituximab, a vascular targeting agent with immune-modulating properties, for lung cancer treatment.* Immunotherapy, 2011. **3**(8): p. 933-944.
138. Domanski, P.J., P.R. Patel, A.S. Bayer, L. Zhang, A.E. Hall, P.J. Syribeys, E.L. Gorovits, D. Bryant, J.H. Vernachio, J.T. Hutchins, and J.M. Patti, *Characterization of a Humanized Monoclonal Antibody Recognizing Clumping Factor A Expressed by Staphylococcus aureus.* Infection and Immunity, 2005. **73**(8): p. 5229-5232.
139. Patti, J.M., *A humanized monoclonal antibody targeting Staphylococcus aureus.* Vaccine, 2004. **22, Supplement 1**(0): p. S39-S43.
140. Zhang, C., M. Jugold, E.C. Woenne, T. Lammers, B. Morgenstern, M.M. Mueller, H. Zentgraf, M. Bock, M. Eisenhut, W. Semmler, and F. Kiessling, *Specific Targeting of Tumor Angiogenesis by RGD-Conjugated Ultrasmall Superparamagnetic Iron Oxide Particles Using a Clinical 1.5-T Magnetic Resonance Scanner.* Cancer Research, 2007. **67**(4): p. 1555-1562.
141. Xie, J., G. Liu, H.S. Eden, H. Ai, and X. Chen, *Surface-Engineered Magnetic Nanoparticle Platforms for Cancer Imaging and Therapy.* Accounts of Chemical Research, 2011. **44**(10): p. 883-892.
142. Furnari, F.B., T. Fenton, R.M. Bachoo, A. Mukasa, J.M. Stommel, A. Stegh, W.C. Hahn, K.L. Ligon, D.N. Louis, C. Brennan, L. Chin, R.A. DePinho, and W.K. Cavenee, *Malignant astrocytic glioma: genetics, biology, and paths to treatment.* Genes & development, 2007. **21**(21): p. 2683-2710.
143. Wen, P.Y. and S. Kesari, *Malignant Gliomas in Adults.* New England Journal of Medicine, 2008. **359**(5): p. 492-507.
144. Hsu, A., L. Hou, A. Veeravagu, J. Greve, H. Vogel, V. Tse, and X. Chen, *In Vivo Near-Infrared Fluorescence Imaging of Integrin αvβ3 in an Orthotopic Glioblastoma Model.* Molecular Imaging and Biology, 2006. **8**(6): p. 315-323.
145. Hsu, A.R., W. Cai, A. Veeravagu, K.A. Mohamedali, K. Chen, S. Kim, H. Vogel, L.C. Hou, V. Tse, M.G. Rosenblum, and X. Chen, *Multimodality molecular imaging of glioblastoma growth inhibition with vasculature-targeting fusion toxin VEGF121/rGel.* Journal of nuclear medicine : official publication, Society of Nuclear Medicine, 2007. **48**(3): p. 445-454.

146. McCann, C.M., P. Waterman, J.-L. Figueiredo, E. Aikawa, R. Weissleder, and J.W. Chen, *Combined magnetic resonance and fluorescence imaging of the living mouse brain reveals glioma response to chemotherapy.* NeuroImage, 2009. **45**(2): p. 360-369.
147. Laws, E.R., I.F. Parney, W. Huang, F. Anderson, A.M. Morris, A. Asher, K.O. Lillehei, M. Bernstein, H. Brem, A. Sloan, M.S. Berger, and S. Chang, *Survival following surgery and prognostic factors for recently diagnosed malignant glioma: data from the Glioma Outcomes Project.* Journal of Neurosurgery, 2003. **99**(3): p. 467-473.
148. Barker Ii, F.G. and S.M. Chang, *Improving resection of malignant glioma.* The Lancet Oncology, 2006. **7**(5): p. 359-360.
149. Stummer, W., U. Pichlmeier, T. Meinel, O.D. Wiestler, F. Zanella, and H.-J. Reulen, *Fluorescence-guided surgery with 5-aminolevulinic acid for resection of malignant glioma: a randomised controlled multicentre phase III trial.* The Lancet Oncology, 2006. **7**(5): p. 392-401.
150. Burton, J.B., M. Johnson, M. Sato, S.B. Koh, D.J. Mulholland, D. Stout, A.F. Chatziioannou, M.E. Phelps, H. Wu, and L. Wu, *Adenovirus-mediated gene expression imaging to directly detect sentinel lymph node metastasis of prostate cancer.* Nature medicine, 2008. **14**(8): p. 882-888.
151. Hayashi, K., P. Jiang, K. Yamauchi, N. Yamamoto, H. Tsuchiya, K. Tomita, A.R. Moossa, M. Bouvet, and R.M. Hoffman, *Real-time Imaging of Tumor-Cell Shedding and Trafficking in Lymphatic Channels.* Cancer Research, 2007. **67**(17): p. 8223-8228.
152. Hoffman, R.M., *The multiple uses of fluorescent proteins to visualize cancer in vivo.* Nature reviews. Cancer, 2005. **5**(10): p. 796-806.
153. Kaushal, S., M. McElroy, G. Luiken, M. Talamini, A.R. Moossa, R. Hoffman, and M. Bouvet, *Fluorophore-conjugated anti-CEA Antibody for the Intraoperative Imaging of Pancreatic and Colorectal Cancer.* Journal of Gastrointestinal Surgery, 2008. **12**(11): p. 1938-1950.
154. Parungo, C., S. Ohnishi, A. De Grand, R. Laurence, E. Soltesz, Y. Colson, P. Kang, T. Mihaljevic, L. Cohn, and J. Frangioni, *In Vivo Optical Imaging of Pleural Space Drainage to Lymph Nodes of Prognostic Significance.* Annals of Surgical Oncology, 2004. **11**(12): p. 1085-1092.
155. Sevick-Muraca, E.M., R. Sharma, J.C. Rasmussen, M.V. Marshall, J.A. Wendt, H.Q. Pham, E. Bonefas, J.P. Houston, L. Sampath, K.E. Adams, D.K. Blanchard, R.E. Fisher, S.B. Chiang, R. Elledge, and M.E. Mawad, *Imaging of Lymph Flow in Breast Cancer Patients after Microdose Administration of a Near-Infrared Fluorophore: Feasibility Study1*. Radiology, 2008. **246**(3): p. 734-741.
156. Cheng, Z., J. Levi, Z. Xiong, O. Gheysens, S. Keren, X. Chen, and S.S. Gambhir, *Near-Infrared Fluorescent Deoxyglucose Analogue for Tumor*

Optical Imaging in Cell Culture and Living Mice. Bioconjugate Chemistry, 2006. **17**(3): p. 662-669.

157. O'Neil, R., L. Wu, and N. Mullani, *Uptake of a Fluorescent Deoxyglucose Analog (2-NBDG) in Tumor Cells.* Molecular Imaging and Biology, 2005. **7**(6): p. 388-392.
158. Kovar, J.L., M.A. Simpson, A. Schutz-Geschwender, and D.M. Olive, *A systematic approach to the development of fluorescent contrast agents for optical imaging of mouse cancer models.* Analytical Biochemistry, 2007. **367**(1): p. 1-12.
159. Sampath, L., S. Kwon, S. Ke, W. Wang, R. Schiff, M.E. Mawad, and E.M. Sevick-Muraca, *Dual-Labeled Trastuzumab-Based Imaging Agent for the Detection of Human Epidermal Growth Factor Receptor 2 Overexpression in Breast Cancer.* Journal of Nuclear Medicine, 2007. **48**(9): p. 1501-1510.
160. Kovar, J.L., W. Volcheck, E. Sevick-Muraca, M.A. Simpson, and D.M. Olive, *Characterization and performance of a near-infrared 2-deoxyglucose optical imaging agent for mouse cancer models.* Analytical Biochemistry, 2009. **384**(2): p. 254-262.
161. Hillman, E.M. and A. Moore, *All-optical anatomical co-registration for molecular imaging of small animals using dynamic contrast.* Nature photonics, 2007. **1**(9): p. 526-530.
162. Beattie, B.J., G.J. Förster, R. Govantes, C.H. Le, V.A. Longo, P.B. Zanzonico, L. Bidaut, R.G. Blasberg, and J.A. Koutcher, *Multimodality registration without a dedicated multimodality scanner.* Molecular imaging, 2007. **6**(2): p. 108-120.
163. Weissleder, R. and M. Pittet, *Imaging in the era of molecular oncology.* Nature, 2008. **452**: p. 580-589.
164. Serganova, I. and R.G. Blasberg, *Multi-Modality Molecular Imaging of Tumors.* Hematology/Oncology Clinics of North America, 2006. **20**(6): p. 1215-1248.
165. Zhao, D., E. Richer, P.P. Antich, and R.P. Mason, *Antivascular effects of combretastatin A4 phosphate in breast cancer xenograft assessed using dynamic bioluminescence imaging and confirmed by MRI.* The FASEB Journal, 2008. **22**(7): p. 2445-2451.
166. Adams, K.E., S. Ke, S. Kwon, F. Liang, Z. Fan, Y. Lu, K. Hirschi, M.E. Mawad, M.A. Barry, and E.M. Sevick-Muraca, *Comparison of visible and near-infrared wavelength-excitable fluorescent dyes for molecular imaging of cancer.* Journal of Biomedical Optics, 2007. **12**(2): p. 024017-024017.

167. Chang, S.K., I. Rizvi, N. Solban, and T. Hasan, *In vivo Optical Molecular Imaging of Vascular Endothelial Growth Factor for Monitoring Cancer Treatment.* Clinical Cancer Research, 2008. **14**(13): p. 4146-4153.
168. Diagaradjane, P., J.M. Orenstein-Cardona, N. E. Colón-Casasnovas, A. Deorukhkar, S. Shentu, N. Kuno, D.L. Schwartz, J.G. Gelovani, and S. Krishnan, *Imaging Epidermal Growth Factor Receptor Expression In vivo: Pharmacokinetic and Biodistribution Characterization of a Bioconjugated Quantum Dot Nanoprobe.* Clinical Cancer Research, 2008. **14**(3): p. 731-741.
169. Hama, Y., Y. Urano, Y. Koyama, P.L. Choyke, and H. Kobayashi, *Activatable Fluorescent Molecular Imaging of Peritoneal Metastases following Pretargeting with a Biotinylated Monoclonal Antibody.* Cancer Research, 2007. **67**(8): p. 3809-3817.
170. Ke, S., X. Wen, M. Gurfinkel, C. Charnsangavej, S. Wallace, E.M. Sevick-Muraca, and C. Li, *Near-Infrared Optical Imaging of Epidermal Growth Factor Receptor in Breast Cancer Xenografts.* Cancer Research, 2003. **63**(22): p. 7870-7875.
171. Runnels, J.M., P. Zamiri, J.A. Spencer, I. Veilleux, X. Wei, A. Bogdanov, and C.P. Lin, *Imaging molecular expression on vascular endothelial cells by in vivo immunofluorescence microscopy.* Molecular imaging, 2006. **5**(1): p. 31-40.
172. Zou, P., S. Xu, S.P. Povoski, A. Wang, M.A. Johnson, E.W. Martin, V. Subramaniam, R. Xu, and D. Sun, *Near-Infrared Fluorescence Labeled Anti-TAG-72 Monoclonal Antibodies for Tumor Imaging in Colorectal Cancer Xenograft Mice.* Molecular Pharmaceutics, 2009. **6**(2): p. 428-440.
173. Zhang, M., Z. Zhang, D. Blessington, H. Li, T.M. Busch, V. Madrak, J. Miles, B. Chance, J.D. Glickson, and G. Zheng, *Pyropheophorbide 2-Deoxyglucosamide: A New Photosensitizer Targeting Glucose Transporters*. Bioconjugate Chemistry, 2003. **14**(4): p. 709-714.
174. Zhang, Z., H. Li, Q. Liu, L. Zhou, M. Zhang, Q. Luo, J. Glickson, B. Chance, and G. Zheng, *Metabolic imaging of tumors using intrinsic and extrinsic fluorescent markers.* Biosensors and Bioelectronics, 2004. **20**(3): p. 643-650.
175. Galiè, M., P. Farace, C. Nanni, A. Spinelli, E. Nicolato, F. Boschi, P. Magnani, S. Trespidi, V. Ambrosini, S. Fanti, F. Merigo, F. Osculati, P. Marzola, and A. Sbarbati, *Epithelial and mesenchymal tumor compartments exhibit in vivo complementary patterns of vascular perfusion and glucose metabolism.* Neoplasia (New York, N.Y.), 2007. **9**(11): p. 900-908.
176. Tseng, J., L.K. Dunnwald, E.K. Schubert, J.M. Link, S. Minoshima, M. Muzi, and D.A. Mankoff, *18F-FDG Kinetics in Locally Advanced Breast*

Cancer: Correlation with Tumor Blood Flow and Changes in Response to Neoadjuvant Chemotherapy. Journal of Nuclear Medicine, 2004. **45**(11): p. 1829-1837.